COMPUTATIONAL ANALYSIS OF NON-ISOTHERMAL FLOW OF NON-NEWTONIAN FLUIDS

BY

IKENNA IREKA EBUBECHUKWU

A THESIS SUBMITTED FOR THE DEGREE OF
Doctor of Philosophy
IN THE DEPARTMENT OF MATHEMATICS AND APPLIED MATHEMATICS,
FACULTY OF SCIENCE, UNIVERSITY OF CAPE TOWN
FEBRUARY 2015

SUPERVISOR: DR. TIRIVANHU CHINYOKA

The undersigned, IKENNA IREKA EBUBECHUKWU, in his quality of doctoral candidate for a Ph.D. degree in Applied Mathematics granted by the University of Cape Town, hereby, attests that the research exposed in this thesis titled "COMPUTATIONAL ANALYSIS OF NON-ISOTHERMAL FLOW OF NON-NEWTONIAN FLUIDS", is original and that it has not been and will not be used to pursue or attain any other academic degree of any level at any other academic institution, be it foreign or South African.

SIGNATURE:____________________

DATE :____________________

Dedicated to my lovely wife Rosemary and son Chidiebube.

Acknowledgment

I appreciate you my God and father for availing me strength, wisdom, knowledge and understanding all through the course of this study. All the glory be to you LORD.

I want to say a big thank you to my supervisor, Dr. T. Chinyoka for his consistent tireless support and assistance throughout the course of this work. My sincere gratitude also goes to the German government for providing me with the necessary financial support through the ANSTI /DAAD in-region scholarship, which aided me to complete my research successfully within the stipulated time. I equally acknowledge their travel support through the DAAD (German Academic exchange Service) short-term research scholarship, which granted me the opportunity to visit the Fraunhofer ITWM, Kaiserslautern Germany, where I had six months of productive research experience. In addition, I appreciate the kind support of the University of Cape Town (UCT) via the UCT Refugee and International students scholarship as well as the travel support they provided me through the Max & Lillie Sonnenberg scholarship for my travel to Germany. On the same note, my unreserved appreciation goes to the Fraunhofer Institute for providing me with all the necessary tools and enabling work environment, which enhanced my productivity during my six months with them. I particularly want to thank Drs. Dariusz Niedziela and Konrad Steiner of the SMS department in Fraunhofer ITWM for their support. I also appreciate our

collaborators at TU Chemnitz Germany, who provided us with relevant experimental data necessary to validate one of the important results in this thesis.

To everyone who made this study a great success; my colleagues at UCT (Mebratu F. Wakeni and Gordon N. K. Amoako), my brethren in the Redeemed Christian Church of God (RCCG) Latter House Parish, all the members of the Redeemed Christian Fellowship (RCF) UCT chapter, my friends (F. O. Onyekwum, A. A. Osuntuyi, T. T. Sajobi, the Enaholos & many others) and colleagues at the Obafemi Awolowo University (O.A.U) ile-Ife Nigeria. Thank you so much for all your prayers and support, God richly reward you all.

To my mentors Prof. S. S. Okoya and Prof. Alireza Baghai-Wadjii; words cannot express my gratitude to you. Your impact in my life is immeasurable you are well appreciated. I equally want to acknowledge Surveyor Akhigbe K. Irenen for his incessant support to my family during the course of my studies.

I will not forget the consistent encouragement and prayers of my parents Mr. and Mrs. Innocent O. Ireka, thank God for using them immensely in helping me reach where I am today, Dad and Mum, you are wonderful people; God bless you. I also wish to appreciate the support of my siblings, uncles, in-laws and all and sundry who in one way or the other supported this course, thank you so much.

Finally, to my darling wife (Rosemary) and wonderful son (Chidiebube), it would not have been possible without your support. I cannot express how much it meant to me. Thank you so much for all your care, support, prayers, encouragement and sacrifices. My God continually bless you.

Contents

Abstract

The dynamics of complex fluids under various conditions is a model problem in biofluidics and in process industries. We investigate a class of such fluids and flows under conditions of heat and/or mass transfer. Experiments have shown that under certain flow conditions, some complex fluids (e.g. worm-like micellar solutions and some polymeric fluids) exhibit flow instabilities such as the emergence of regions of different shear rates (shear bands) within the flow field. It has also been observed that the reacting mixture in reaction injection molding of polymeric foams undergoes self-expansion with evolution of heat due to exothermic chemical reaction. These experimental observations form the foundation of this thesis. We explore the heat and mass transfer effects in various relevant flow problems of complex fluids. In each case, we construct adequate mathematical models capable of describing the experimentally observed flow phenomena. The mathematical models are inherently intractable to analytical treatment, being nonlinear coupled systems of time dependent partial differential equations. We therefore develop computational solutions for the model problems. Depending on geometrical or mathematical complexity, finite difference or finite volume methods will be adopted. We present the results from our numerical simulations via graphical illustrations and validate them (qualitatively) against 'similar' results in the literature; the quotes being necessary in keeping in mind the novelties introduced in our investigations which are otherwise absent in the existing literature. In the case where experimental data is available, we validate our numerical simulations against such experimental results.

Summary

The flow of non-Newtonian fluids under various geometric and physical conditions is of significant relevance in several industrial processes. Indeed, a comprehensive understanding of non-Newtonian fluid dynamics is of fundamental importance to the process industry with applications ranging in scope from food processing and other household product development to polymer processing, petroleum transport & processing and a host of other mining applications. The majority of these industrial processes necessarily occur under variable temperature (non-isothermal) conditions. Despite the significant industrial importance, a comprehensive scientific understanding of the dynamics of these complex (non-Newtonian) fluids under non-isothermal conditions remains scant. It is the goal of this study to add to this very active area of research and hence contribute to the growing body of knowledge in this very important scientific field.

Theoretical and experimental studies have independently demonstrated unequivocally that under certain flow conditions, viscoelastic fluids (a class of non-Newtonian fluids) exhibit various flow instabilities. A number of such instabilities have been shown to lead to material wastage and increased operational costs in industrial processes. An understanding of the origins of such instabilities and how they can be mitigated is therefore crucial. The current study limits attention to the flow instabilities that manifest as shear bands in the shear flow of polymeric fluids and worm-like micellar solutions as well as to the complex dynamics exhibited by self-expanding reacting polymeric foams in Reaction Injection Molding (**RIM**). As already hinted, the majority of industrial fluid dynamical processes occur under conditions of variable temperature and concentration. Heat and mass transfer effects are therefore central to these industrial processes. A thorough theoretical understanding of the heat and mass transfer processes in the dynamics of industrial fluids would ideally lead to adequate

model predictions of relevant flow behaviour. This knowledge will in turn provide the industrialist with relevant information regarding minimizing both the wastage of raw materials and operational/experimental costs. The current study focuses on heat transfer processes under either homogeneous or heterogeneous conditions. We particularly concentrate on building crucial knowledge and understanding of non-isothermal processes in the flow of complex fluids.

Being computational in focus, this study presents numerical investigations of non-isothermal (temperature dependent) flows of fluids exhibiting complex rheological behaviour under various physical conditions. The Mathematical formulation of the relevant flow phenomena investigated in this study comprise of systems of coupled, nonlinear and time-dependent partial differential equations. The mathematical complexity posed by such model equations makes them analytically intractable, hence our recourse to purely computational methodology for the solution processes in this study. Following the very successful implementation, by multiple researchers over the years, of the finite difference and finite volume methods in solving complex mathematical problems, we adopt these two numerical methodologies as mathematical tools for the solution process of our nonlinear model equations. The choice of the actual numerical methodology in each particular case is dependent on the related flow and/or geometric complexity. Validation of results is done either against similar benchmark results in the literature or against experimental data.

The first chapter (1) presents an overview of non-Newtonian fluids. Various non-Newtonian constitutive models and their applicability or limitation with respect to relevant applications are presented and discussed. The main results of this thesis are presented in chapters 2 - 4. In chapter 2, we employ robust finite difference techniques to investigate numerically the shear-induced flow instabilities (shear banding in particular) observed in the shear flow of certain classes of viscoelastic fluids. We

limit attention to those viscoelastic fluids that can be described empirically by the Johnson-Segalman constitutive model. We particularly explore the wall-slip and non-isothermal effects on the flow of such fluids in simple geometries. Investigations in chapter 3 extend the works of chapter 2 to more complex annular geometric constrictions and explore some important mathematical techniques that are necessary to capture accurately the conditions related to the onset of instabilities. In particular, the effects of viscoelastic stress diffusion, geometric constrictions and fluid injection on the annular flow of fluids governed by the diffusive Johnson-Segalman constitutive models is investigated under non-isothermal and wall slip conditions. The finite difference method is also adopted here for the solution processes. Chapter 4 presents a joint numerical and experimental study of expanding polyurethane foams. Motivated by experimental observations, the relevant mathematical formulation introduces a non-divergence free framework for the continuity equation. This concept reflects the self-expansion processes as observed in the relevant physical systems. Efficient numerical techniques based on the finite volume method are used for the solution process of the nonlinear systems of partial differential equations. The foam growth phenomena as well as temperature distributions within the bulk flow are captured numerically and validated against the experimental results.

List of Tables

List of Figures

Chapter 1

General Introduction

"Everything flows, even the mountains will flow...if you wait long enough!"

- Markus Reiner

Despite the fact that any non-zero volume of a fluid actually consist of billions of individual molecules or atoms, we will (in this thesis) treat fluids as continuous media. We thus will only be interested, not in the behavior of individual constituent molecules or atoms, but in those macroscopic properties of the bulk fluid. We will therefore associate with any infinitesimal (but nonzero) volume of fluid those macroscopic properties; such as velocity, density, pressure, temperature etc. that we would normally associate with the bulk fluid. This forms the basis of the so-called continuum hypothesis and provides the foundation for the study of continuum mechanics.

The study of deformation and flow of matter is now widely known as *rheology*. The invention of the term *rheology* in 1920 is attributed to Eugene Cook Bingham, then a professor at Lafayette College in Pennsylvania, USA. It is also understood that the suggestions of his colleague, Markus Reiner, played a significant role in the birth of the term. For a historical review of the concept of rheology, see for example [6, 109] and the references there in. The deformation properties of Newtonian fluids all follow Newton's law of viscosity and the flow of such fluids are all governed by the Navier-Stokes equations. The deformation and flow properties of non-Newtonian fluids, on the other hand, are less predictable and cannot be described by unique and all encompassing laws. This then forms the foundation of the field of rheology; i.e. to account for the deformation and flow behavior of non-Newtonian fluids - which we will alternately refer to as complex fluids. The prevalence and importance of such fluids in everyday life has made the field of rheology all the more critical. The majority of biological and industrial processes indeed involve these types of fluids. A huge array of fields of rheology have therefore emerged to deal with equally diverse challenges in the relevant biological and industrial processes. Examples include bio-rheology (say in blood flow and other biological soft matter studies), food rheology, polymer rheology, foam rheology, suspension rheology, chemo-rheology etc.

In many flow applications involving non-Newtonian fluids such as food processing, polymer processing, tribology, reaction injection molding of polyurethane foams etc., changes in temperature in space and time as a result of, say, viscous heating, mechanical dissipation, material deformation, exothermic reactions, external heating etc., usually become significant and must therefore be accounted for. This thesis is thus premised on investigations of non-isothermal (temperature dependent) flows involving complex fluids. The non-Newtonian fluids of interest will be broadly categorized into two main groups, i.e. Generalized Newtonian fluids (GNFs) and Viscoelastic fluids. The first category typifies the viscous and inelastic fluids. The inclusion of memory effects or fluid elasticity leads to the latter class.

Practically all fluids exhibit a certain degree of resistance to flow when subject to deformation or stress. A measure of this intrinsic material behavior is referred to as the fluid's viscosity η. The viscosity of a Newtonian fluid, at a given temperature, pressure and concentration remains constant irrespective of the deformation rates encountered by the fluid. The viscosity of any fluid can however vary with variations in the fluid temperature, pressure and concentration. Various empirically determined non-isothermal viscosity models have been derived in literature [103], see for example Table: 1.1. The terms A, B, C_1, C_2 in the table are empirical constants.

Table 1.1: Temperature dependent viscosity models

Reynold's model	$\eta(T) = \eta_0 \exp(-BT)$
Vogel's model	$\eta(T) = \eta_0 \exp\left(\frac{B}{T-T_0}\right)$
Arrhenius model	$\eta(T) = \eta_0 \exp(E/RT)$
Nahme model	$\eta(T) = \eta_0 \exp\left(\frac{T-T_0}{T_0}\right)$
William-Landel-Ferry (WLF) model	$\eta(T) = \eta_0 \exp\left(\frac{-C_1(T-T_0)}{C_2+T-T_0}\right)$
Fulcher model	$log_{10}(\eta(T)) = -A + \frac{B\times 10^3}{T-T_0}$

In general, the fluid viscosity can depend on a combination of temperature, pressure, time, shear rate, cure/polymerization rate (as in the case of polymeric foams) and volume fraction, see for example [46]. The shear rate dependence of viscosity is a particular characteristic of non-Newtonian fluids, the only known exceptions being the Boger fluids whose viscosities have been demonstrated to be independent of shear rates. The Newtonian viscosity model thus has severe limitations in the bulk of practical rheological applications. In addition to the relevant constitutive modeling for the viscosity, Newtonian and non-Newtonian fluid behavior is also characterized mathematically via appropriate, usually empirically determined, constitutive models for the fluid stresses. We can denote the total stress in a fluid, $\boldsymbol{\tau}$, as,

$$\boldsymbol{\tau} = -\nabla p + \boldsymbol{T},$$

where p is the fluid pressure and $\boldsymbol{T}$ represents extra stresses. Under this framework, the relevant fluid dynamical equations, as derived from the conservation laws of physics, i.e. conservation of mass, momentum and energy respectively read,

$$\frac{\partial \rho}{\partial t} + \nabla \cdot (\rho \boldsymbol{v}) = 0, \tag{1.1}$$

$$\rho \frac{D\boldsymbol{v}}{Dt} = -\nabla p + \nabla \cdot \boldsymbol{T} + \rho \boldsymbol{F}, \tag{1.2}$$

$$\rho c_v \frac{DT}{Dt} = -p \nabla \cdot \boldsymbol{v} + \nabla \cdot (\kappa \nabla T) + \Phi + q_s, \tag{1.3}$$

where

$$\frac{D}{Dt} = \frac{\partial}{\partial t} + \boldsymbol{v} \cdot \nabla, \tag{1.4}$$

is the material derivative, q_s represents heat sources/sinks and the other notation is otherwise standard to fluid dynamics. Eqs. (1.1 - 1.3) where independently derived, in the nineteenth century, by Navier and Stokes for Newtonian fluids, where the stress tensor $\boldsymbol{T}$ follows Newton's law of viscosity. Newtonian fluids are therefore commonly also referred to as Navier-Stokes fluids.

Section 1.1 gives a brief summary of Newtonian fluid behavior. We follow this up in section 1.2 with a summary description of non-Newtonian fluids, their observed behavior as well as their mathematical modelling. Based on this brief but fundamental foundation, the ensuing discussion in section 1.3 then lays out the general motivation behind this thesis.

1.1 Newtonian Fluids

The theory of fluid mechanics, as described by sir Isaac Newton, was based on simple shear experiments. In particular, Newton deduced that the shear stress or force per unit area $F/\hat{A}$, denoted in tensor form by $\boldsymbol{T}$, required to produce motion was proportional to the velocity gradient or shear rate $\dot{\gamma}$, denoted as $\boldsymbol{D}$ in tensor form, and that the constant of proportionality η is the coefficient of shear viscosity. This stress constitutive model for Newtonian fluids is summarized mathematically as,

$$\boldsymbol{T} = \eta \boldsymbol{D}. \tag{1.5}$$

The deformation rate tensor $\boldsymbol{D}$ is given by,

$$\boldsymbol{D} = \nabla \boldsymbol{v} + (\nabla \boldsymbol{v})^T, \tag{1.6}$$

where the superscript ^{T} indicates matrix transposition. The viscosity η in this case may not depend on the shear rates. It is usually common to define the stress tensor and the deformation rate tensor respectively as,

$$\boldsymbol{T} = 2\eta \boldsymbol{D}, \quad \text{with,} \quad \boldsymbol{D} = \frac{1}{2}\left[\nabla \boldsymbol{v} + (\nabla \boldsymbol{v})^T\right].$$

Unless otherwise stated, we will adopt the notation from Eqs. (1.5-1.6) as much as possible.

A ***Newtonian fluid*** is therefore any fluid whose stress constitutive equation for $\boldsymbol{T}$ follows Eq. (1.5) and whose viscosity may vary with concentration, temperature and pressure but may not vary with deformation rate, applied stress, time or polymerization rates as in the case of reacting polymer foams. Typical example of Newtonian fluids include gases, water, low molecular weight inorganic solutions, molten metals and salts, simple organic liquids, etc.

Experiments have shown that Newton's assumption of simple linear relationship between the shear stress and shear rate is inadequate and even inappropriate in accounting for the flow and deformation behavior of a large class of fluids of practical interests [6]. Fluids whose stress-strain behavior deviate from the linear relationship given in Eq. (1.5) and/or whose viscosities are dependent on shear rates, applied stresses, time, reaction rates are called non-Newtonian fluids and are generally classified as complex fluids.

1.2 Non-Newtonian Fluids

As already indicated, non-Newtonian fluid behavior arises from deviation in either of the two fundamental characteristics of Newtonian behavior. To recap, the two fundamental characteristic of Newtonian fluid behavior are (i) a linear stress-strain relationship and (ii) viscosity that is independent of shear rates, applied stresses, time and reaction rates.

Complex fluids such as those derived from polymers (i.e. polymer solutions or melts) and micellar solutions, are built from a microstructure that consists of macromolecules. The macromolecular structure significantly affects the response of the fluid to deformation leading to non-linear behavior between the applied stresses and the resulting deformation rates. The nonlinear stress-strain relationships makes these fluids non-Newtonian. The elastic response to deformation due to the macromolecular structure in fact means that these fluids exhibit solid like behavior. This leads to the class of fluids known as the viscoelastic fluids, see section 1.2.3.

Other classes of fluids, such as drilling muds, slurries, most paints, suspensions of small particles etc. do not exhibit any elastic behavior. Additionally these fluids exhibit linear stress-strain relationships in shear experiments as with Newtonian fluids. However, these fluids remain inherently non-Newtonian due to the fact that their viscosities show strong dependence to shear rates, applied stresses and time. Such fluids are classified as Generalized Newtonian fluids, [6, 17, 89, 97].

1.2.1 Generalized Newtonian Fluids

Generalized Newtonian fluids (GNF) exhibit shear or time dependent viscosity. The stress constitutive model however follows the linear stress-strain model given by Newton's law of viscosity,

$$\boldsymbol{T} = 2\eta(\dot{\gamma})\,\boldsymbol{D}, \quad \textit{with}, \quad \boldsymbol{D} = \frac{1}{2}\left[\nabla\boldsymbol{v} + (\nabla\boldsymbol{v})^T\right]. \tag{1.7}$$

It is important to note that the Newtonian fluid model as well as the GNF model are special cases of the *Reiner-Rivilin fluids model*,

$$\boldsymbol{T} = \alpha\boldsymbol{I} + \Gamma_1\boldsymbol{D} + \Gamma_2\boldsymbol{D}^2,$$

where α is a Lagrange multiplier, $\boldsymbol{I}$ is the identity tensor and Γ_1 and Γ_2 dependent on the second and third principal invariants of the deformation rate tensor $\boldsymbol{D}$.

For incompressible fluids, the first scalar invariant of $\boldsymbol{D}$ is,

$$\boldsymbol{I_D} = \mathrm{tr}\,(\boldsymbol{D}) = \nabla \cdot \boldsymbol{v} = 0, \tag{1.8}$$

and for shearing flows, the third invariant vanishes,

$$\boldsymbol{III_D} = \det(\boldsymbol{D}) = 0. \tag{1.9}$$

The viscosity, $\eta(\dot{\gamma})$, in Eq. (1.7) therefore only depends on the second principal invariant $\boldsymbol{II_D}$ which is given by,

$$\boldsymbol{II_D} = \frac{1}{2}\left[(\mathrm{tr}\,\boldsymbol{D})^2 - \mathrm{tr}\,(\boldsymbol{D}^2)\right]. \tag{1.10}$$

For simple shear flows, it suffices to write $\mathbf{II}_{\boldsymbol{D}}$ as the magnitude of the deformation tensor, so that,

$$\boldsymbol{II_D} = |\boldsymbol{D}| = \sqrt{2\boldsymbol{D} : \boldsymbol{D}^T} = \frac{\dot{\gamma}}{2}. \tag{1.11}$$

The term $\dot{\gamma}$ in Eq. (1.11) is defined as $\dot{\gamma} = 2|\boldsymbol{D}|$. Alternatively, if we define

$$\boldsymbol{D} = \nabla\boldsymbol{v} + (\nabla\boldsymbol{v})^T, \tag{1.12}$$

then we write $\dot{\gamma} = |\boldsymbol{D}|$.

Similarly to the given dependence of the apparent viscosity on the shear rate, $\eta = \eta(\dot{\gamma})$, it is also possible to describe the viscosity dependence on the magnitude of the shear stress. If, say, we set $\tau = |\boldsymbol{T}|$, then we can write the alternative expression $\eta = \eta(\tau)$.

Time independent inelastic fluids

Time independent inelastic fluids may exhibit shear thinning, shear thickening or yield stress behavior. If the fluid viscosity decreases with increasing shear rate, then the fluid is classified as shear thinning. If on the other hand the fluid viscosity increases with increasing shear rate, then the fluid is classified as shear thickening. The flow curves in Fig. 1.1 summarizes these phenomena.

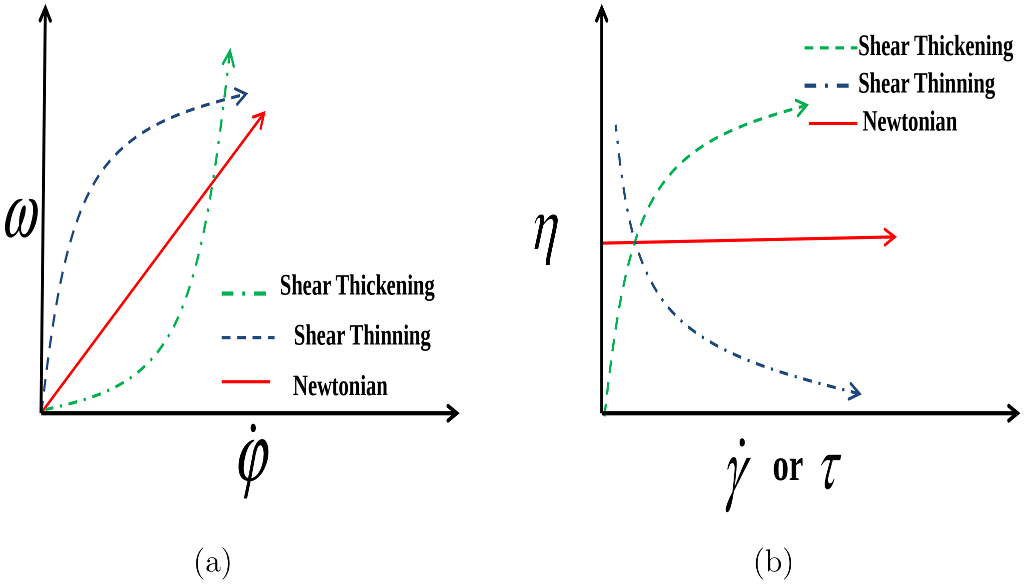

(a) (b)

Figure 1.1: Flow curves for shear thinning, Shear thickening and Newtonian fluids

The viscosity constitutive models describing the physically observed combinations of the stress-strain behavior illustrated in Fig. 1.1 vary in complexity from a one-parameter *(Power law)* models to five-parameter *(Carreau - Yasuda)* models depending on the shear regions captured by the particular model. In sections 1.2.1 - 1.2.2, we present some common viscosity constitutive models.

Power Law model

The viscosity constitutive models exhibiting the stress-strain behavior as strictly illustrated in Fig. 1.1 are described by an empirical Power law model given by,

$$\eta = k\dot{\gamma}^{n-1}, \tag{1.13}$$

where k called the consistency, with a unit of $force \times (time)^n/length^2$ is the shear stress at a shear rate of $1.0s^{-1}$. The dimensionless parameter n is known as the flow behavior index. We note the following limiting behavior,

$$\begin{array}{lll} \text{if } \; n < 1 & \lim\limits_{\dot{\gamma}\to 0} \eta(\dot{\gamma}) = \infty & \lim\limits_{\dot{\gamma}\to \infty} \eta(\dot{\gamma}) = 0, \\ \text{if } \; n > 1 & \lim\limits_{\dot{\gamma}\to 0} \eta(\dot{\gamma}) = 0 & \lim\limits_{\dot{\gamma}\to \infty} \eta(\dot{\gamma}) = \infty. \end{array} \tag{1.14}$$

The Power law model thus describes shear thinning behavior for $n < 1$ and shear thickening behavior for $n > 1$. The model reduces to a Newtonian viscosity model when $n = 1$, with constant viscosity k.

Although most shear thinning fluids with complex micro-structure are classified as non-Newtonian, they can also exhibit Newtonian behavior at low and high shear rate (see Fig. 1.2), these regions are referred to as the zero-shear-rate and the infinite-shear-rate regions, with corresponding zero-shear-rate-limiting viscosity η_0, and infinite-shear-rate-limiting viscosity, η_∞ respectively. The major limitation of the Power law model in physical applications, is therefore it's inability to describe and capture these low and high shear rate regimes of constant, finite and non-zero viscosity.

In general, the evolution of viscosity under increasing shear rate, for shear thinning fluids, shows three different regions: a constant viscosity (η_0) zero-shear-rate region,

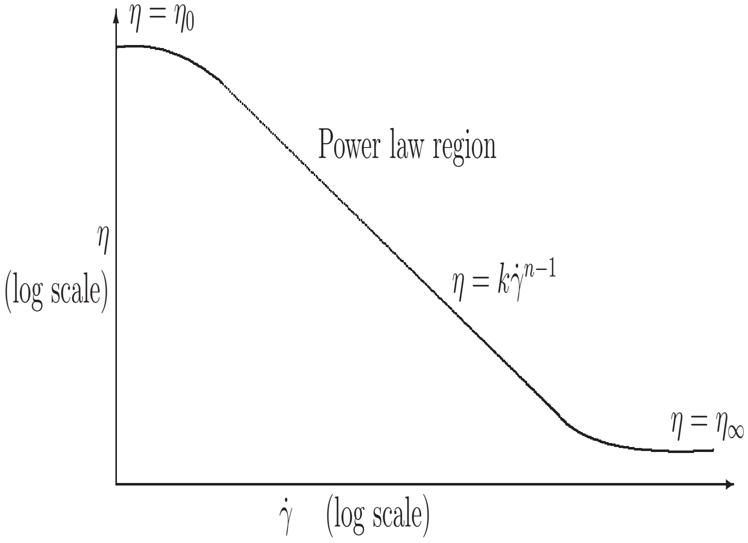

Figure 1.2: Log - log plot of apparent viscosity η against shear rate $\dot{\gamma}$, for shear thinning non-Newtonian fluids

followed by a Power law region of decreasing viscosity ultimately leading to a constant viscosity (η_∞) infinite-shear-rate region, see Fig. 1.2. Most paints exhibit this type of shear thinning behavior.

Prandtl-Eyring model

This two parameter shear-thinning model is an alternative to the Power law model that captures the zero-shear-rate regime,[1]

$$\eta = \eta_0 \frac{\sinh^{-1}(\lambda\dot{\gamma})}{\lambda\dot{\gamma}}, \tag{1.15}$$

where the parameter η_0 and λ are material constants. The limiting behavior shows that,

$$\lim_{\dot{\gamma}\to 0} \eta(\dot{\gamma}) = \eta_0, \qquad \lim_{\dot{\gamma}\to\infty} \eta(\dot{\gamma}) = 0. \tag{1.16}$$

The Prandtl-Eyring model is incapable of capturing the infinite-shear-rate regime of constant and non-zero viscosity η_∞. This motivates the Powell-Eyring improvement.

Powell-Eyring model

This model is a three Parameter shear-thinning model which tends to non-zero and finite viscosity in both the lower and upper shear-rate limits,

$$\eta = \eta_\infty + (\eta_0 - \eta_\infty)\frac{\sinh^{-1}(\lambda\dot{\gamma})}{\lambda\dot{\gamma}}. \tag{1.17}$$

This can alternatively be re-arranged as:

$$\frac{\eta - \eta_\infty}{\eta_0 - \eta_\infty} = \frac{\sinh^{-1}(\lambda\dot{\gamma})}{\lambda\dot{\gamma}}. \tag{1.18}$$

The limiting behavior shows that,

$$\lim_{\dot{\gamma}\to 0}\eta = \eta_0 \quad \text{and} \quad \lim_{\dot{\gamma}\to\infty}\eta = \eta_\infty. \tag{1.19}$$

If $\eta_\infty = 0$ in Eq. (1.17) or Eq. (1.18) above, we obtain the *Prandtl - Eyring model*, see Eq. (1.15). One of the major deficiencies of the Powell-Eyring model is it's inability to describe the relation between shear rate ($\dot{\gamma}$) and shear stress (τ) over a wide range of $\dot{\gamma}$ (or τ). Furthermore, the power law character from experimental data is difficult to reproduce using this model, see [5].

Cross model

The cross model is a four parameter model whose apparent viscosity approaches a non-zero and finite viscosity in both the lower and upper shear-rate limits. The mathematical description is given as,

$$\frac{\eta - \eta_\infty}{\eta_0 - \eta_\infty} = \frac{1}{1 + (\lambda\dot{\gamma})^m}, \tag{1.20}$$

where m is a dimensionless parameter. The limiting behavior shows that,

$$\begin{array}{lll} \text{if } \ m < 1 & \lim\limits_{\dot{\gamma}\to 0} \eta(\dot{\gamma}) = \eta_0 & \lim\limits_{\dot{\gamma}\to\infty} \eta(\dot{\gamma}) = \eta_\infty, \\ \text{if } \ m > 1 & \lim\limits_{\dot{\gamma}\to 0} \eta(\dot{\gamma}) = \eta_\infty & \lim\limits_{\dot{\gamma}\to\infty} \eta(\dot{\gamma}) = \eta_0, \end{array} \tag{1.21}$$

and when $m = 0$, the model represents a Newtonian fluid.

The mathematical representation for the Cross model can be re-arranged as,

$$\frac{\eta_0 - \eta}{\eta - \eta_\infty} = (\lambda\dot{\gamma})^m. \tag{1.22}$$

It then easily follows from this definition that under certain assumptions on the parameters, the Cross model reduces to the Power Law model. In particular, if $\eta << \eta_0$ and $\eta >> \eta_\infty$, the Cross model reduces to

$$\eta = \frac{\eta_0}{(\lambda\dot{\gamma})^m}, \tag{1.23}$$

hence, if we define $m = 1 - n$ and set $k = \eta_0\lambda^{-m}$, then Eq. (1.23) becomes a Power law model,

$$\eta = k\dot{\gamma}^{n-1}. \tag{1.24}$$

If we assume that $\eta << \eta_0$, then the Cross model as given by Eq. (1.22) reads,

$$\eta = \eta_\infty + \frac{\eta_0}{(\lambda\dot{\gamma})^m}. \tag{1.25}$$

A redefinition of parameters in Eq. (1.25) leads to,

$$\eta = \eta_\infty + k\dot{\gamma}^{n-1}. \tag{1.26}$$

Eq. (1.26) is known as the Sisko model and was originally proposed for high shear rate measurements of lubricating grease.

Carreau-Yasuda model

The Carreau-Yasuda model is an alternative model to the Cross model. This five parameter model fits accurately to a range of experimentally obtained viscosity data. It therefore finds huge application in several problems of industrial relevance. The mathematical description is given by,

$$\frac{\eta - \eta_\infty}{\eta_0 - \eta_\infty} = [1 + (\lambda\dot{\gamma})^c]^{(n-1)/c}. \tag{1.27}$$

The constant c in Eq. (1.27) above controls the breadth of the transition from Newtonian to power Law regimes. In particular, if c is set to 2, Eq. (1.27) becomes,

$$\frac{\eta - \eta_\infty}{\eta_0 - \eta_\infty} = [1 + (\lambda\dot{\gamma})^2]^{(n-1)/2} \tag{1.28}$$

Eq. (1.28) above is the *Carreau model* which is a special case of the Carreau-Yassuda model Eq. (1.27). The Carreau model is a popular alternative to the *Cross model* in theoretical investigations. The Carreau model was developed from network theory, but has found great use as an empirical relation.

Ellis Model

This three parameter model gives the viscosity (η) in terms of shear stress instead of shear rate. The Ellis model is given as,

$$\eta(\tau) = \frac{\eta_0}{1 + \left(\frac{\tau}{\tau_{1/2}}\right)^{b-1}}, \quad \text{where} \quad \tau_{1/2} = \tau|_{\eta=\eta_0/2}. \tag{1.29}$$

For very high shear stress, the model displays power law behavior. The Ellis model is therefore related to the power law model by setting $k = \eta_0^{1/b}\tau_{1/2}^{1-(1/b)}$ and $n = 1/b$, where b is a constant.

1.2.2 Yield Stress Fluids

Yield stress fluids resist flow until a critical (or yield) stress is reached and beyond which the fluids will start to flow. Fluids such as, toothpaste, Mayonnaise etc. exhibit this type of behavior. If the applied stress is less than the yield stress, the material deformation behaves like that of an elastic solid, hence, it restores to its original configuration as soon as loading is removed. But once the yield stress is exceeded, the material experiences a non reversible plastic deformation. This family of fluids are also referred to as viscoplastic fluids. Various constitutive relations have been proposed to model the flow behavior of viscoplastics fluids in simple shear flows. Two types of plastic behavior are observed after the yield stress is exceeded, either Bingham plastic or Casson plastic behavior, see Fig. 1.3.

Beyond the yield stress values, Bingham plastic behavior is similar to Newtonian behavior and hence a linear stress-strain constitutive model results:

$$\tau = \tau_Y + \eta_p\dot{\gamma}. \tag{1.30}$$

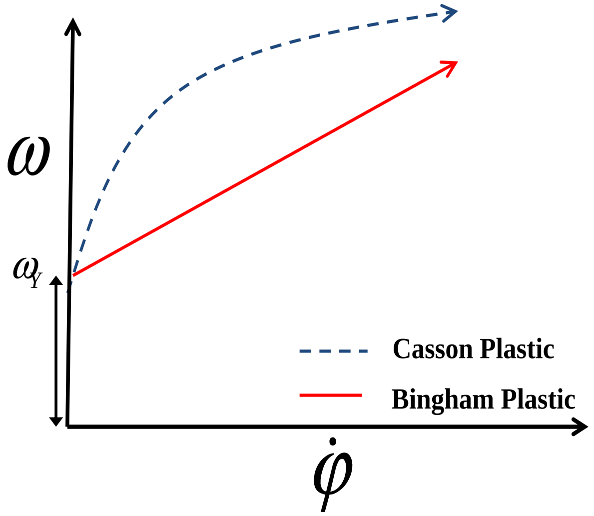

Figure 1.3: shear stress τ against shear rate $\dot{\gamma}$ for yield stress fluids

The viscosity constitutive model for a Bingham plastic can be written as:

$$\eta = \begin{cases} \infty & \text{if} \quad \tau \leq \tau_Y, \\ \eta_0 + \frac{\tau_Y}{\dot{\gamma}} & \text{if} \quad \tau > \tau_Y. \end{cases} \tag{1.31}$$

A modification of the Bingham model leads to the Herschel-Bulkley model Eq. (1.32), which incorporates the power law model into the Bingham Model.

$$\eta = \begin{cases} \infty & \text{if} \quad \tau \leq \tau_Y, \\ k\dot{\gamma}^{n-1} + \frac{\tau_Y}{\dot{\gamma}} & \text{if} \quad \tau > \tau_Y. \end{cases} \tag{1.32}$$

Beyond the yield stress values, Casson plastic behavior, as with shear thinning behavior, gives nonlinear stress-strain relationships. The viscosity constitutive model for a typical Casson plastic thus reads,

$$\sqrt{\eta} = \begin{cases} \infty & \text{if} \quad \tau \leq \tau_Y, \\ \sqrt{\eta_0} + \sqrt{\frac{\tau_Y}{\dot{\gamma}}} & \text{if} \quad \tau > \tau_Y. \end{cases} \tag{1.33}$$

For a more comprehensive list of examples of viscoplastic fluid models, the reader is referred to [79] and the references therein.

Some inelastic non-Newtonian fluids exhibit time dependent viscosity behavior. Such fluids are classified as either rheopectic or thixotropic fluids respectively depending on whether the viscosity increases or decreases with time under shear. Corn starch is a typical example of a fluid exhibiting rheopectix behavior.

Generalized Newtonian fluid models are inadequate for the modelling of normal stress effects such as rod climbing, die swell etc. that are otherwise characteristic behavior observed in flow of polymeric fluids. Additionally, the GNF models are inappropriate for the description of viscoelastic behavior as well as extensional phenomena. In the following section, we present some viscoelastic fluid models that can account for these and other fluid behavior that are otherwise not accounted for by the GNF models.

1.2.3 Viscoelastic fluids

The so-called viscoelastic fluids (also known as *memory fluids*) exhibit both solid like (elastic) and liquid like (viscous) behavior. Their response to deformation over different time scales determine which of either the solid-like or liquid-like behavior is dominant. In general the viscoelastic fluids exhibit dominant elastic solid-like behavior if the timescale of the deformation process is short. If on the other hand the timescale of the deformation process is long, then viscous liquid-like behavior dominates. The ratio of the material time scale to the time scale of the deformation process is denoted by a dimensionless number called the Deborah or the Weissenberg number. Liquid-like behavior therefore dominates at low Deborah numbers and solid-like behavior at high Deborah numbers. For a comprehensive history and description of viscoelastic fluids, we refer to the excellent texts by Barnes and that by Bird et. al., [6, 17].

These complex behavior exhibited by viscoelastic fluids can be attributed to the complex response of the fluid stresses under deformation. The stress-strain relationships for viscoelastic fluids are non-linear and markedly different from the linear relationships predicted under Newton's law of viscosity for inelastic fluids. To completely specify the mechanical response of these memory fluids, it is therefore necessary that additional stress constitutive models are added to the system of Eqs. (1.1-1.3). These stress constitutive equations vary from one class of viscoelastic fluids to the other but must be objective and should not lead to changes in the work and energy of the stresses under any arbitrary motion. In general, the stress constitutive models depend on the fluid micro-structure and can be presented in either algebraic, differential, integral or integro-differential forms.

A class of fluid models that describe viscoelastic behavior are the order fluids. Rivlin and Erickson proposed that if the extra stress tensor $\boldsymbol{T}$ for an isotropic fluid is assumed to depend on the gradients of the velocity, acceleration and higher time derivatives at some time t, then there exists a polynomial equation in $\boldsymbol{T}$ of the Rivlin- Erickson tensors $\mathbf{A}_k,\ k \in 1, 2, 3, ...$, such that the constitutive relation can be written as a polynomial of the first N Rivlin Erickson tensors, see [89],

$$\boldsymbol{T} = \boldsymbol{f}(\boldsymbol{A}_1, \boldsymbol{A}_2, \ldots, \boldsymbol{A}_N). \tag{1.34}$$

In particular, first order fluids (Newtonian fluids with $\eta = a_1$) have the representation,

$$\boldsymbol{T} = a_1 \boldsymbol{A}_1. \tag{1.35}$$

Second order fluid have,

$$\boldsymbol{T} = a_1 \boldsymbol{A}_1 + a_2 \boldsymbol{A}_2 + a_{11} \boldsymbol{A}_1^2. \tag{1.36}$$

Third order fluids have,

$$\boldsymbol{T} = (a_1 + a_1' \operatorname{tr}(\boldsymbol{A}_1^2))\boldsymbol{A}_1 + a_2 \boldsymbol{A}_2 + a_{11} \boldsymbol{A}_1^2 + a_3 \boldsymbol{A}_3 + a_{12}(\boldsymbol{A}_1 \boldsymbol{A}_2 + \boldsymbol{A}_2 \boldsymbol{A}_1), \tag{1.37}$$

where the a_i, a_{1j}, $i \in 1, 2, 3$, $j \in 1, 2$ are constant coefficients associated with the fluid material properties and,

$$\boldsymbol{A}_{k+1} = \frac{D\boldsymbol{A}_k}{Dt} + \nabla \boldsymbol{v} \cdot \boldsymbol{A}_k + \boldsymbol{A}_k \cdot (\nabla \boldsymbol{v})^T, \tag{1.38}$$

with $\boldsymbol{A}_1 = \nabla \boldsymbol{v} + (\nabla \boldsymbol{v})^T$.

The order fluids can be used to model slow flows of viscoelastic fluids as well as slightly elastic liquids, i.e. where the fluid deviates slightly from the Newtonian behavior and the Deborah number is low [89].

Linear viscoelastic constitutive models are more appropriate in describing fluid elastic behavior for low deformations and low deformation rates. The extra stress tensor for viscoelastic fluids will be written as,

$$\boldsymbol{T} = \eta \, \boldsymbol{D} + \boldsymbol{\sigma}, \quad \text{with,} \quad \boldsymbol{D} = \nabla \boldsymbol{v} + (\nabla \boldsymbol{v})^T, \tag{1.39}$$

where $\boldsymbol{\sigma}$ represents viscoelastic stresses. The linear viscoelastic constitutive models for $\boldsymbol{\sigma}$ can be obtained from the generalized differential Eq. (1.40),

$$\left(\sum_{k=0}^{m} A_k \frac{\partial^k}{\partial t^k}\right) \boldsymbol{\sigma} = \left(\sum_{k=0}^{n} B_k \frac{\partial^k}{\partial t^k}\right) \boldsymbol{\gamma}, \tag{1.40}$$

where $n = m$ or $n = m - 1$, see [6]. Observe that if $A_i = 0,\ i \in \{1, 2, ..., m\}$, $B_j = 0,\ j \in \{0, 2, 3, ..., n\}$ and if we set $A_0 = 1$ and $B_1 = \eta$, then we obtain the Newtonian fluid model.

Maxwell model

If $A_0 = 1, A_1 = \lambda_1$ and $B_1 = \eta$ are the only non-zero terms in Eq. (1.40), then the model reduces to the linear viscoelastic Maxwell's model Eq. (1.41) with relaxation time λ_1. Maxwell, thinking that gases might be viscoelastic proposed that fluids possessing viscous and elastic behavior could be described by:

$$\boldsymbol{\sigma} + \lambda_1 \dot{\boldsymbol{\sigma}} = \eta_0 \dot{\boldsymbol{\gamma}}. \tag{1.41}$$

The linear viscoelastic Maxwell model Eq. (1.41) has proven to be useful in building the foundation for modeling the dynamics of many polymeric fluids, see [17]. Its inherent limitation to describing linear viscoelastic phenomena however makes it inadequate for general viscoelastic modelling.

Jeffery model

The three constant Jeffery model is another linear viscoelastic model obtained if $A_0 = 1,\ A_1 = \lambda_1, B_1 = \eta$ and $B_2 = \lambda_2$ are the only non-zero terms in Eq. (1.40). The two time constants λ_1 and λ_2 are the relaxation time and retardation time respectively,

$$\boldsymbol{\sigma} + \lambda_1 \dot{\boldsymbol{\sigma}} = \eta_0 \dot{\boldsymbol{\gamma}} + \lambda_2 \ddot{\boldsymbol{\gamma}}. \tag{1.42}$$

The Jeffery model was proposed for the investigation of wave propagation in the earth's mantle.

Generalized Maxwell model

The generalized Maxwell model is obtained by superposition of the Maxwell model. This model is given by

$$\begin{aligned} \boldsymbol{\sigma} &= \sum_{k=1}^{\infty} \boldsymbol{\sigma}_k, \\ \boldsymbol{\sigma}_k + \lambda_1 \dot{\boldsymbol{\sigma}}_k &= \eta_k \dot{\boldsymbol{\gamma}}. \end{aligned} \tag{1.43}$$

Under the influence of large deformation and deformation rates, viscoelastic fluids exhibits remarkable flow patterns such as the rod climbing effect, extrudate swell, flow instabilities due to stick-slip phenomena, shark skin, shear banding, tubeless siphons, etc. These remarkable effects are generally nonlinear phenomena that can only be described via nonlinear viscoelastic models. In particular, these are generally normal force effects, in shear flow, and are associated with the normal stress differences N_1 and N_2. The relevant stress differences for non-Newtonian liquids are,

$$\begin{aligned} \sigma_{12} &= \dot{\gamma}\eta(\dot{\gamma}), && \text{Shear Stress,} \\ \sigma_{11} - \sigma_{22} &= N_1(\dot{\gamma}), && \text{First Normal stress difference,} \\ \sigma_{22} - \sigma_{33} &= N_2(\dot{\gamma}), && \text{Second Normal stress difference.} \end{aligned} \tag{1.44}$$

The normal stress difference coefficients Ψ_1 and Ψ_2, which represent the viscoelastic equivalents of viscosity i.e stress/shear-rate, are given as

$$\begin{aligned} \Psi_1 &= \frac{N_1}{\dot{\gamma}^2}, \qquad \text{First normal stress difference Coefficient,} \\ \Psi_2 &= \frac{N_2}{\dot{\gamma}^2}, \qquad \text{Second normal stress difference Coefficient.} \end{aligned} \tag{1.45}$$

It is not the aim of this thesis to develop new viscoelastic stress constitutive models. We rather seek to explore the existing models to investigate non-isothermal effects associated with the material deformation, chemical reactions, viscous heating etc. on experimentally observed viscoelastic phenomena, such as wall slip, shear bands and foam expansion in injection molding. For a detailed overview of viscoelastic models, the reader is referred to the excellent book of Bird et. al. [17] and the detailed introductory text of Barnes et. al. [6]. For a more mathematical approach, we refer to the books of Renardy [100] and Owens [89]. A rather general viscoelastic stress constitutive model for $\boldsymbol{\sigma}$ is given by,

$$\exp\left(\pi \frac{\lambda}{\eta_v} \operatorname{tr}(\boldsymbol{\sigma})\right) \boldsymbol{\sigma} + \hat{\alpha} \frac{\lambda}{\eta_v} \boldsymbol{\sigma} \cdot \boldsymbol{\sigma} + \lambda \overset{\square}{\boldsymbol{\sigma}} = 2\eta_v \boldsymbol{D}. \tag{1.46}$$

For a given tensor $\boldsymbol{M}$ and scalar a with $0 \leq a \leq 2$, we define:

$$\overset{\square}{\boldsymbol{M}} = (1 - \frac{a}{2}) \overset{\triangledown}{\boldsymbol{M}} + \frac{a}{2} \overset{\triangle}{\boldsymbol{M}}, \tag{1.47}$$

where

$$\overset{\triangledown}{\boldsymbol{M}} = \frac{\partial}{\partial t} \boldsymbol{M} + \boldsymbol{v} \cdot \nabla \boldsymbol{M} - \left[(\nabla \boldsymbol{v})^T \cdot \boldsymbol{M} + \boldsymbol{M} \cdot \nabla \boldsymbol{v} \right], \tag{1.48}$$

and

$$\overset{\triangle}{\boldsymbol{M}} = \frac{\partial}{\partial t}\boldsymbol{M} + \boldsymbol{v}\cdot\nabla\boldsymbol{M} + \boldsymbol{M}\cdot(\nabla\boldsymbol{v})^T + \nabla\boldsymbol{v}\cdot\boldsymbol{M}. \tag{1.49}$$

Table: 1.2 gives some of the common nonlinear viscoelastic stress constitutive models.

Table 1.2: Some differential viscoelastic constitutive models

Model Name	Constitutive model for $\boldsymbol{\sigma}$	N_1 and N_2
Oldroyd-B	$\boldsymbol{\sigma} + \lambda\overset{\triangledown}{\boldsymbol{\sigma}} = 2\eta_v\boldsymbol{D}$	$N_1 > 0$ $N_2 \equiv 0$
Geisekus	$\boldsymbol{\sigma} + \alpha(\boldsymbol{\sigma}\boldsymbol{\cdot}\boldsymbol{\sigma}) + \lambda\overset{\triangledown}{\boldsymbol{\sigma}} = 2\eta_v\boldsymbol{D}$	$N_1 > 0$ $N_2 \neq 0$
Johnson-Segalman	$\boldsymbol{\sigma} + \lambda\overset{\square}{\boldsymbol{\sigma}} = 2\eta_v\boldsymbol{D}$	$N_1 > 0$ $N_2 \neq 0$
Diffusive Johnson-Segalman	$\boldsymbol{\sigma} + \lambda\overset{\square}{\boldsymbol{\sigma}} = 2\eta_v\boldsymbol{D} + \varepsilon\nabla^2\boldsymbol{\sigma}$ $\boldsymbol{\sigma} + \lambda\overset{\square}{\boldsymbol{\sigma}} = 2\eta_v\boldsymbol{D} + \varepsilon\nabla^2\boldsymbol{D}$	$N_1 > 0$ $N_2 \neq 0$ $N_1 > 0$ $N_2 \neq 0$
Phan-Thien-Tannar	$\exp\left(\pi\frac{\lambda}{\eta_v}\mathrm{tr}\left(\boldsymbol{\sigma}\right)\right) + \boldsymbol{\sigma} + \lambda\overset{\square}{\boldsymbol{\sigma}} = 2\eta_v\boldsymbol{D}$	$N_1 > 0$ $N_2 \neq 0$

The investigations in chapter 2 are based on the Johnson-Segalman model and those in chapter 3 are based on the Diffusive Johnson-Segalman model. The relevant models will naturally be corrected to account for the inclusion of non-isothermal effects.

1.2.4 Chemorheological fluids

In many reacting flow systems, it is possible for the fluid viscosity (in addition to the dependence on temperature, shear rate, etc.) to also depend on the rate of polymerization, as in the case of polymer foams. Chemo-rheology is therefore the study of the viscoelastic behavior of reacting systems, which incorporates chemical reaction, processing conditions and the network formation i.e. the so called gelling process as well as phase transition, see [46]. In reaction injection molding (RIM) of polyurethane foams for example, the foam viscosity can depend on pressure (p), temperature (θ), time (t), shear rate ($\dot{\gamma}$), polymerization/cure rate (α) and filler properties (F) in the case when it is reinforced with fiber, see Eq. (1.50):

$$\eta = \eta(\theta, p, \dot{\gamma}, t, F, \alpha). \tag{1.50}$$

In chapter 4, we present a computational investigation on the Chemo-rheology of self expanding polyurethane foams.

1.3 Motivation

This research is primarily motivated by the prevalence of relevant industrial applications of complex fluids coupled with the limited attention that the flow of these fluids has received in the literature especially under non-isothermal conditions. The biological and industrial applications are quite diverse and almost always, various degrees and forms of heat transfer processes due among other reasons to material transformations are involved. The intrinsic relationships between the heat transfer processes to volume expansion, wall slip and flow instabilities is also of fundamental significance. The comprehensive understanding of the correlations between the thermal response, rheological properties and flow behavior of such complex fluids is therefore essential. The relevant non-isothermal investigations associated with the flow of complex fluids has received very little attention as compared to related Newtonian flow investigations. For non-isothermal investigations of viscoelastic flows, this can be attributed in part to the fact that the relevant temperature constitutive models for viscoelastic systems are still a subject of current and ongoing research. We will limit our mathematical investigations to those already developed temperature and stress constitutive models, that have since been robustly tested experimentally and theoretically.

Chapter 2

Non-isothermal flow of reactive viscoelastic liquids in a lubricated pipe*

Abstract

This chapter focuses on the unsteady, axi-symmetric, non-isothermal flow of a viscoelastic Johnson-Segalman liquid in a lubricated pipe which allows for wall slip. In simple flows, the Johnson-Segalman constitutive model under certain conditions allows for a non-monotonic relationship between the shear stress and the rate of shear, hence, leading to shear banded flow phenomena. Wall slip has been conjectured to play a role or at least occur simultaneously with shear banding in certain cases. We investigate the relationships between wall slip and shear banding in non-isothermal pipe flow of a Johnson-Segalman fluid under axi-symmetric conditions and Arrhenius chemical kinetics. The wall slip in our investigation is postulated to arise, say, from

---

*The contents of this chapter are from Ireka and Chinyoka [55] wall lubrication; both constant and variable wall slip effects are here considered. The set of coupled nonlinear time dependent partial differential equations for the fluid velocity, temperature and viscoelastic stresses are solved via semi-implicit finite difference techniques. We discuss the effect of wall slip on the flow profiles while varying certain flow and fluid material parameters.

2.1 Introduction

Non-isothermal flow of reactive fluids exhibiting non-Newtonian rheology has recently gained remarkable research prominence. This is largely due to its profound industrial relevance, say in, polymer industries, petrochemical and food processing industries, petroleum engineering and pharmaceutics. In process industries (where such flows are employed), adherence to safety measures becomes pertinent, especially if the flow involves possible exothermic reactions. In such case, it becomes absolutely necessary to avoid thermal runaway in the flow system. Finite time thermal runaway resulting from increasing local temperature can lead to thermal explosions thereby damaging expensive materials and/or equipments. In an exothermic reaction system, when the heat generated within the system is more than the heat loss to the environment, thermal explosion may occur, this phenomena is summarized mathematically by the dimensionless Frank-Kamenetskii heat evolution parameter δ, which physically reflects the internal properties of the system. Thus, for reactive fluids under Arrhenius kinetics, the critical temperature is exceeded when the value of δ exceeds a critical value δ_{cr} as described in [12, 42]. Flow of reactive fluids under Arrhenius Kinetics has widely been studied, for instance, in [1] thermal explosion and critical parameters in flow of reactive viscous (Newtonian) fluids are investigated, with subsequent extensions [87] and [23, 24] to flow involving non-Newtonian fluids (including Generalized Newtonian Models and viscoelastic fluids). If the fluid type is of non-monotonic constitutive relation, whilst thermal runaway may occur when the value of δ exceeds its critical value, it can also be enhanced by shear banding phenomena [23], which is exhibited in the flow as regions of discontinuities in shear rates between interfaces of adjacent fluid layers. In gradient shear banding, which will be investigated herein, fluid layers adjacent to the walls tend to exhibit higher shear rates while the main flow in the bulk region is mostly plug.

In the analysis of flow of viscous fluids over solid boundaries, the well documented no-slip condition which stipulates that "fluid particles on a boundary wall stick to the wall and in particular, moves with the same speed as that of the boundary", has been shown not to hold in general [93, 96], especially for a class of polymeric fluids. Investigation on wall slip effects in the flow of linear viscous fluids through a channel [96], show that if the wall slip depends on both the shear and normal stresses, the velocity profile differs qualitatively from the case when it depends on the shear stresses alone. Experiments in simple shear of polymeric liquids reveal the existence of wall slip in polymer melts, with prediction of transition from a weak slip regime to a regime of strong slip (leading to a plug flow in the bulk), provided a critical stress value is exceeded [49, 77]. This prediction is confirmed to be true for a certain class of polymeric liquids [32, 47], with a possibility of estimating the critical stress value via experimentation. Wall slip dependence on flow parameters, such as temperature, wall shear stress, critical stress value, first normal stress difference, molecular weight e.t.c. has been researched extensively, this has led to the formulation of various slip models most of which are validated using experimental data, for instance, in [61] a unified model which predicts wall slip by either entanglement or de-bonding mechanism as well as reflect the temperature dependence of critical wall shear stress under certain experimental condition was developed and verified experimentally [62]. Several other interesting wall slip models can be found in the comprehensive review paper on wall slip of molten polymer by Hatzikiriakos [48] and the well documented account on wall slip modelling and measurements [51] by Archer.

Asides from experimental results, analytical approaches have equally been adopted to investigate effects of wall slip on the flows of viscoelastic fluids. Georgiou [44] carried out linear stability analyses on the channel flow of a viscoelastic fluid under wall slip conditions and showed that the combination of slip and elasticity could lead to self-sustained oscillations in the flow. The search for the causes of instabilities in flow of polymeric fluids has spurred significant research activity. Hence, in shear flow of polymeric fluids, it is believed that a possible explanations to the flow instability observed in such flows results from the emergence of wall slip which may occur either by chain disentanglement or de-bonding mechanisms at the wall - polymer interface [61]. In particular, under wall slip conditions, the sudden change in the boundary conditions resulting from an apparent detachment of the polymeric material from the wall can yield spurt phenomena in the flow field [66, 76]. Archer, [51], revealed that the violation of no-slip conditions on the wall in the flow of polymeric fluids can be attributed to the existence of slip as a result of (i) cohesive failure between fluid layers near the solid-liquid interface, (ii) depletion of more viscous components from fluid-solid interface in multiphase materials, (iii) shear banding or constitutive instabilities or (iv) if the stresses in the flow are greater than the adhesive strength of the liquid-solid interface. Also, Denn in his review paper, [30], discussed the existence of slip, it's mechanism and a possible relationship between slip and extrusion instabilities in the extrusion of polymer melts at a sufficiently high stress levels. Although the relationship between constitutive modeling and instability in simple flows of polymers does not have enough experimental evidence to support its existence, and the theory is also not yet well developed, some investigations on constitutive instability of viscoelastic fluids have shown a possible existence of this phenomena see for example [35, 38, 74, 95] and the excellent review paper by Larson [67]. From a constitutive instability point of view, it is shown that if a viscoelastic fluid exhibits a non-monotonic relationship between the shear stress and rate of shear, then in a pressure driven flow, provided critical values are exceeded, the sudden surge in the bulk region may be attributed to its constitutive relation [66]. This interplay between constitutive instabilities and boundary conditions is indeed a promising area of research [88]. In fact, it has been conjectured [8, 73, 88] that wall slip does seem to play a role or at least occurs simultaneously with shear banding.

In principle, non-monotonic constitutive relations may admit multiple weak steady state solutions in simple shear flows. Existence of such weak solutions in steady flow of fluids governed by the said non-monotonic constitutive relations is attributed to the infinite number of possible shear rate discontinuities/paths encountered [23, 43, 88], one of such constitutive model which is well documented in the literature is the Johnson-Segalman model [59]. Shear banding in isothermal flow of Johnson-Segalman fluids has been well investigated [40, 75, 82, 88]. As noted in these references, aside from the Johnson-Segalman model, several other fluid models exhibit shear banding phenomena in experiments, some other constitutive models which attempt to explain shear banding phenomena includes the Giesekus model with parameter $\alpha > 1/2$ and the Rolie-Poly model among others. In this investigation we focus attention on startup flows of fluids with the Johnson-Segalman model subject to zero initial condition. The fixed initial condition leads to unique shear stress selection under the different parameter values of interest to the current investigation.

Due to their elastic characteristics, viscoelastic fluids are known to possess the ability to store energy, hence, temperature changes in the flow of polymeric fluids should reflect (i) the energetic effects resulting from polymer orientation changes, (ii) entropic effects due to stress work and (iii) the effects of heat transfer by conduction [19, 54, 92, 114]. Chinyoka [20] and [19] showed computationally that the viscoelastic fluids (as described by the Oldroyd-B and Phan-Thien-Tanner constitutive models respectively) possess better thermal loading properties as compared to equivalent Newtonian fluids. It was demonstrated in these works that the higher resistance of the viscoelastic fluids to thermal runaway phenomena makes them better alternatives in exothermic lubricant applications or as coolants in heat exchangers. This conclusion however does not apply to all viscoelastic fluids, in [23] it was shown that the shear banded channel flow of Johnson-Segalman fluids with non-monotonic shear stress - shear rate relationships lead to larger temperature build up in the flow field as compared to Newtonian fluids.

This study is motivated by the lubricated pipelining results of Joseph and Renardy [60] and experiments involving surface coating of the interface between polymer melts and solid boundaries as discussed in [50, 62]. In [60], it was demonstrated that in pipeline transport of immiscible liquids of different viscosities, say, viscoelastic liquids and a less viscous fluid, a flow setup whereby the less viscous fluid migrates to the walls (acting as lubricants to the bulk flow of the more viscous fluids) emerges. According to Adams et al. [75], Boukany and Wang [14], Boukany et al. [13] and Wang [113] wall slip is very important in experimental investigations of shear banded flows of complex fluids. The interface between high and low shear rate bands is known to move in time. For flow models with a diffusion term under isothermal conditions, the work of Olmsted, Fielding and collaborators, see for example [82, 88], demonstrates that this interface has a small but non-zero width. The various issues that arise during shear banding as well as the possibility of various time scales, associated with the development of the finite width shear band related interfaces would require the use of adaptive meshing and time stepping algorithms to capture the relevant phenomena inside these interfaces. In our study, we omit diffusion terms in the constitutive relation of [88] and include non-isothermal effects, hence, the interface between high and low shear rate bands, under this condition, has zero width. We employ semi-implicit finite difference methods for the solution process of the unsteady and coupled nonlinear systems of partial differential equations. Our use of constant time and mesh sizes thus seems accurate enough to capture the relevant phenomena involved in each of the respective bands. For more comprehensive and interesting developments of generalized theoretical frameworks and illustrations of time dependent banding phenomena, we refer to the excellent review articles [82] and [41] respectively. The current study proceeds along similar lines as in [23], here, by assuming either constant or variable (shear dependent) wall slip [48, 61, 63], we investigate numerically (i) the effects of wall slip (surface coating/lubrication) on gradient shear banding and thermal runaway in the non-isothermal flow of fluid described by the Johnson - Segalman constitutive model in a lubricated pipe and (ii) the interplay between wall slip and shear banding. Being the first study involving non-isothermal viscoelastic shear banded flow with wall slip conditions, we hope our current investigation supplements the growing literature in this very important and interesting area of research.

2.2 Model formulation

The mathematical description of fluid flow broadly follows the conservation equations of mass, momentum and energy discussed in chapter 1, see Eqs. (1.1 - 1.3). As also noted in chapter 1, the physical properties and rheological behavior of the particular fluid may necessitate the inclusion of additional constitutive equations for either the viscosity or the stresses. In particular, the focus on viscoelastic fluids in this study means that we in turn have to include appropriate stress constitutive models to the set of governing equations. The viscoelastic stresses in this study follow the the Johnson-Segalman constitutive model, see Table: 1.2. The full set of governing equations relevant for this study thus includes the conservation equations for mass, energy and momentum, i.e. Eqs. (2.1), (2.2) and (2.3) respectively as well as the Johnson-Segalman stress constitutive equations (Eq. (2.5)).

We let $\boldsymbol{v}'$ represent the fluid velocity field, t' the time, μ_s the solvent viscosity, ρ the fluid density, P' the fluid pressure, c_p the specific heat capacity at constant pressure, T' the fluid temperature, $\boldsymbol{q}' = -\kappa \nabla' T'$ the heat flux vector, κ the thermal conductivity of the fluid, Q the heat released due to exothermic reaction, A the Arrhenius pre-exponential factor, C the residue concentration, E the activation energy, R the gas constant, Q'_D represents the dissipation function resulting from internal heat production, T_0 the initial fluid temperature, η_p the polymer viscosity and $\boldsymbol{\sigma}'$ the viscoelastic stress tensor.

The mass conservation equation reads,

$$\nabla' \cdot \boldsymbol{v}' = 0. \tag{2.1}$$

The momentum equations are,

$$\rho \frac{D\boldsymbol{v}'}{Dt'} = -\nabla' P' + \nabla' \cdot \boldsymbol{T}'. \tag{2.2}$$

Conservation of energy leads to,

$$\rho c_p \frac{DT'}{Dt'} = -\nabla' \cdot \boldsymbol{q}' + Q\,A\,C\,\exp\left(\frac{-E}{RT'}\right) + Q'_D. \tag{2.3}$$

The extra stress tensor, $\boldsymbol{T}'$ in Eq. (2.2) is the sum of Newtonian and viscoelastic contributions,

$$\boldsymbol{T}' = \mu_s \boldsymbol{D}' + \boldsymbol{\sigma}', \quad \text{with,} \quad \boldsymbol{D}' = \nabla' \boldsymbol{v}' + (\nabla' \boldsymbol{v}')^T, \tag{2.4}$$

where the viscoelastic stresses are governed by the Johnson-Segalman constitutive model, which has been corrected for thermodynamics, see for example [33],

$$\boldsymbol{\sigma}' + \lambda' \left(\overset{\square}{\boldsymbol{\sigma}'} - \boldsymbol{\sigma}' \frac{D}{Dt'} \ln \left[\frac{T'}{T_0} \right] \right) = \eta_p \boldsymbol{D}'. \tag{2.5}$$

Here, the derivative $\overset{\square}{\boldsymbol{\sigma}'}$ appearing in Eq. (2.5) is defined as,

$$\begin{aligned} \overset{\square}{\boldsymbol{\sigma}'} = \left(1 - \frac{\xi}{2}\right) \left[\frac{D}{Dt'} \boldsymbol{\sigma}' - \boldsymbol{\sigma}' \cdot \nabla \boldsymbol{v}' - (\nabla \boldsymbol{v}')^T \cdot \boldsymbol{\sigma}' \right] \\ + \frac{\xi}{2} \left[\frac{D}{Dt'} \boldsymbol{\sigma}' + \nabla \boldsymbol{v}' \cdot \boldsymbol{\sigma}' + \boldsymbol{\sigma}' \cdot (\nabla \boldsymbol{v}')^T \right] \quad . \end{aligned} \tag{2.6}$$

We introduce the following dimensionless variables and parameters to the governing equations;

$$\nabla = h\nabla', \; \boldsymbol{v} = \frac{\boldsymbol{v}'}{U}, \; t = \frac{U}{h} t', \; \boldsymbol{\sigma} = \frac{h}{\eta_r U} \boldsymbol{\sigma}', \; P = \frac{h}{U \eta_r} P',$$

$$T = \frac{T' - T_0}{\alpha T_0}, \; Q_D = \frac{h^2}{\eta_r U^2} Q'_D,$$

$$Re = \frac{\rho U h}{\eta_r}, \; Pr \; = \; \frac{c_p \eta_r}{\kappa}, \; Br = \frac{\eta_r U^2}{\alpha \kappa T_0}, \; We = \frac{\lambda_r U}{h}, \; \alpha = \frac{RT_o}{E},$$

$$\delta = \frac{h^2 QACE}{RT_0^2 \kappa} \exp(-\frac{1}{\alpha}),$$

where Re, Pr, Br, We, α and δ are respectively the Reynolds, Prandtl, Brinkman, Weissenberg numbers, activation energy and Frank-Kamenetskii parameters. U is a reference velocity, h a reference length scale and η_r represents the total reference viscosity. The total viscosity of the fluid is given by

$$\eta = \mu_s + \eta_p, \tag{2.7}$$

where μ_s and η_p are respectively assumed to take the form

$$\mu_s = \mu_{sr}\mu(T') \quad \text{and} \quad \eta_p = \eta_{pr}\mu(T'). \tag{2.8}$$

The constant quantities μ_{sr} and η_{pr} are reference solvent and polymer viscosities respectively, so that the total fluid viscosity can be written in the form $\eta = \eta_r\,\mu(T')$ where $\eta_r = \eta_{pr} + \mu_{sr}$. We will take β as the important ratio of polymer viscosity to the total viscosity, i.e. $\beta = \eta_{pr}/\eta_r$. The solvent viscosity can therefore be written as,

$$\mu_s = \eta_r\mu(T')(1-\beta). \tag{2.9}$$

It immediately follows that $\beta = 0$ corresponds to Newtonian fluid. The temperature dependence of viscosities and relaxation times follow a Nahme type law,

$$\mu(T') = \exp\frac{-(T'-T_0)}{T_0}, \qquad \text{and} \qquad \lambda(T') = \frac{T_0}{T'}\exp\frac{-(T'-T_0)}{T_0}. \tag{2.10}$$

The governing equations, Eqs. (2.1), (2.2) and (2.3), respectively for the conservation of mass, momentum and energy, in dimensionless form become,

$$\nabla\cdot\mathbf{v} = 0, \tag{2.11}$$

$$Re\frac{D\boldsymbol{v}}{Dt} = -\nabla p + \nabla\cdot\left(\mu(T)(1-\beta)\mathbf{D} + \boldsymbol{\sigma}\right), \tag{2.12}$$

$$RePr\frac{DT}{Dt} = \nabla^2 T + \delta\exp\left(\frac{T}{1+\alpha T}\right) + BrQ_D. \tag{2.13}$$

The non-dimensional Johnson-Segalman equations for the viscoelastic stresses reduce to,

$$\boldsymbol{\sigma} + We\lambda(T)\left(\overset{\square}{\boldsymbol{\sigma}} - \boldsymbol{\sigma}\frac{D}{Dt}\ln(1+\alpha T)\right) = \beta\mu(T)\mathbf{D}. \tag{2.14}$$

The dimensionless form of the dissipation function for the single mode Johnson-Segalman model (see for example [114]) is given as,

$$Q_D = \mu(T)(1-\beta)\mathbf{D} : \nabla \boldsymbol{v} + \gamma \boldsymbol{\sigma} : \mathbf{D} + (1-\gamma)\frac{\hat{G}}{2(1-\xi)^2 We \lambda(T)}(I_1 \; + \; tr(\boldsymbol{b}^{-1}) \; - \; 6). \tag{2.15}$$

The energy storing ability of the viscoelastic liquid is described by $0 \leq \gamma \leq 1$, so that $\gamma = 1$ corresponds to pure entropy elasticity, in which case the heat production reduces to that generated by stress work only. In the case where $\gamma = 0$, the internal heat production corresponds to energy elastic effect. Other values of γ yield a linear combination of the entropic and energetic effects. $I_1 = tr(\boldsymbol{b})$ where the conformation tensor $\boldsymbol{b}$ is related to the viscoelastic stress tensor $\boldsymbol{\sigma}$ by

$$\boldsymbol{b} = \frac{(1-\xi)}{\hat{G}}\boldsymbol{\sigma} + \boldsymbol{I}, \tag{2.16}$$

where $\boldsymbol{I}$ is the unit tensor. $\hat{G}$ is a material parameter depending on the fluid. The temperature dependence of viscosities and relaxation times in dimensionless form becomes,

$$\mu(T) = \exp(-\alpha T), \quad \text{and} \quad \lambda(T) = \frac{1}{1+\alpha T}\exp(-\alpha T). \tag{2.17}$$

2.2.1 Equations in cylindrical form

To solve the given problem using finite difference techniques, we adapt the governing equations to cylindrical coordinate systems (since the flow is through a pipe, see Fig. 2.1) with the flow velocity vector having components $\boldsymbol{v} = (0, 0, w(t, r))$ and temperature $T = T(t, r)$.

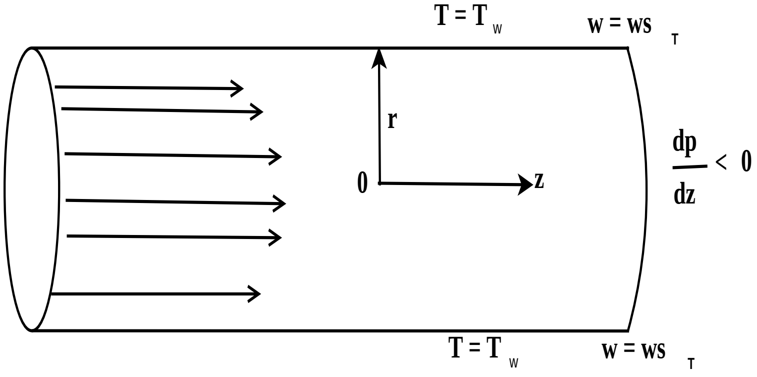

Figure 2.1: Schematic of the problem: ws_T and T_w are the total wall slip velocity and wall temperature respectively

The only non-trivial momentum equation in cylindrical coordinates reads,

$$Re\frac{\partial w}{\partial t} = -\frac{\partial p}{\partial z} + \frac{1}{r}[(1-\beta)\frac{\partial}{\partial r}(\mu r\frac{\partial w}{\partial r})] + \frac{1}{r}\frac{\partial}{\partial r}(r\sigma_{rz}), \tag{2.18}$$

subject to the initial and boundary conditions,

$$\begin{aligned} w(0,r) &= 0, \qquad 0 \leq r \leq 1, \\ w(t,1) &= ws_T \quad \frac{\partial w}{\partial r}(t,0) = 0, \qquad t \geq 0. \end{aligned} \tag{2.19}$$

The energy equation in cylindrical coordinates reduces to,

$$RePr\frac{\partial T}{\partial t} = \frac{1}{r}\frac{\partial}{\partial r}(\frac{\partial T}{\partial r}) + \delta\exp(\frac{T}{1+\alpha T}) + BrQ_D. \tag{2.20}$$

subject to the initial and boundary conditions,

$$\begin{aligned} T(0,r) &= 0, \qquad 0 \le r \le 1, \\ T(t,1) &= T_w, \quad \frac{\partial T}{\partial r}(t,0) = 0, \qquad t \ge 0. \end{aligned} \tag{2.21}$$

Here, $T_w = T_0 + \epsilon|\sigma_{rz}|_w$ is the wall temperature arising from friction associated with slip at the wall, where T_0 is a constant wall temperature, $\epsilon = k/\nu$, where $\nu > 0$ is the grafting density at the wall, k is a constant and $|\sigma_{rz}|_w$ is the magnitude of the wall shear stress, see [61].

The viscoelastic stresses are similarly obtained in cylindrical coordinates as,

$$\sigma_{rr} + We\lambda(T)[\dot{\sigma}_{rr} + (\xi - 2)\sigma_{rz}\frac{\partial w}{\partial r} - \frac{\alpha}{1+\alpha T}\sigma_{rr}\frac{\partial T}{\partial t}] = 0, \tag{2.22}$$

$$\sigma_{zz} + We\lambda(T)[\dot{\sigma}_{zz} + \xi\sigma_{rz}\frac{\partial w}{\partial r} - \frac{\alpha}{1+\alpha T}\sigma_{zz}\frac{\partial T}{\partial t}] = 0, \tag{2.23}$$

and

$$\sigma_{rz} + We\lambda(T)[\dot{\sigma}_{rz} + (\frac{\xi}{2} - 1)\sigma_{zz}\frac{\partial w}{\partial r} + \frac{\xi}{2}\sigma_{rr}\frac{\partial w}{\partial r} - \frac{\alpha}{1+\alpha T}\sigma_{rz}\frac{\partial T}{\partial t}] = \beta\mu(T)\frac{\partial w}{\partial r}. \tag{2.24}$$

The system of equations governing the stresses are hyperbolic in σ_{ij}, $i, j \in \{r, z\}$ and hence the imposition of boundary conditions will be inappropriate. The initial conditions for these stresses will be maintained at zero initial stress. To deal with the numerics for the stresses at the boundary, we employ a linear stress reconstruction technique [19, 20, 21, 22, 23, 24] at the outer wall and impose symmetry conditions at the pipe centerline. These initial and "boundary" conditions are given mathematically as follows;

$$\begin{aligned}\sigma_{ij}(0,r) &= 0, \qquad 0 \le r \le 1, \\ \frac{\partial \sigma_{ij}}{\partial r}(t, r_{n-1}) &= \frac{\partial \sigma_{ij}}{\partial r}(t, r_n^-), \quad \frac{\partial \sigma_{ij}}{\partial r}(t,0) = 0.\end{aligned} \tag{2.25}$$

In Eq. (2.25) r_n and r_{n-1} respectively represent the mesh positions at the wall and just below the wall. The superscripted derivative, $\partial\sigma_{ij}/\partial r(t, r_n^-)$ and $\frac{\partial \sigma_{ij}}{\partial r}(t, r_{n-1})$ respectively indicates backward differentiation from the wall and central differences, under the finite difference framework. We refer the reader to appendix A.13 for details of the discretization technique including a comprehensive description of how the Neumann Boundary conditions are handled numerically. In section 2.4, we validate the qualitative behavior of our numerical scheme against existing results in the literature which are special cases to our current investigation. The main results of this chapter follow in section 2.5 and these are based on the wall slip models developed in section 2.3.

2.3 Wall slip model

2.3.1 Case 1: Viscous Newtonian fluid

As a special case to our current study, we investigate wall slip in a viscous Newtonian fluid model (which is easily obtained from the Johnson - Segalman fluid model, by simply switching off some parameters). We consider a wall slip model that allows for both constant slip (arising from, say, the presence of lubricant along the pipe walls) and variable slip, which depends on the magnitudes of the normal and shear stresses at the wall. Denoting the wall shear stress by ζ_w, the wall normal stress by χ_w and the total wall slip by ws_T, we thus assume that:

$$ws_T = f(\zeta_w, \chi_w), \quad \zeta_w = [\sigma_{rz}]_{r=1}, \quad \chi_w = [\sigma_{rr} + \sigma_{zz}]_{r=1}, \tag{2.26}$$

for some continuous function f which relates the slip velocity to the wall stresses. We adopt the form of wall slip theory developed in [96] wherein the slip velocity is assumed to depend on both the shear and normal stresses and the stress relation defined by the variable Ω as:

$$\Omega = \frac{\zeta_w}{\chi_w}.$$

According to [96], the fluids slips at the wall for large Ω but does not slip for very low values of Ω. The slip velocity function used in [96] is of the form,

$$ws_T = w_l, \qquad \Omega < \Omega_0 \tag{2.27}$$

$$ws_T = \frac{w_l + w_h}{2} + \frac{w_l - w_h}{2} \sin\left(\frac{\Omega - \Omega_0}{\Omega_1 - \Omega_0}\pi + \frac{\pi}{2}\right), \qquad \Omega_0 \leq \Omega \leq \Omega_1, \tag{2.28}$$

$$ws_T = w_h, \qquad \Omega > \Omega_1, \tag{2.29}$$

where w_s is the slip velocity and $w_h \geq w_l$ are the limiting values of ws_T for high and low values of Ω respectively. For lubrication applications, we will limit attention to $w_l > 0$ and $\Omega < \Omega_0$.

2.3.2 Case 2: Viscoelastic Johnson - Segalman fluid

As earlier mentioned, provided the wall shear stress exceeds a critical value, viscoelastic fluids slips over solid interface. Several slip models have been developed but observations from experiments propose that the slip velocity depends not only on the normal and shear stresses at the wall but also on the fluids' immediate past state, this is in line with the concept of fading memory of viscoelastic fluids. We wish to introduce a model that accommodates a constant slip as a result of a wall lubrication/coating so that the slip model will be of the form

$$ws_T = w_l + w_s, \tag{2.30}$$

here w_s is the wall slip resulting from material entanglement and de-bonding and w_l is the wall slip as a result of lubricant/coating. To capture slip relaxation effects in the transient flow problem currently investigated, we use a dynamic slip model for w_s outlined in [48], which is obtained in dimensionless form as:

$$w_s + \alpha_1 We\lambda(T)\frac{dw_s}{dt} = \alpha_2((1-\beta)\mu(T))^m {\sigma_w}^m \tag{2.31}$$

subject to the initial condition

$$w_s(t) = 0, \qquad t \leq 0, \tag{2.32}$$

where $\alpha_1 We\lambda(T)$ is the dimensionless slip relaxation time at the wall, α_1 and $\alpha_2 = \frac{1}{k^*}$ are constants, where k^* is the coefficient of dynamic friction on the wall, $m \in \{2, 4, 6\}$ (depending on the structure of the molten polymer) is the slip power law exponent and σ_w is the wall shear stress. α_1 is a scaling parameter to distinguish the slip relaxation time $\alpha_1 We\lambda(T)$ in Eq. (2.31) from the fluid relaxation time $We\lambda(T)$.

2.4 Numerical validation

As this study is the first investigation on non-isothermal viscoelastic shear banded flow with wall slip conditions, we attempt to validate the qualitative behavior of our numerical scheme against existing results in literature which are special cases to our current investigation. We first consider the viscous Newtonian fluid case (section 2.3.1). By switching off viscoelastic fluid parameters and heat generation terms in our model i.e $We = 0$, $\gamma = 0$, $t = 10$, $\beta = 0$, $\delta = 0$, $Br = 0$, under slip conditions, say, due to wall lubrication (i.e. $\Omega < \Omega_0$ and $ws_T = w_l = 0.05$), our velocity profile agrees qualitatively with that obtained in [96], see Fig. 2.2, For a viscoelastic Johnson-Segalman fluid as in [23] under no slip and isothermal wall conditions, $w_h = 0$ and $T_w = 0$ respectively, considering the following parameters value: $\xi = 0.8$, $\beta = 0.95$, $\hat{G} = 10^{-3}$, $\delta = 0.5$, $\alpha = 0.1$, $Br = 1$, $Pr = 1$, $\Delta r = 0.001$, $\Delta t = 0.005$, $t =$

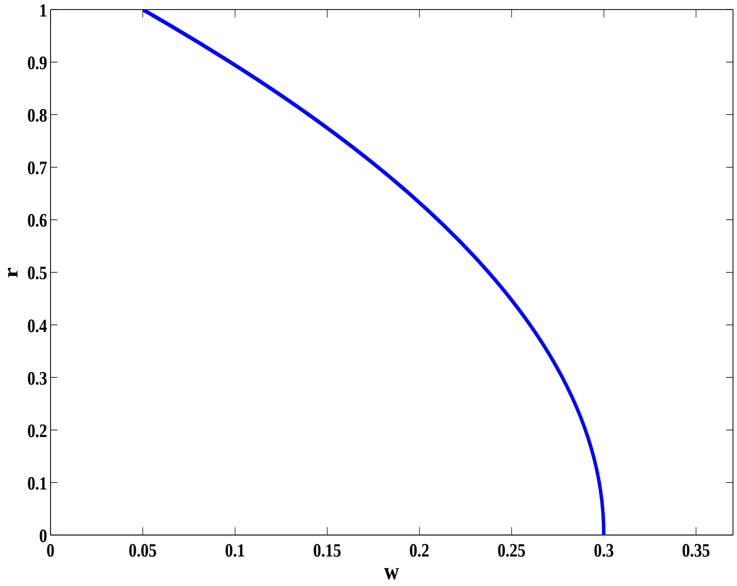

Figure 2.2: Velocity profile for viscous Newtonian fluid model

10 and subject to a constant pressure gradient,

$$G = -\frac{\partial p}{\partial r} = 1,$$

When $We = 2$ and $\gamma = 0$ we observe that our profiles are in qualitative agreement

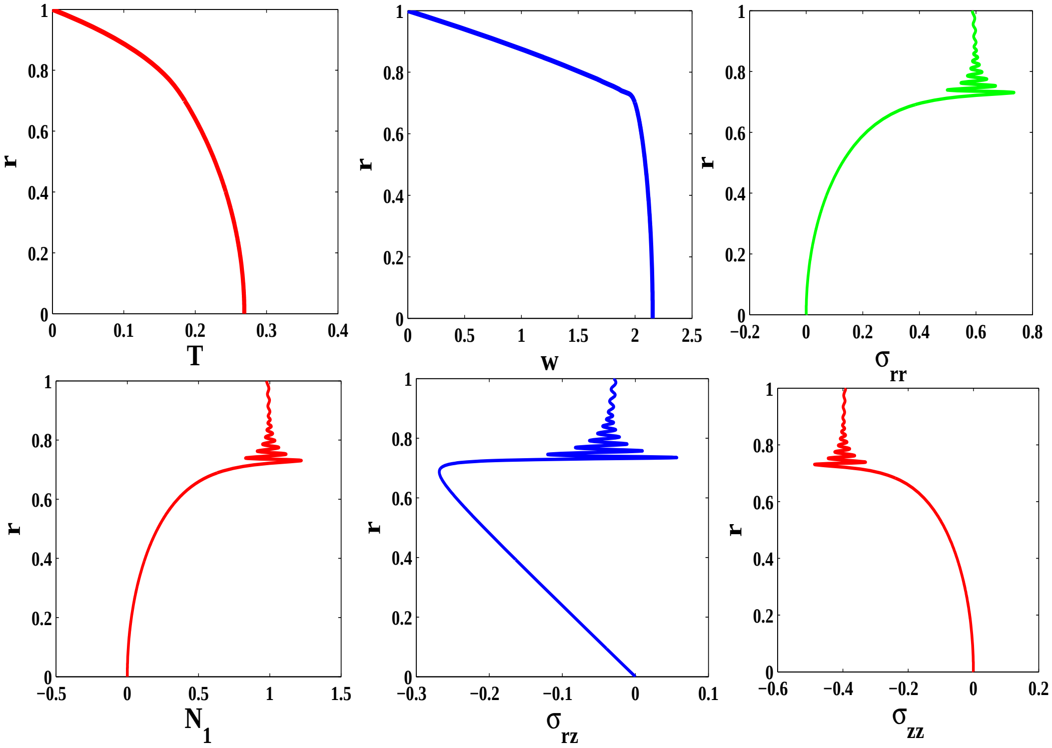

Figure 2.3: Development of shear bands with $We = 2$, $\gamma = 0$, $w_s = 0.0$ and $t = 10$.

with those given in [23] under similar conditions, albeit for channel flow, see Fig. 2.3. We also note that the plug flow observed in the bulk as described in the velocity profile (w) of Fig. 2.3 and the non-zero first normal stress difference N_1 agrees with results for related nonlinear viscoelastic fluids in literature, where the elastic effects dominate the viscous effect for $We > 1$. As illustrated in [23], the Gibbs-like oscillations observed in Fig. 2.3 are simply transient effects which disappear in the steady state.

2.5 Results and discussion

The discretized model equations are simulated with or without wall slip, under isothermal and non-isothermal wall temperature. Except otherwise stated we use the following parameter values: $Re = 1, G = 1, We = 2, \gamma = 0, T_0 = 0, \xi = 0.8,\ \beta = 0.95,\ \hat{G} = 10^{-3},\ \delta\ =\ 0.5,\ \alpha = 0.1,\ Br = 1,\ Pr\ =\ 1,\ \Delta r = 0.01,\ \Delta t = 0.005,\ t = 50, \epsilon = 0.05, k^* = 0.01, \alpha_1 = 0.5, w_l = 0.05, m = 2$.

2.5.1 Shear dependent wall slip and Temperature

With the dynamic slip model as envisioned in [48] i.e. Eq.(2.31) and wall temperature dependence on shear stress, we investigate the correlation between shear banding (viscoelastic effects) and wall slip (shear dependent wall and pipe lubrication/surface coating) as in Eq. (2.30), with $w_l = 0.05$, via numerical experimentations under isothermal and non-isothermal wall temperature. Our simulation updates the boundary conditions for both the velocity and temperature profiles at each time step so that T_w and ws_T assumes a new value at every time step. The emergence of shear bands is symbolized by the inception of Gibbs-like oscillation as illustrated in Fig. 2.4 at $t = 10$. The gradient shear bands manifest as shear rate discontinuities characterized by high shear rates close to the walls and a plug type flow in the bulk fluid, see Fig. 2.5. In our investigations, shear banding phenomena was observed for both isothermal and non isothermal wall temperature cases under slip and no slip conditions at the walls.

The results displayed in Fig. 2.4, in which the shear stress decreases with increases in either or both wall temperature and slip, are in agreement with experimental evidence. For example the experimental observations of Joshi [62], show that presence of wall slip and increase in wall temperature lead to a decrease in the critical stresses for

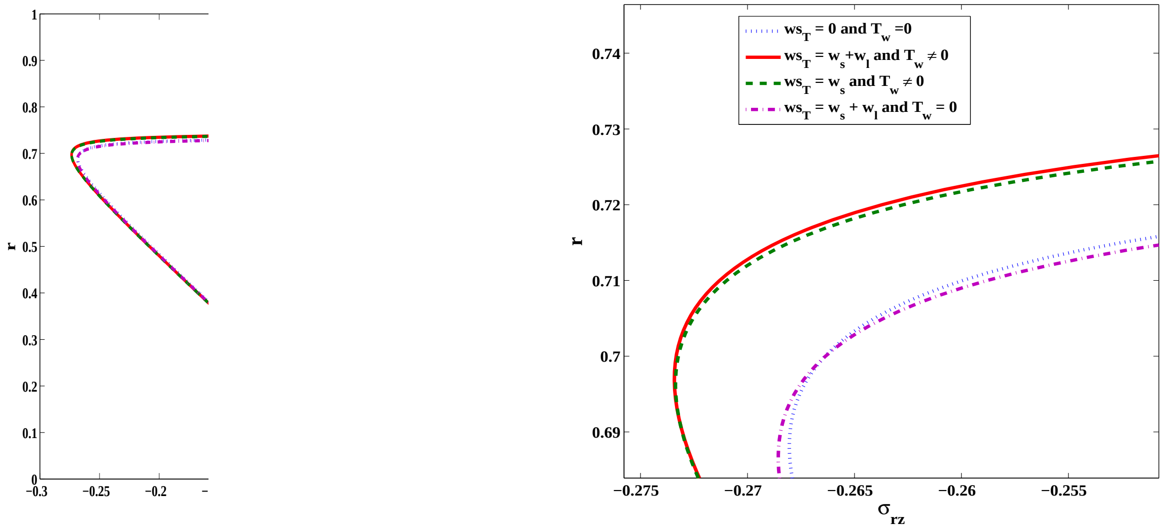

(a) (b)

Figure 2.4: (a) Onset of Shear banding under isothermal and non-isothermal wall

(b)

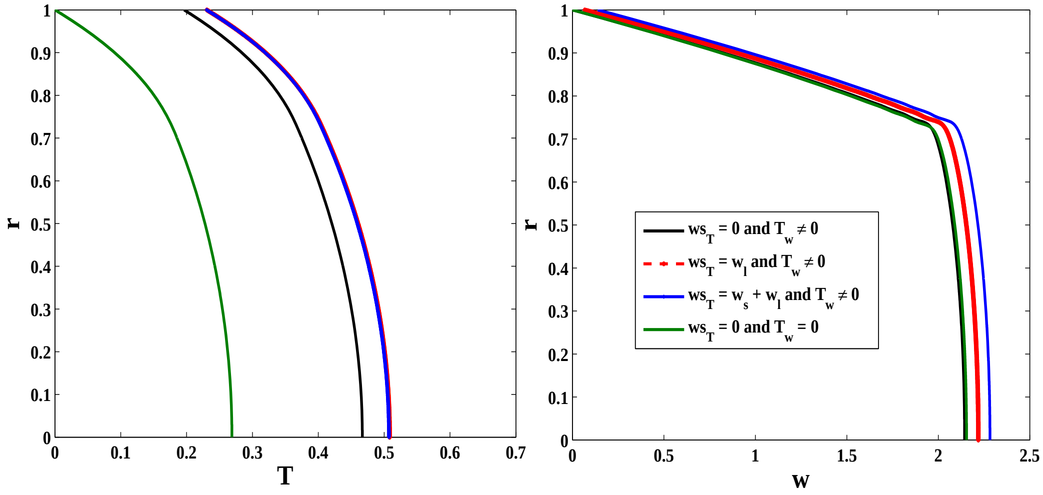

Figure 2.5: Influence of shear dependent wall slip or no slip conditions on flow profiles under isothermal and non-isothermal wall temperature for $We = 2$.

certain classes of polymeric fluids. In Fig. 2.5, the temperature of the system as well as the flow velocity in the bulk is expectedly shown to increase in the presence of wall slip and non-isothermal wall temperatures.

2.5.2 Parameter dependence

From an industrial applications perspective, the possibility of the occurrence of thermal runaway phenomena is extremely important. Sensitivity of the relevant viscoelastic fluids to thermal instabilities under Arrhenius kinetics becomes a central issue. The admissible range of values for the Frank-Kamenetskii parameter (δ) for which the system will remain thermally stable can be inferred from our computational

y

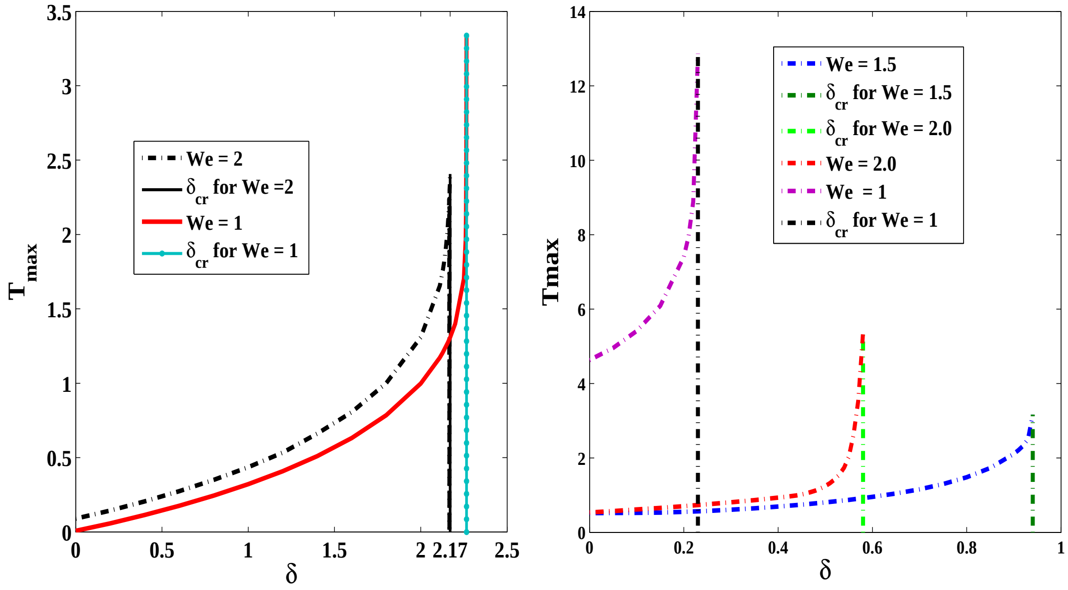

Figure 2.6: (a) T_{max} versus δ at $t = 50$, $ws_T = 0$, $Re = 1$ and $T_w = 0$ (b) Graph of T_{max} against δ at $t = 50$ with $ws_T \neq 0$ and $T_w \neq 0$.

strongly influences the thermal loading properties. For example Fig. 2.6(a), under isothermal wall temperature and no slip conditions, shows the dependence of the critical Frank-Kamenetskii parameter (δ_{cr}) on fluid viscoelasticity and Fig. 2.6(b) explores a similar relationship under non-isothermal wall temperature and slip conditions. In Fig. 2.6(a), we notice as was reported in [23] under no-slip conditions,

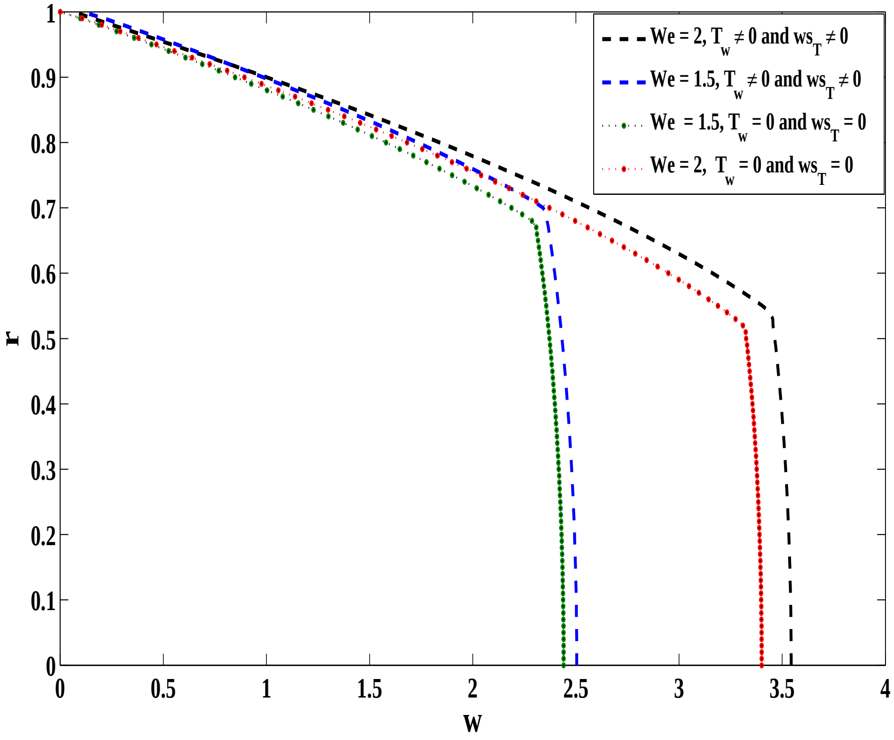

Figure 2.7: Velocity profiles for varying We, at $t = 50$.

that in the presence of shear banding, higher fluid viscoelasticity (i.e. higher We) leads to increased susceptibility to thermal runaway, i.e. lower δ_{cr}. Fig. 2.6(b) shows that the inclusion of wall slip and related non-isothermal wall temperature conditions leads to a more complex relationship between fluid viscoelasticity and the related the critical Frank-Kamenetskii parameter values. We conjecture that in this case, the energy storing ability of the viscoelastic fluids becomes important. In particular, the low viscoelasticity in the cases under which no shear banding is observed ($We \leq 1$) means less energy can be stored but instead is released as heat to the fluid leading to the faster and higher temperature buildup an hence the resultant low δ_{cr} values

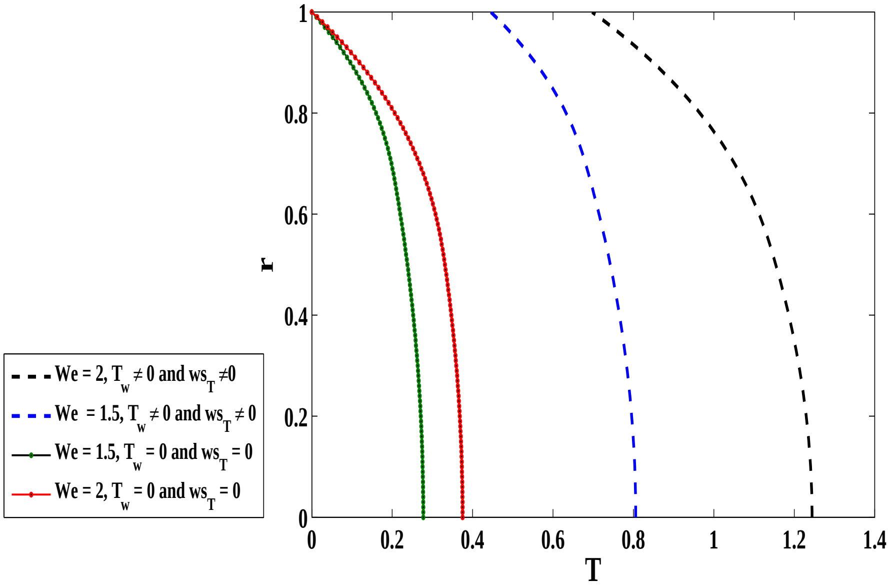

Figure 2.8: Temperature effects varying We, at $t = 50$.

as compared to the higher We cases. Increased fluid viscoelasticity (i.e. $We > 1$) leads to (i) less heat generation but more energy storage and hence lower temperature buildup and higher δ_{cr} values compared to the weaker viscoelasticity cases and (ii) the emergence of shear banded solutions and hence similar behavior to that observed in Fig. 2.6(a) in which higher We lead to lower δ_{cr} values. Figs. 2.7 and 2.8 show the influence of wall slip and non-isothermal wall temperature on the fluid velocity and temperature. It is observed that the fluid temperature increases significantly with fluid viscoelasticity with also a gradual increase in the bulk velocity observed under similar conditions.

The increased volume flow rates and fluid temperature observed in Figs. 2.7 and 2.8 respectively necessitates an investigation into the strength of the driving force, i.e. the magnitude of the pressure gradient. In Fig. 2.9, we investigate the effects of varying pressure gradient G, which in [23] and has thus far in the current work been assumed to be constant at $G = 1$. With the value $We = 2$ under which shear

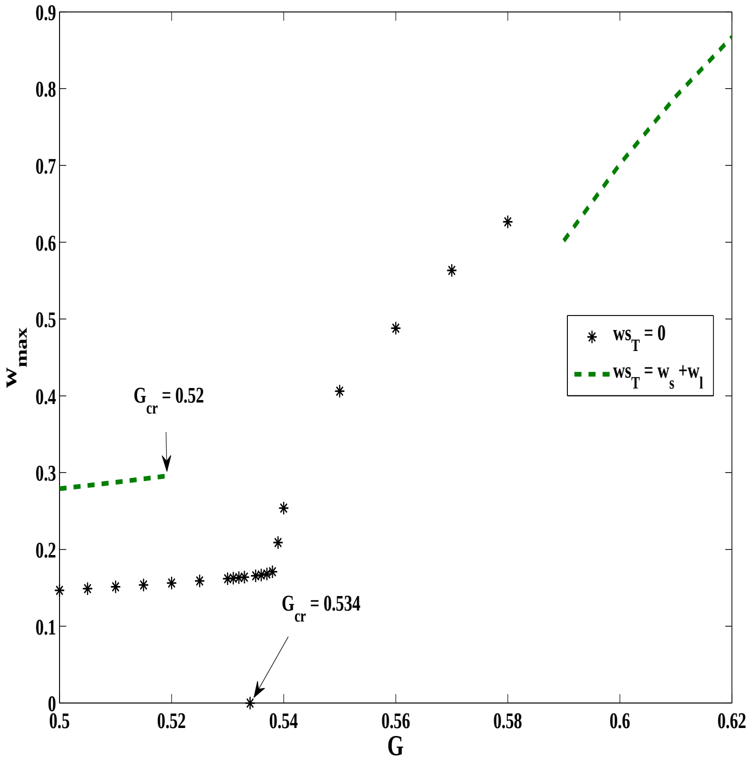

Figure 2.9: $w_{\max}$ varying G for $We = 2$ and $t = 50$, $T_w \neq 0$ and $ws_T \neq 0$.

banding is observed in the flow if $G = 1$, we notice the existence of a critical pressure gradient, G_{cr}, below which no shear banding occurs (with or without wall slip) and above which shear banding sets in leading to large increases in the volumetric flow rates, see Fig. 2.9.

The results of Fig. 2.9 clearly suggest that for each physically appropriate value of We, there should exist at least a critical pressure gradient G_{cr} as described above. In view of applications to pipeline transport of reactive complex liquids, with or without lubricated walls, this result suggests reducing the pumping pressures as a means of alleviating shear banding and the associated effects of thermal runaway. As expected, the results of Fig. 2.9 show that the critical pressure gradient is higher in the no-slip case than under wall slip conditions since the wall slip would naturally contribute to the volume flow rates, in addition to the contributions from the driving pressure

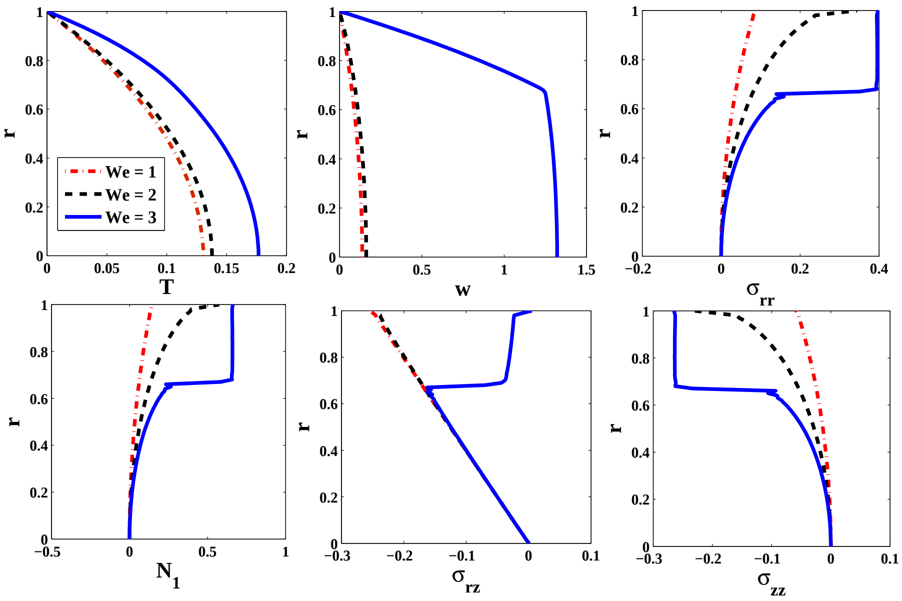

Figure 2.10: Flow profiles for varying We at $t = 50$ with $G = 0.532$ under slip and non-isothermal wall temperature condition.

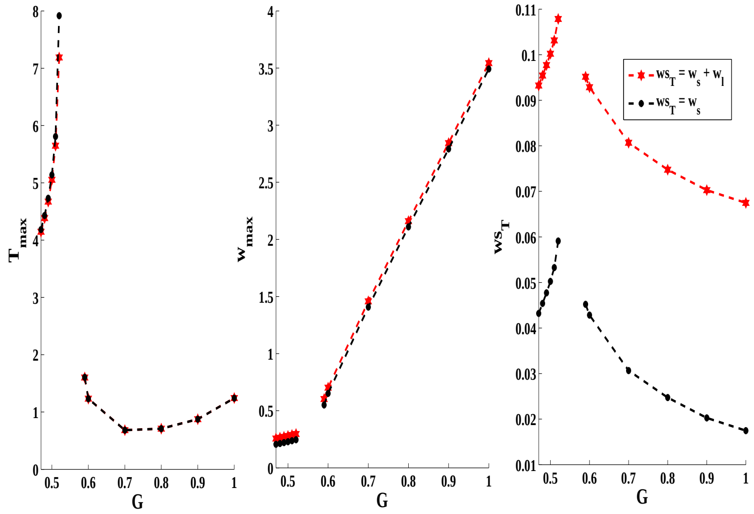

Figure 2.11: Effect of varying pressure gradient on (a) temperature, (b) velocity and (c) wall slip values for $We = 2$, and $T_w \neq 0$.

forces. Fig. 2.10 illustrates the expected elimination of shear banding in the flow profiles under the action of subcritical pressure gradients.

We conclude by showing the effects of lubrication/coating wall slip as well as shear dependent slip acting collectively or severally. Fig. 2.11 shows that at relatively low values, the combined or individual effects of these wall slip mechanisms on the flow quantities is roughly similar. In particular, at low strengths lubrication and/or surface coating has similar effects on shear banding phenomena to slip effects resulting from material disentanglement or de-bonding.

2.6 Conclusion

We have computationally investigated the effects of wall slip (due to surface coating and/or lubrication as well as resulting from wall shear stresses) on gradient shear banding and thermal runaway in the non-isothermal flow of fluid described by the Johnson-Segalman constitutive model in a pipe. The interplay between wall slip and shear banding was also investigated and our results demonstrate an interdependence of wall slip and shear banding. We showed that the presence of wall slip and non-isothermal wall temperature reduces the magnitude of the wall shear stresses, in line with experimental observations. The dependence on wall slip of wall temperature is also illustrated. In particular, the fluid temperature is demonstrated to increase with wall slip and hence susceptibility to phenomena such as thermal runaway is also increased.

Our results also indicate that, at low strengths, lubrication and/or surface coating has similar effects on shear banding phenomena to slip effects resulting from material disentanglement or de-bonding. We have also demonstrated an admissible range of values for pressure gradient. Values of the pressure gradient below certain critical thresholds were shown to significantly delay the onset of shear banding phenomena normally observed at higher pressure gradients. We have also demonstrated the dependence of thermal loading properties of the fluid to the fluid viscoelasticity in the presence or absence of wall slip. Under conditions of shear banding, it is shown that higher fluid viscoelasticity leads to lower critical Frank-Kamenetskii parameter values and hence also to increased susceptibility to thermal runaway phenomena.

Chapter 3

Shear banding phenomena in flow of polymeric fluids under non-isothermal conditions*

Abstract

In this chapter we investigate phenomena associated with shear banded flows of viscoelastic fluids in both pipe and coaxial annular flow. We in particular computationally analyse the effects of stress diffusion, non-isothermal flow conditions and annular gap size on the shear stress path selection (and the selected shear stress value) in shear banded flow of viscoelastic fluids described by the non-local Diffusive Johnson-Segalman (DJS) constitutive model. The DJS model is one of such constitutive models which allows for a non-zero inter-facial layer between regions of high and low shear rates within the flow field. Temperature effects due to polymer orientation changes, entropic effects (resulting from stress work), conduction heat

---

[*] The contents of this chapter are from Ireka and Chinyoka [56]

transfer, Arrhenius chemical kinetics as well as the influence of slip and related frictional heating on the wall are all accounted for. The time dependent model formulated to capture gap effect in the axial annular flow problem (under certain values of the relevant parameters), reduces to the system of equations governing a pipe flow setup. Semi-implicit finite difference methods are also employed for the solution process of the coupled nonlinear time dependent partial differential equations governing the flow problem. We discuss with graphical representations the effect of temperature, stress diffusion, wall slip, suction/injection and annular gap size on the related shear rate path selection phenomena for certain material parameter values.

3.1 Introduction

Industrial relevance of macromolecular fluids and their commercial viability have led to increased research activity and interest in the dynamics of these complex fluids. One such flow problem which has attracted significant theoretical and experimental research activity is the flow of viscoelastic fluids through annular duct. This is mainly due to its vast application in several industrial processes such as oil extraction and drilling, plastic extrusion, journal bearings, wire coating, annular heat exchangers in food processing etc. The theoretical analyses have been conducted for various fluid models capable of predicting, to a certain extent, the complex dynamics of non-Newtonian fluids under shear. Fluid models such as the Bingham model, Power law model, Oldroyd-B model, Johnson-Segalman model, Phan-Thien-Tanner model and the Geisekus model, have all been used by various authors, see for example [2, 11, 37, 81, 83, 94, 99, 106], to investigate flow patterns/profiles or volumetric flow rate in annular flow of non-Newtonian fluids under certain physical conditions.

Due to their macromolecular and viscoelastic nature, polymeric fluids when subjected to an imposed shear stress (such that a critical relaxation time is exceeded) exhibit certain flow instabilities [51]. These instabilities emerge within the flow as shear bands or fluid layers flowing with different internal configuration and apparent viscosities, coexisting and separated along the normal to the flow direction [88]. This phenomena of "gradient banding" in flow of complex fluids has been widely investigated both theoretically and experimentally, see for example [39, 75, 88, 117]. As stated in chapter 2, the onset of shear bands in simple shear flow of complex fluids can be attributed to multiple weak steady state solutions of the fluid's constitutive relation resulting from a non-monotonic shear stress - shear rate relationship, with the region of negative slope representing an unstable regime within the flow [108]. These non-monotonic constitutive relations have been observed to possess inherent history-dependence which could be resolved by introducing diffusion terms [91]. Several fluid models exhibiting this phenomena, while offering good comparison with experimental data, include Giesekus model [45], Rolie Poly model [71], the VCM model [110] and Johnson-Segalman (JS) model [59] amongst others. Relevant flows of fluids described by these models have been extensively investigated under both isothermal conditions, see for example [27, 28, 29, 39, 53, 88] (and the references therein) and non-isothermal conditions [23, 55].

Studies have demonstrated that in order to ensure a mechanism to select a unique shear stress at which shear banding will occur, one will need to incorporate non-local terms into the equations governing the stresses (i.e. those formulated in [45], [59] and [71]) see for example [53, 88]. In this study, we focus on the Johnson-Segalman model which in its original form, has no mechanism to ensure selection of the unique shear stress at which shear banding will occur. Experimentally, however, the selected shear stress (and hence shear rate path) is usually observed to be independent of flow history and initial conditions [88]. With the addition of diffusion term in the

JS model investigated in chapter 2, the resulting Diffusive Johson-Segalman (DJS) model is capable of predicting the experimentally observed unique total stress at which shear banding occurs. This model has been proposed either with polymer stress diffusion [72] or shear rate diffusion [119]. It is important to note that the total stress corresponds to the stress at which the interface between shear bands is stationary, and the diffusion terms which determines the non-zero inter-facial width, describes nonlocal relaxation of the viscoelastic stresses necessary for describing strongly inhomogeneous flow profiles. For a detailed explanation on stress selection phenomena in shear banded flows, we refer the reader to the comprehensive review paper of Olmsted [88].

The small diffusion coefficient introduced in this investigation makes a significant difference in the behavior of the shear stress - shear rate curves around the regions of non-monotonicity. Away from the regions of non-monotonicity, the shear stress - shear rate curves are otherwise unaffected by the addition of stress (or shear rate) diffusion. Physically, the stress diffusion terms contribute to particle diffusion across inter-facial layers between the bands and hydrodynamic interactions within each band. However, recent study has shown that this phenomena can be accounted for more explicitly without stress diffusion [29].

As earlier mentioned (chapter 2), in modeling flow of viscoelastic fluids, it is important to accommodate their energy storing ability. For instance, in the flow of polymeric fluids, effects such as (i) energetic effects due to polymer orientation changes, (ii) entropic effects resulting from stress work and (iii) conduction heat transfer effects, should be accounted for in the models, [11, 33, 54, 92, 114]. In fact, it has been shown that non-isothermal wall conditions affects the magnitude of wall shear stress [55, 62]. Another important phenomena which significantly contributes to instabilities in flow of polymeric fluids is wall slip, see [48, 51, 55] and the references therein.

Investigations on the interplay between temperature effects, wall slip and shear banding reveal an interdependence of non-isothermal conditions, wall slip and shear banding [55].

The current investigation is motivated by relevant applications of annular flow of viscoelastic fluids as well as the experimental results of Olmsted [75] where it was established that confinement and boundary conditions influence nonlocal effects in flows of worm-like micellar, and the work of Cromer et al [28], where pressure driven flow of worm-like micellar solutions through rectilinear micro-channels was investigated using the VCM model. Our study incorporates polymer stress diffusion into the stress constitutive relations of Johnson Segalman model, as suggested by [72], instead of the shear rate diffusion type of [119] which was also adopted in [75]. However, introducing stress diffusion warrants that the stress relations are solved subject to a new set of boundary conditions; i.e. the stress equations becomes parabolic instead of hyperbolic. We formulate the model for the annular flow problem and include a gap parameter χ, which when set to 1, reduces the model to the set of equations governing a pipe flow. For the pipe flow problem, we assume the stresses to be zero at the axis (i.e. at $r = 0$, which corresponds to a steady state solution of the total stress from the momentum equations as $r \rightarrow 0$ at constant axial pressure gradient), and then take the gradient of the stresses at the wall along the outward normal to be zero, as in [88]. For the annular flow problem, we also take the gradient of the stresses at the walls, along the outward normal to be zero. The emerging unsteady nonlinear coupled partial differential equations are solved via semi implicit finite difference techniques. Most importantly, our aim in this study is to investigate possible effects of annular gap size, polymer stress diffusion, fluid injection through the inner pipe, non-isothermal and wall slip conditions on the selected shear stress for a polymeric fluid described by the DJS constitutive model. We discuss with graphical illustrations these influence on the flow profiles.

3.2

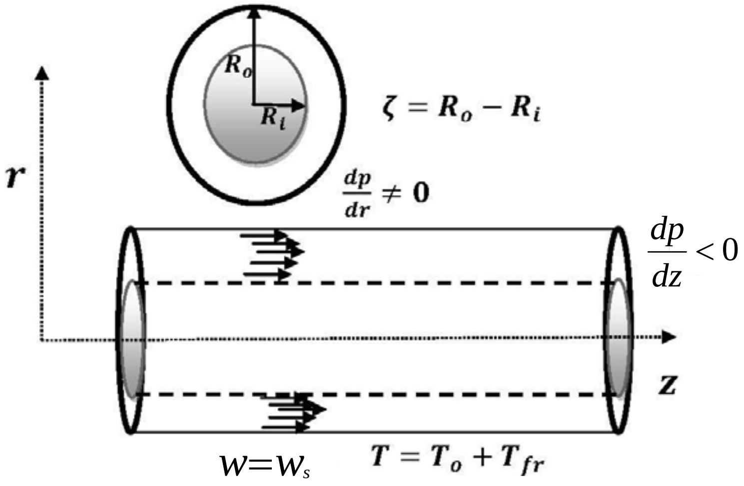

Figure 3.1: Geometry of the flow problem

We consider a start-up pressure driven flow of an incompressible, reactive viscoelastic fluid governed by the DJS model under Arrhenius kinetics, through a coaxial annular pipe with gap size $\zeta = R_o - R_i$, oriented such that the axis of the pipes of radius R_o and R_i $(R_o > R_i)$ representing the outer and inner radius respectively, coincides with the z axis. The flow is such that the velocity, temperature and stresses vary only in the radial direction (along the normal to the wall), with time. The flow direction is parallel to the $z - axis$, i.e. the common axis of the pipes. The wall temperatures also change as a result of frictional heating (T_{fr}) and the fluid exhibits slip on the wall (w_s). We further include the possibility of fluid injection (through the inner pipe into the annulus region), allowing for ejection/suction of the same fluid through the outer pipe, as described in the Fig. 3.1.

Noting that $R_i > 0$ corresponds to coaxial annular flow problem and that $R_i = 0$ corresponds to pipe flow, we define the annular gap ζ as

$$\zeta = \begin{cases} R_o & \text{if} \quad R_i = 0, \\ \\ R_o - R_i = R_o\left(1 - \frac{R_i}{R_o}\right) = R_o\left(\frac{k-1}{k}\right) = \frac{R_o}{\chi}, & \text{if} \quad 0 < R_i < R_o, \end{cases}$$

where the dimensionless parameters k and χ are defined by

$$k = \frac{R_o}{R_i} > 1 \quad \text{and} \quad \chi = \frac{k}{k-1} > 1 \qquad \text{for} \quad 0 < R_i < R_o.$$

Defining $\chi = 1$ when $R_i = 0$ shows that $\zeta = R_o/\chi$ for all relevant values of $\chi \geq 1$.

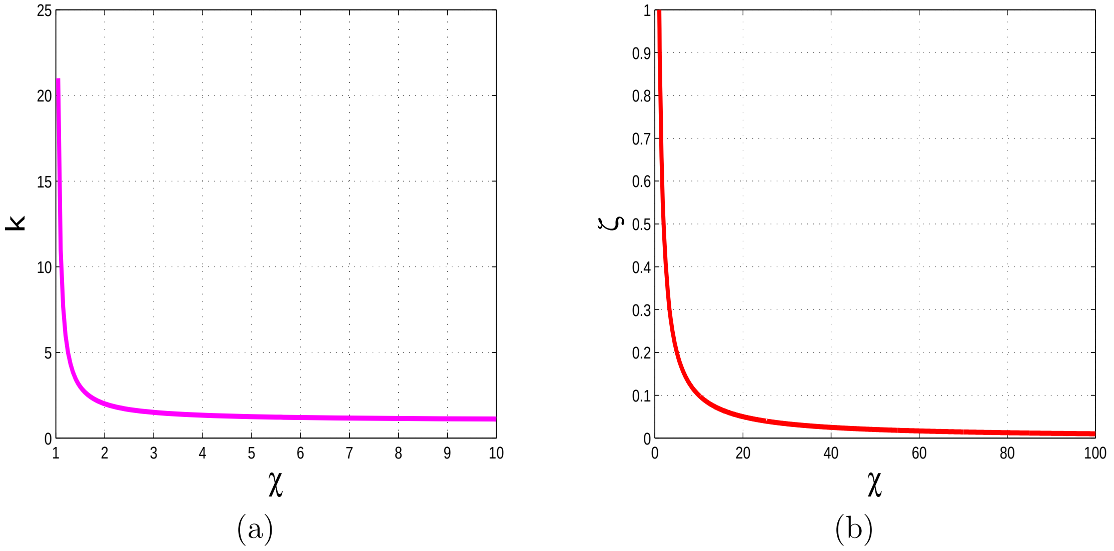

(a) (b)

Figure 3.2: Behavior of χ against (a) radii ratio k and (b) annular gap size ζ, say for $R_o = 1$.

It is evident either from Fig. 3.2 or from the mathematical definitions that an increase in the value of χ corresponds to a reduction in the gap size ζ, or alternatively corresponds to the situation where the magnitude of the radii become close, i.e.

$R_i \to R_o$.

The governing equations for the flow are derived from the conservation of mass, momentum and energy, given repectively as Eqs. (2.1), (2.2) and (2.3). To account for possible fluid injection/suction through the walls, we define $\boldsymbol{v}'$ by

$$\boldsymbol{v}' = u'(r', t')\hat{e}_r + w'(r', t')\hat{e}_z, \tag{3.1}$$

where $u' = b/r'$ (b is a constant) chosen so that Eq. (2.1) is satisfied. We note that b vanishes in the absence of fluid injection/suction. In order to account for the non-zero radial pressure observed in axial annular flows, the total pressure in this case is given by $P'(r, z) = h'(z) + p'(r)$, where $h'(z)$ and $p'(r)$ are the pressure in the axial and radial directions respectively, It is necessary to note that when the problem reduces to that of pipe flow, i.e. $\chi = 1$, we assume dominance of the axial pressure over the radial pressure, so that $P'(z) = h'(z)$.

The viscoelastic stress constitutive equations here are governed by the DJS model with polymer stress diffusion, given by

$$\boldsymbol{\sigma}' + \lambda' \left(\overset{\square}{\boldsymbol{\sigma}'} - \boldsymbol{\sigma}' \frac{D}{Dt'} \ln(\frac{T'}{T_o}) \right) = \eta_p \mathbf{D}' + \epsilon \nabla^2 \boldsymbol{\sigma}' \tag{3.2}$$

The term $\overset{\square}{\boldsymbol{\sigma}'}$ appearing in Eq. (3.2) is as defined in section 2.2. η_p is the polymer viscosity, $\boldsymbol{\sigma}'$ is the viscoelastic stress tensor and T_o is the temperature at the initial time. The inclusion of stress diffusion in Eq. (3.2) determines the interfacial width between band layers which has been observed experimentally in the flow of wormlike micellars (see [75]) to have a length scale $l_d \approx O(10\mu m)$, l_d relates to ϵ by $l_d = \sqrt{\epsilon}$

and $\epsilon = \psi\lambda'$, where ψ is the diffusion term and λ' the stress relaxation time scale.

Using the following dimensionless variables and parameters

$$r = \frac{r'}{\zeta},\ z = \frac{z'}{\zeta},\ w = \frac{w'}{U},\ u = \frac{u'}{U},\ t = \frac{U}{\zeta}t',\ \boldsymbol{\sigma} = \frac{\zeta}{\eta_r U}\boldsymbol{\sigma}',\ P = \frac{R_o}{U\eta_r}P',$$

$$\theta = \frac{T' - T_o}{\alpha T_o},\ Q_D = \frac{\zeta^2}{\eta_r U^2}Q'_D,$$

$$Re = \frac{\rho U R_o}{\eta_r},\ Pr\ =\ \frac{c_p\eta_r}{\kappa},\ Br = \frac{\eta_r U^2}{\alpha\kappa T_o},\ Wi = \frac{\lambda_r U}{R_o},\ \alpha = \frac{RT_o}{E},\ \varepsilon = \frac{\phi\lambda_r}{R_o^2} = \frac{\epsilon}{R_o^2},$$

$$\delta_1 = \frac{R_o^2 QACE}{RT_o^2\kappa}\exp(-\frac{1}{\alpha}).$$

With this choice of dimensionless variable, we are able to incorporate the dimensionless gap scaling parameter χ into the equations of state, so that Eqs. (2.1), (2.2), (2.3) and (3.2) in non-dimensional form becomes (see appendix A.8, A.9 and A.10 for details of formulations):

$$\nabla.\ \boldsymbol{v} = 0, \tag{3.3}$$

$$Re\left(\frac{\partial \boldsymbol{v}}{\partial t} + \boldsymbol{v}\cdot\nabla\boldsymbol{v}\right) = -\nabla P(r,z) + \chi\nabla\cdot\boldsymbol{T}, \tag{3.4}$$

where $\boldsymbol{T}$ is as defined in Eq. (2.4)

$$PrRe\left(\frac{\partial\theta}{\partial t} + u\frac{\partial\theta}{\partial r}\right) = \frac{\chi}{r}\left[\frac{\partial}{\partial r}(\frac{r\partial\theta}{\partial r}) + rBrQ_D\right] + \frac{1}{\chi}\delta_1\exp\left(\frac{\theta}{\alpha\theta+1}\right). \tag{3.5}$$

and

$$\frac{1}{\chi^2}\boldsymbol{\sigma} + \frac{1}{\chi}Wi\lambda(\theta)\left[\overset{\square}{\boldsymbol{\sigma}} - \boldsymbol{\sigma}\frac{\alpha}{(1+\alpha\theta)}\left(\frac{\partial\theta}{\partial t} + u\frac{\partial\theta}{\partial r}\right)\right] = \frac{1}{\chi^2}\beta\mu(\theta)\mathbf{D} + \lambda(\theta)\varepsilon\nabla^2\boldsymbol{\sigma}, \tag{3.6}$$

respectively. Here, δ_1 and Wi represents the Frank Kamanetskii parameter and Weissenberg number respectively, while Re, Pr, Br, α and U are as defined in section 2.2 . The dimensionless viscosities and relaxation times also transforms to

$$\mu(\theta) = \exp(-\alpha\theta), \qquad \text{and} \qquad \lambda(\theta) = \frac{1}{1+\alpha\theta}\exp(-\alpha\theta).$$

The flow pressure takes the form,

$$P(r,z) = \begin{cases} -Gz + p(r) & \text{if} \quad \chi > 1 \quad \text{(which corresponds to axial annular flow)}, \\ \\ -Gz & \text{if} \quad \chi = 1, \quad \text{(which corresponds to a pipe flow)}, \end{cases}$$

and the dissipation term in dimensionless form, reflecting the contribution of geometric change (see appendix A.11 for details), translate to

$$Q_D = \mu(\theta)(1-\beta)\mathbf{D} : \nabla \boldsymbol{v} + \gamma\boldsymbol{\sigma} : \mathbf{D} + (1-\gamma)\frac{\hat{G}}{2\chi(1-\xi)Wi\lambda(\theta)}(I_1 + tr(\mathbf{b}^{-1}) - 6), \quad (3.7)$$

where I_1, γ and $\mathbf{b}$ are as defined in section 2.2.

The non-dimensional momentum equations in component form, which accommodate geometric change as a result of variation in value of χ, become (details are presented in appendix A.9).

Radial component of momentum

$$\frac{\partial p}{\partial r} = Re\frac{u^2}{r} + \chi\left\{\frac{\partial \sigma_{rr}}{\partial r} + \frac{\sigma_{rr} - \sigma_{\phi\phi}}{r} - \frac{2u}{r}(1-\beta)\frac{\partial \mu(\theta)}{\partial r}\right\}, \quad (3.8)$$

where u $(= b/r)$. Although the radial pressure is important in some industrial application such as wire coating, but our main focus in this work is on the distribution of the flow velocity, temperature and stresses, within the flow setup.

Axial Component of momentum

$$\begin{aligned} Re\left(\frac{\partial w}{\partial t}+u\frac{\partial w}{\partial r}\right) &= G+\chi(1-\beta)\mu(\theta)\frac{\partial^2 w}{\partial r^2} \\ &+\chi(1-\beta)\left(\frac{\mu(\theta)}{r}+\frac{\partial\mu(\theta)}{\partial r}\right)\frac{\partial w}{\partial r} \\ &+\chi\left(\frac{\partial\sigma_{rz}}{\partial r}+\frac{\sigma_{rz}}{r}\right), \end{aligned} \tag{3.9}$$

where, w is the axial velocity component.

Furthermore, the dimensionless stress constitutive relations in component form are obtained (see formulation details in appendix A.10) as:

rr Component of the stress tensor

$$\begin{aligned} \Phi\left(\frac{\partial\sigma_{rr}}{\partial t}+u\frac{\partial\sigma_{rr}}{\partial r}\right) &= \varepsilon\lambda(\theta)\frac{\partial^2\sigma_{rr}}{\partial r^2}+\frac{\varepsilon\lambda(\theta)}{r}\frac{\partial\sigma_{rr}}{\partial r} \\ &+\left(\Phi\mathbf{D}_{(\theta)}-\frac{1}{\chi^2}-(1-\xi)\Phi\frac{2u}{r}-\frac{2\varepsilon\lambda(\theta)}{r^2}\right)\sigma_{rr} \\ &+\left(\frac{2\varepsilon\lambda(\theta)}{r^2}\sigma_{\phi\phi}-(\xi-2)\Phi\sigma_{rz}\frac{\partial w}{\partial r}-\frac{\beta\mu(\theta)u}{r\chi^2}\right), \end{aligned} \tag{3.10}$$

rz Component of the stress tensor

$$\begin{aligned} \Phi\left(\frac{\partial\sigma_{rz}}{\partial t}+u\frac{\partial\sigma_{rz}}{\partial r}\right) &= \varepsilon\lambda(\theta)\frac{\partial^2\sigma_{rz}}{\partial r^2}+\frac{\varepsilon\lambda(\theta)}{r}\frac{\partial\sigma_{rz}}{\partial r} \\ &+\left(\Phi\mathbf{D}_{(\theta)}-\frac{1}{\chi^2}-(1-\xi)\Phi\frac{u}{r}-\frac{\varepsilon\lambda(\theta)}{r^2}\right)\sigma_{rz} \\ &+\left(\frac{\beta\mu(\theta)}{\chi^2}-\Phi\left[(\frac{\xi}{2}-1)\sigma_{zz}+\frac{\xi}{2}\sigma_{rr}\right]\right)\frac{\partial w}{\partial r}, \end{aligned} \tag{3.11}$$

$\phi\phi$ Component of the stress tensor

$$\begin{aligned}\Phi\left(\frac{\partial\sigma_{\phi\phi}}{\partial t}+u\frac{\partial\sigma_{\phi\phi}}{\partial r}\right) &= \varepsilon\lambda(\theta)\frac{\partial^2\sigma_{\phi\phi}}{\partial r^2}+\frac{\varepsilon\lambda(\theta)}{r}\frac{\partial\sigma_{\phi\phi}}{\partial r}\\ &\quad+\left(\Phi\mathbf{D}_{(\theta)}-\frac{1}{\chi^2}-(\xi-1)\Phi\frac{2u}{r}-\frac{2\varepsilon\lambda(\theta)}{r^2}\right)\sigma_{\phi\phi}\\ &\quad+\left(\frac{2\varepsilon\lambda(\theta)}{r^2}\sigma_{rr}+\frac{\beta\mu(\theta)u}{r\chi^2}\right), \qquad (3.12)\end{aligned}$$

zz Component of the stress tensor

$$\begin{aligned}\Phi\left(\frac{\partial\sigma_{zz}}{\partial t}+u\frac{\partial\sigma_{zz}}{\partial r}\right) &= \varepsilon\lambda(\theta)\frac{\partial^2\sigma_{zz}}{\partial r^2}+\frac{\varepsilon\lambda(\theta)}{r}\frac{\partial\sigma_{rz}}{\partial r}\\ &\quad+\left(\Phi\mathbf{D}_{(\theta)}-\frac{1}{\chi^2}\right)\sigma_{zz}-\xi\Phi\sigma_{rz}\frac{\partial w}{\partial r}, \qquad (3.13)\end{aligned}$$

where

$$\mathbf{D}_{(\theta)}=\frac{\alpha}{(1+\alpha\theta)}\left(\frac{\partial\theta}{\partial t}+u\frac{\partial\theta}{\partial r}\right),\quad \Phi=\frac{Wi\lambda(\theta)}{\chi}. \qquad (3.14)$$

3.2.1 Initial and Boundary conditions

We shall consider two geometric conditions. In case 1, we set $\chi = 1$ in the equations of state, so that the boundary conditions corresponds to a pipe flow problem, while in case 2, $\chi > 1$; thus, corresponding to the boundary conditions for the axial annular flow, so that as $\chi \to \infty$, then $R_i \to R_o$, i.e. $\zeta << 1$.

We also adopt the dynamic slip model similar to that in [48], so that in dimensionless form, see appendix A.12, it takes the form

$$w_s+\chi\alpha_1 Wi\lambda(\theta)\frac{dw_s}{dt}=\chi^m\alpha_2(\beta\mu(\theta))\sigma_{rz_w}{}^m, \qquad (3.15)$$

where $\alpha_1, \alpha_2, m \in \{2,4,6\}$ and σ_{rz_w} are as defined in case 2 of section 2.3.

Case 1: Pipe flow

In this case, we in particular consider $b = 0$ in the velocity field which corresponds to the absence of fluid suction/injection through the walls of the pipe. Here, the axisymmetric flow has a velocity field of the form $\boldsymbol{v} = (0, 0, w(r,t))$, and the temperature and stress fields are assumed to satisfy $\theta = \theta(r,t)$ and $\boldsymbol{\sigma} = \boldsymbol{\sigma}(r,t)$.

We solve Eq. (3.9) subject to the conditions

$$\begin{gathered} w(r,0) = 0, \qquad (t \leq 0), \\ \frac{\partial w}{\partial r}(0,t) = 0 \quad \text{and} \quad w(1,t) = w_s, \qquad (t > 0), \end{gathered} \tag{3.16}$$

The initial and boundary conditions for the temperature field in Eq. (3.5) are,

$$\begin{gathered} \theta(r,0) = 0, \qquad (t \leq 0), \\ \frac{\partial \theta}{\partial r}(0,t) = 0 \text{ and } \theta(1,t) = \theta_w, \qquad (t > 0). \end{gathered} \tag{3.17}$$

The stress equations are solved subject to the initial and boundary conditions:

$$\begin{gathered} \sigma_{ij}(r,t) = 0, \qquad (t \leq 0), \\ \frac{\partial \sigma_{ij}}{\partial r}(1,t) = 0 \quad \text{and} \quad \sigma_{ij}(0,t) = 0 \qquad (t > 0), \\ i, j \in \{r, \phi, z\}. \end{gathered} \tag{3.18}$$

Case 2: Annular flow with and without fluid injection/suction

In this case, we solve the governing equations for the annular flow problem i.e for $b = 0$ and $b \neq 0$ which yields convection-diffusion equations for the setup, subject to the following boundary conditions (see appendix A.15 for the reconstruction of the boundary nodes in terms of χ). For the momentum equation,

$$\begin{gathered} w(r,0)=0, \qquad (t\leq 0), \\ w(\chi-1,t)=w_s \quad \text{and} \quad w(\chi,t)=w_s, \qquad (t>0) \end{gathered} \tag{3.19}$$

for the energy equation,

$$\begin{gathered} \theta(r,0)=0, \qquad (t\leq 0), \\ \theta(\chi-1,t)=\theta_w \;\; \text{and} \; \theta(\chi,t)=\theta_w, \qquad (t>0). \end{gathered} \tag{3.20}$$

and for the stresses,

$$\begin{gathered} \sigma_{ij}(r,t)=0, \qquad (t\leq 0), \\ \frac{\partial\sigma_{ij}}{\partial r}(\chi-1,t)=0 \text{ and } \frac{\partial\sigma_{ij}}{\partial r}(\chi,t)=0 \qquad (t>0). \end{gathered} \tag{3.21}$$

In both instances, $\theta_w=\theta_0+\theta_{fr}$ where $\theta_{fr}=\varsigma|\sigma_{rz_w}|$ is the wall temperature resulting from frictional heating at the wall and $|\sigma_{rz_w}|$ is the magnitude of the wall shear stress as in chapter 2.

3.3 Results and discussion

3.3.1 Pipe flow without injection

Following the approach in chapter 2 we adopt semi-implicit finite difference techniques (see appendix A.13) for the solution process to the coupled system of equations governing the flow setup. Our numerical investigations are carried out under shear banding conditions. Unless stated otherwise, we have used the following parameter values: $Re=1,\; G=1,\; \gamma=0,\; \theta_0=0,\; \xi=0.8,\; \beta=0.95,\; \hat{G}=10^{-3},\; \delta_1=0.8,\; \alpha=$

$0.1,\ Br = 1,\ Pr = 1,\ \Delta r = 0.01,\ \Delta t = 0.005,\ t = 180,\ \varsigma = 0.8,\ k^* = 0.001,\ \alpha_1 = 0.5,\ m = 2.$

3.3.2 Numerical experiments for the pipe flow problem

Steady state profiles

We show convergence to steady state solutions for the velocity and shear stress - shear rate curves in Figs. 3.3 - 3.4, under (a) isothermal, no slip and no stress diffusion conditions and (b) non-isothermal, wall slip and non-zero diffusion parameter at various time steps. Fig. 3.5 shows convergence to steady state solution of temperature. In the absence of stress diffusion, the steady state solutions of the shear stress - shear rate curve are non-monotonic, see Fig. 3.4(a), which corresponds to the solutions for the Johnson Segalman (JS) constitutive model. However, the effect of stress diffusion in our numerical solution, Fig. 3.4(b), shows stress plateaus in the

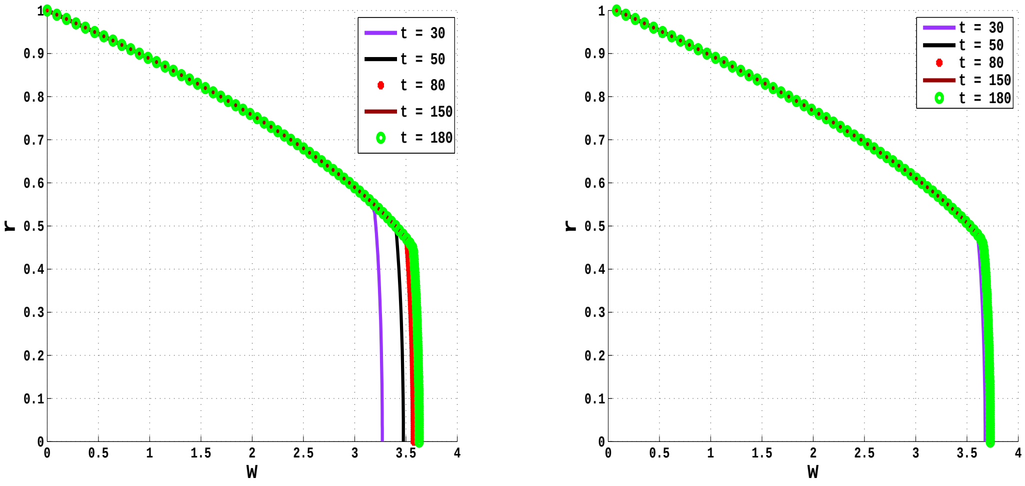

(a) (b)

Figure 3.3: Development of steady velocity profiles under (a) isothermal and no slip condition with $\varepsilon = 0$ and (b) non-isothermal and wall slip conditions with $\varepsilon = 0.0002$.

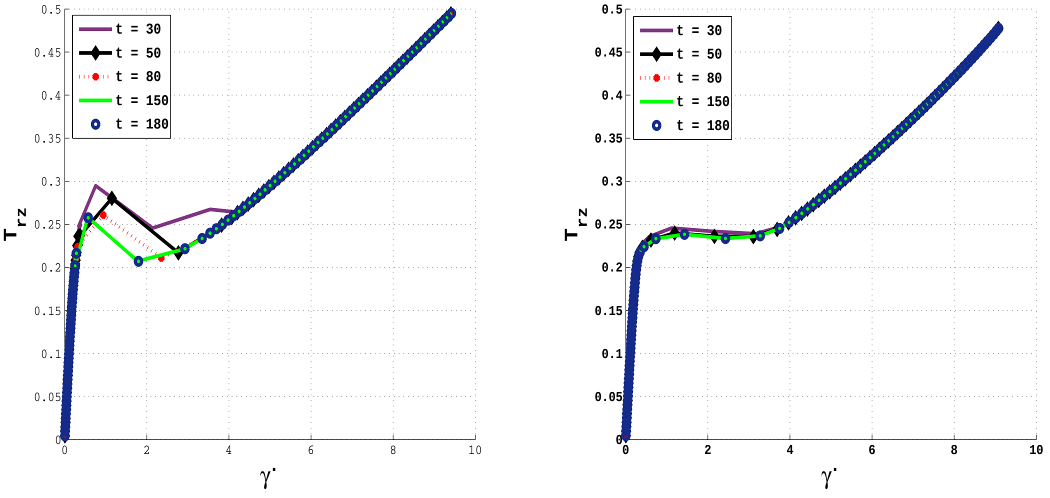

(a) (b)

Figure 3.4: Development of steady state shear stress - rate of shear curve under (a) isothermal and no slip condition with $\varepsilon = 0$ and (b) non-isothermal and wall slip conditions with $\varepsilon = 0.0002$.

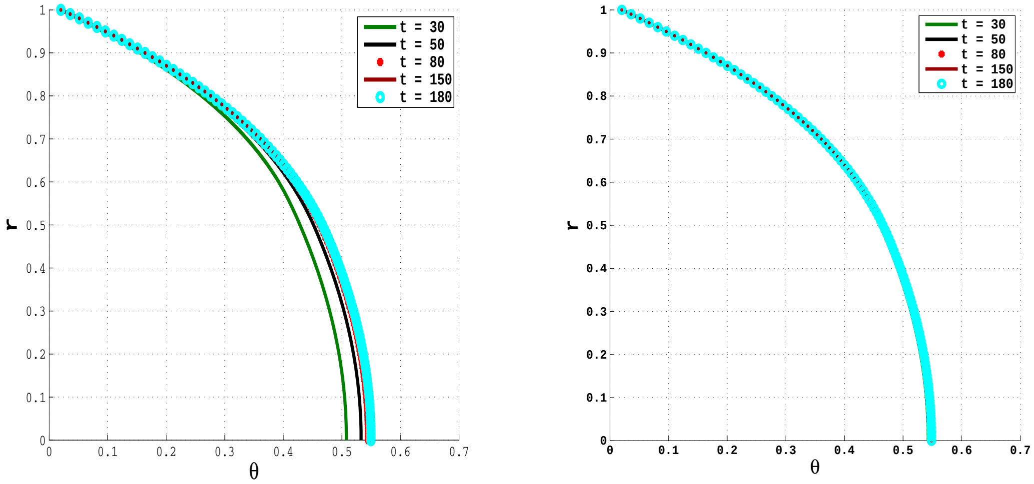

(a) (b)

Figure 3.5: Build up of steady non-isothermal temperature profile under (a) no slip condition with $\varepsilon = 0$ and (b) wall slip condition with $\varepsilon = 0.0002$.

constitutive curves. This indicates the selection of a unique stress path, as observed in the optical and rheological experiments performed on a viscoelastic solution in

[4], as well as recent experimental observations of Olmsted on worm-like micellar solutions, see [75] and those of Yamamoto, [117]. This result also shows agreement with theoretical results of [72] where diffusion terms were introduced into the stress constitutive equations of the JS model, resulting in the DJS model.

Non-isothermal effects

Of particular interest in this work is the stress selection phenomenon which has been reported in isothermal flow of fluids modeled by the DJS model in the absence of wall slip. Results from our numerical simulations under wall slip and non-isothermal condition, reveals that (see Fig. 3.6) the fluid temperature influences the value of the selected shear stress and thus also the onset of shear banding. In Fig. 3.6(a), if only heat generation as a result of entropic effects are considered i.e. without exothermic reactions, $\delta_1 = 0$, we observe that an increase in value of the Brinkman number results in a corresponding increase in the selected shear stress value T^*_{rz}, this is also the case for $\delta_1 \neq 0$ and $Br = 0$, see Fig. 3.6(b), this case corresponds to a purely exothermic heat generating flow setup such as reactive polymer foams; as normally seen in chemically blown polyurethane foams.

Fardin in his experimental work, see [36], showed that increasing or decreasing the temperature of the flow setup, affects the stability of the high shear rate branch in a shear banded flow of wormlike micellars, hence, in Fig. 3.7, by changing the temperature conditions from isothermal (i.e. $Pe = PrRe = Br = \delta_1 = 0$) to those corresponding to a non-isothermal system, where $Pe = PrRe = 1, Br \neq 0, \delta_1 \neq 0$, we observe a noticeable increase in the value of the selected stress, with the onset of banding setting in first, under isothermal condition. This observation may be attributed to the temperature dependence of both fluid viscosity and relaxation times.

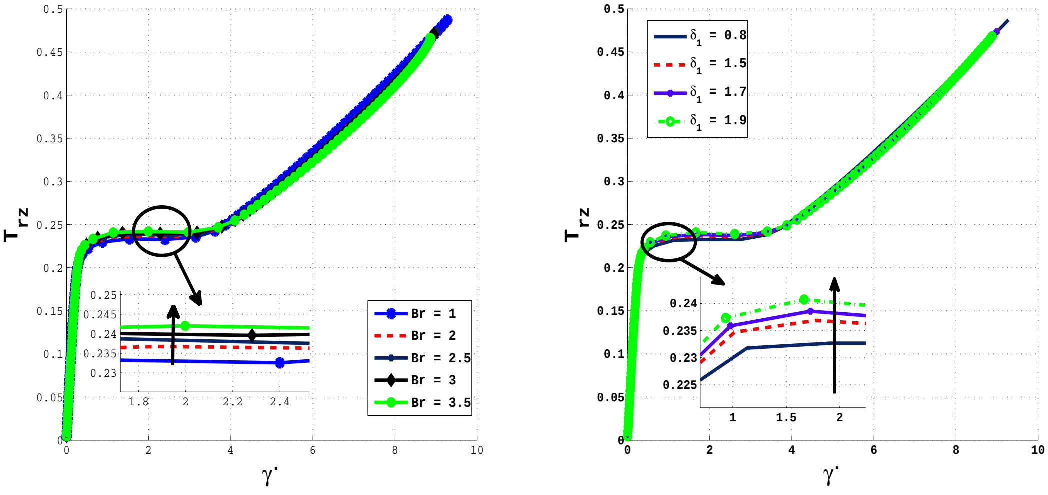

(a) (b)

Figure 3.6: Non-isothermal effect on the shear stress- shear rate curve for (a) $\delta = 0$ and various values of Br, (b) $Br = 0$, and various values of δ_1, for $\varepsilon = 0.0003$

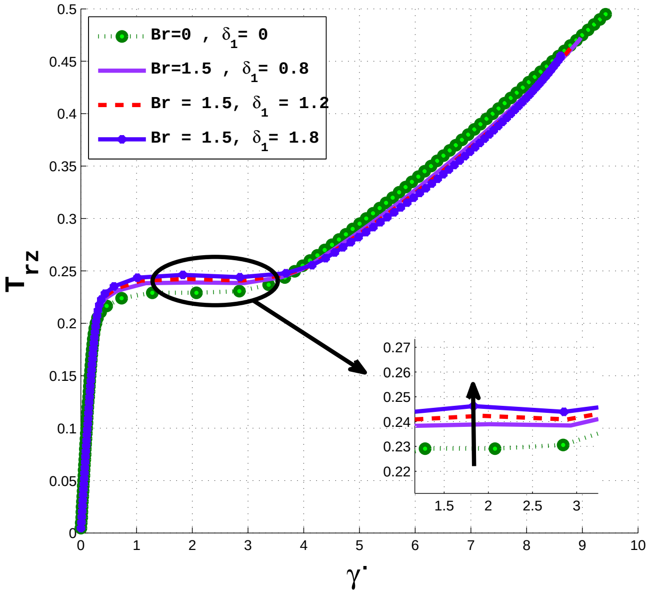

Figure 3.7: Temperature effect on stress selection phenomena in shear banded flow with polymer diffusion of $\varepsilon = 0.0003$.

Effects of stress diffusion on the flow profiles

Under shear banding conditions, the stress diffusion parameter ε (which relates to the non-zero inter facial layer), is observed to affect the on-set of shear banding as well as the flow profiles, see Fig. 3.8. In Fig. 3.8(a), thicker band layers (corresponding to higher ε values), reduce the selected stress (T^*_{rz}) value.

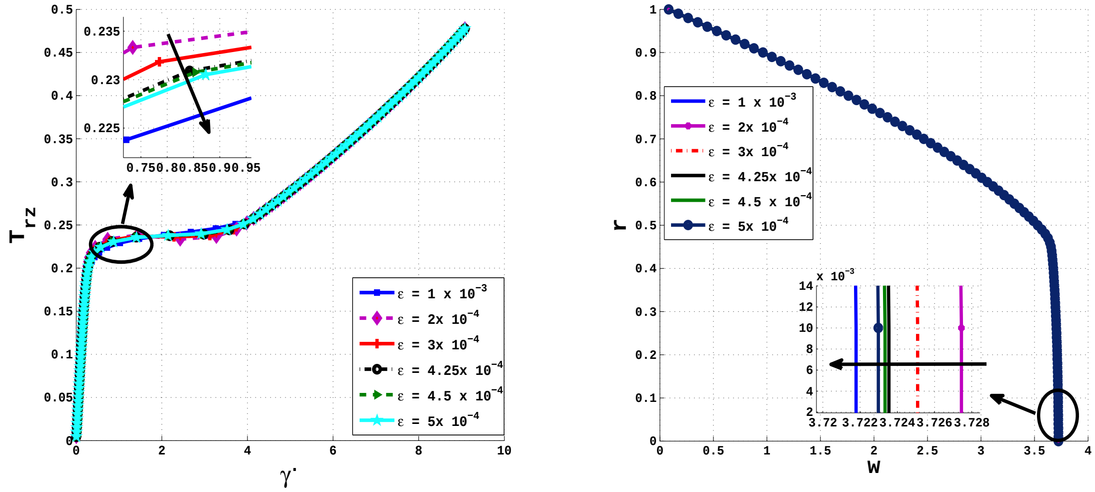

(a) (b)

Figure 3.8: Effect of polymer diffusion (a) on shear stress- shear rate curve, (b) on the flow velocity

This results in the onset of shear banding occurring at lower shear stress and hence, if the inter-facial layer is very thin, the T^*_{rz} value becomes relatively high. Similarly, the main flow velocity of the fluid is observed to be affected by the size of the band layer. The presence of a thick band layer within the flow setup, thus reduces the main flow velocity, see Fig. 3.8(b). These observations are in agreement with those discussed in [27, 28] and the experimental observations of [75] for worm-like micellar solutions.

Our results also show similar effects on the flow temperature profile Fig. 3.9. One may thus view the inter-facial layer as a thin heat resistant region within the flow, which

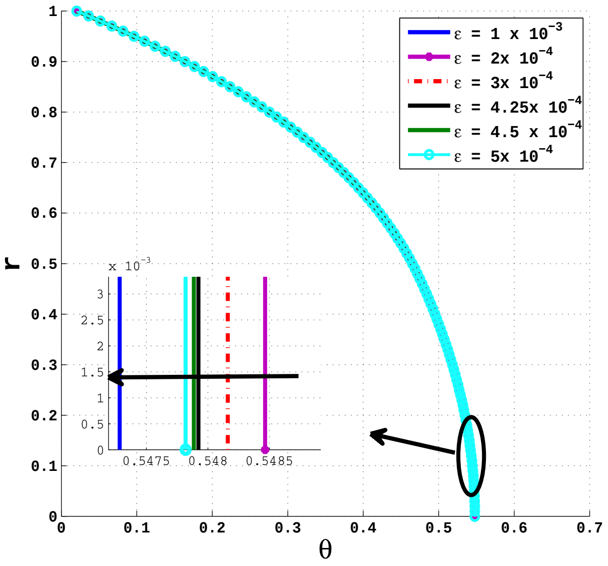

Figure 3.9: Temperature profile for various ε values.

restricts heat transfer across its thickness thereby affecting the overall temperature of the system. A thick band layer within the flow therefore corresponds to a relatively lower temperature within the bulk.

Effect of pressure gradient on the Flow

Since the flow in this study is purely pressure induced, an investigation on the effect of pressure on the flow curves Figs. 3.10, show the flow to move faster under higher pressure gradients. In Fig. 3.10(b), the contribution of wall slip on the bulk is evident, as the flow profiles consistently exhibit higher velocity, when compared to those in Fig. 3.10(a).

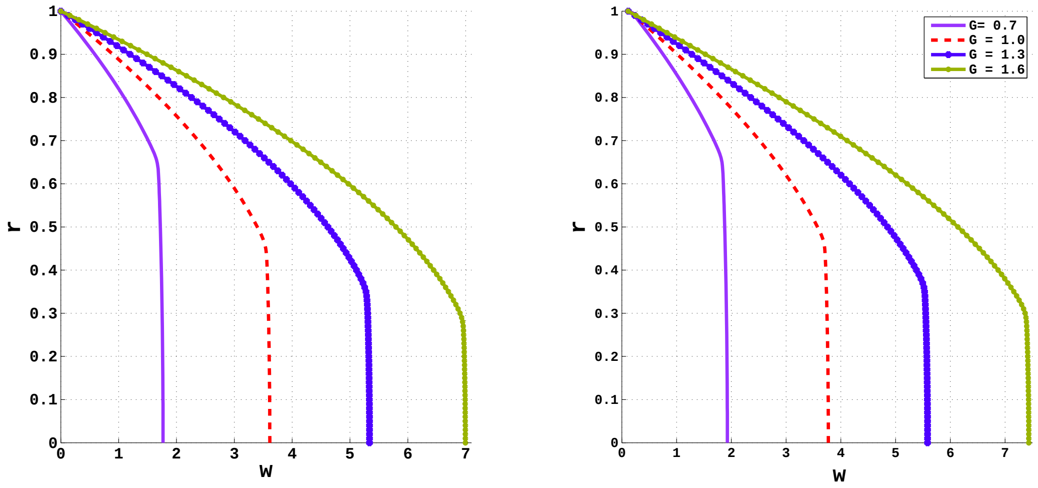

(a) (b)

Figure 3.10: Pressure effects on flow profile in the bulk, under (a) isothermal and no slip conditions, (b) non-isothermal and wall slip conditions

Effects of viscoelasticity on the shear stress - shear rate curves

As discussed in the experimental results of Fardin [36], the viscoelasticity of the fluid changes with an increase or decrease in material concentration of the polymer blend, thus, leading to fluid with higher/lower relaxation time, which relates directly to the Weissenberg number. In our current study, this change in viscoelasticity of the polymeric fluid was observed to affect the shear banding phenomena. In Fig. 3.11, as expected, the Weissenberg number “Wi” (which describes the degree of anisotropy or polymer orientation generated by material deformation), is shown to also affect the on-set of shear banding in the flow set up. In particular if the fluid considered is more viscoelastic, we see that an increase in Wi values reduces the value of the selected stress over a shorter range of apparent shear rates values $\dot{\gamma}_1 < \dot{\gamma} < \dot{\gamma}_2$. This implies that, increasing fluid viscoelasticity leads to a corresponding reduction in the critical stress value at which shear banding occurs in the flow, and therefore resulting

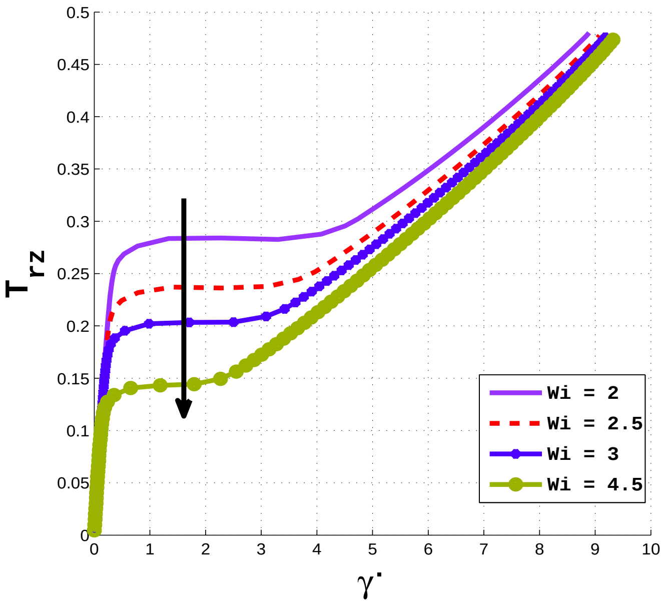

Figure 3.11: Shear stress - rate of shear curve for various Wi value with polymer diffusion of $\varepsilon = 0.0003$.

to shorter range for the unstable regime $\dot{\gamma}_1 < \dot{\gamma} < \dot{\gamma}_2$, before the fluid regularizes again i.e. $\dot{\gamma} > \dot{\gamma}_2$.

3.3.3 Axial annular flow problem

In this section, unless otherwise stated, we take $Wi = 3$ and $\delta_1 = 1$ whilst retaining other parameter values as in section 3.3.1.

Steady state flow profiles

For completeness, we show convergence to steady state solutions of our results for the annular flow problem. As in the pipe flow problem, we observe a plugged flow in the bulk for the velocity profiles, see Fig. 3.12 which corresponds to shear banded flow. In the presence of polymer stress diffusion, see Fig. 3.12(b), our results agree

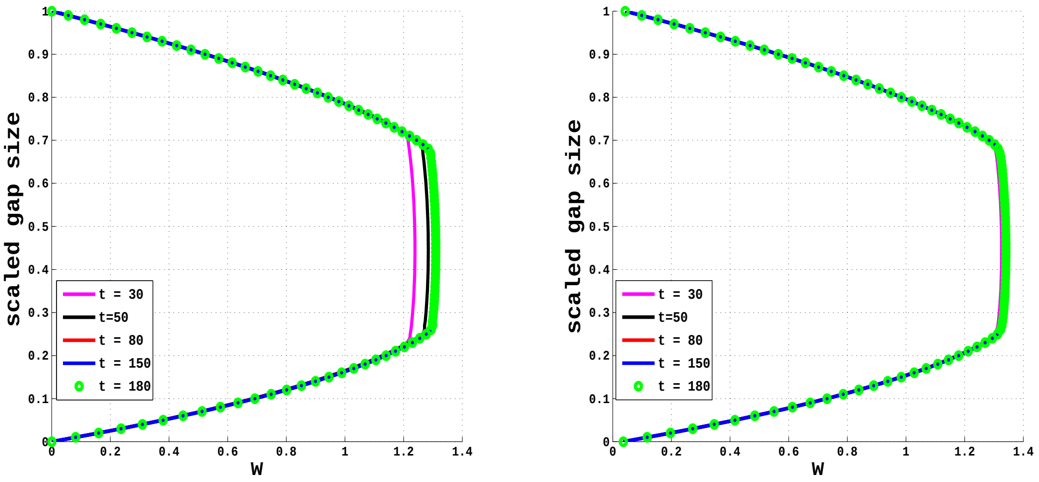

(a) (b)

Figure 3.12: Convergence to steady state velocity profiles under (a) isothermal and no slip condition with $\varepsilon = 0$ and (b) non-isothermal and wall slip conditions with $\varepsilon = 0.0001$.

qualitatively with experimental observations of [75], where it was shown that non-local (diffusive) terms play a role in the overall kinematic response in channel flow of worm-like micellar solutions. The results also show agreement with the flow profiles as discussed in [27, 28].

Effects of annular gap size on fluid velocity and on the shear stress - shear rate curves

The effect of annular gap size on the velocity profiles as well as the selected stress value is shown in Figs. 3.13 - 3.14. In both plots, as the gap becomes smaller, i.e. $\chi \to \infty$, the flow becomes more restricted, showing a plug like flow, which moves in, towards the center of the gap. Furthermore, we observe that under this constricted condition (for example $\chi = 10.5$ in the graph), the velocity profile (in the presence

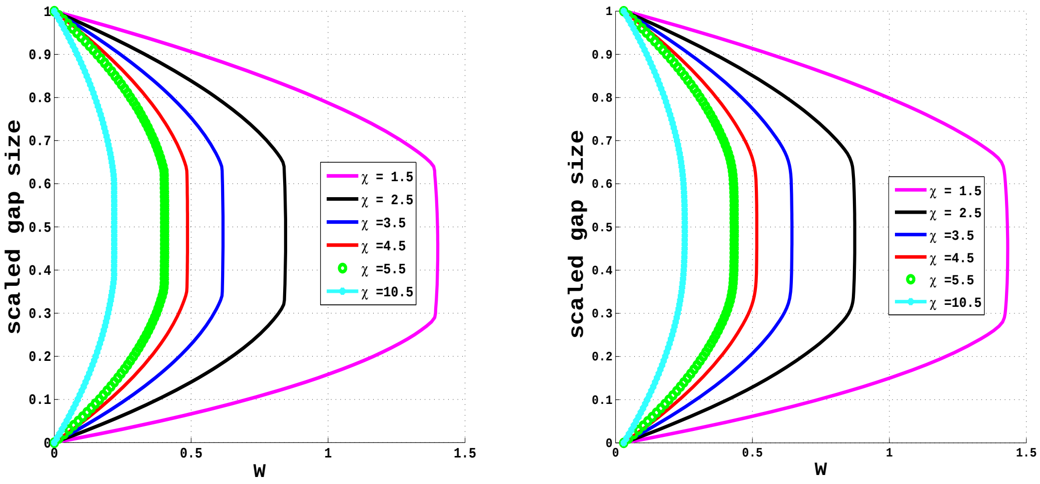

(a) (b)

Figure 3.13: Effect of gap size on the velocity profiles under (a) isothermal and no slip condition with $\varepsilon = 0$ and (b) non-isothermal and wall slip conditions with $\varepsilon = 0.0001$.

of polymer diffusion) becomes parabolic just like in the flow of Newtonian fluids, see Fig. 3.13(b).

In Fig. 3.14, the stress plateau becomes vanishingly small as $\chi \to \infty$, thereby resulting in an almost linear relationship between the shear stress and rate of shear. This result is consistent with the observations of [75] as well as the results of [28], where it was reported that in micro-rheological devices, unlike macroscopic ones, no unique interfacial plateau stress is observed. The plateau stress thus, decreases with decrease in channel width. We therefore conjecture that the onset of shear banding is affected by the gap size of the annulus, this may explain why the velocity profile at larger χ values, no longer appear plugged as seen in Fig. 3.13(b).

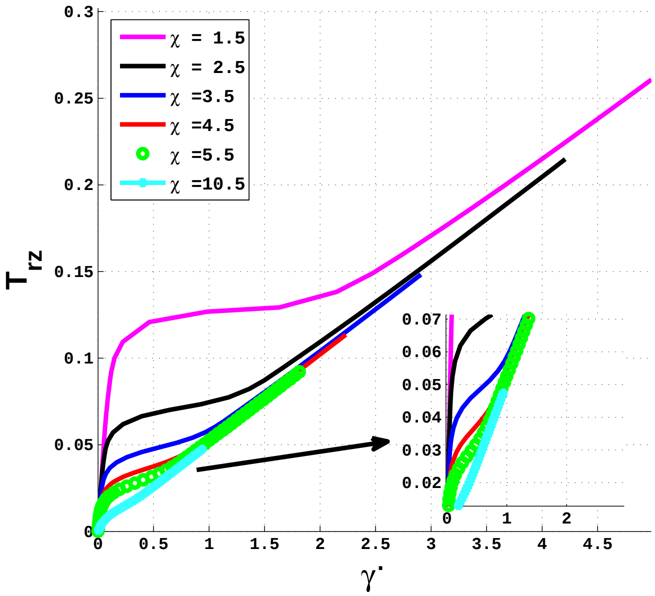

Figure 3.14: Annular gap size effect on stress plateau, under non-isothermal conditions and wall slip, with polymer diffusion of $\varepsilon = 0.0001$.

Injection/suction effects on the flow profiles and on the stress selection phenomena

We finally investigate the effects of fluid injection (through the walls of the inner pipe into the main flow) and suction (out of the outer walls) on the flow profiles. Fig. 3.15 shows the response of the flow when fluid is injected through the walls of the inner pipe and sucked out through the walls of the outer pipe. We observe that with increase in the value of the injection/suction parameter, the flow rate gradually reduces and additionally, as expected, the flow profiles shift in the direction of the injection flow. In Fig. 3.16, the selected stress for the onset of shear banding is also observed to be affected. We, in particular notice similar effects as observed when the gap size of the annulus is varied, thus the shear stress shear - rate curves becomes almost linear in this case as well.

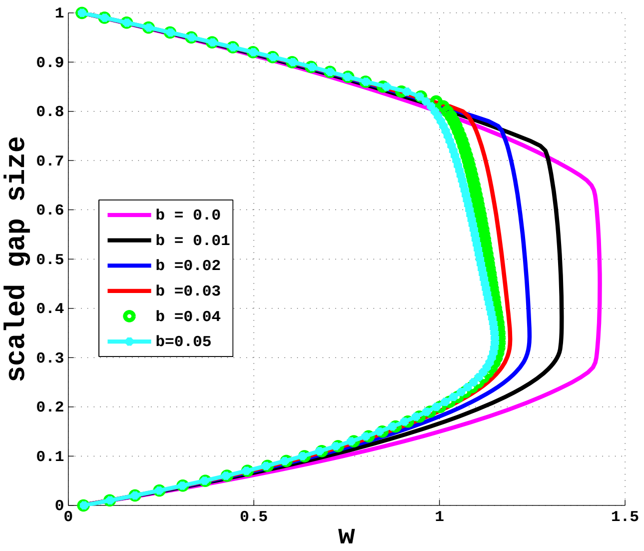

Figure 3.15: Plots showing effect of injection/suction on the flow velocity, under non-isothermal conditions and wall slip, with $\chi = 1.5$ and $\varepsilon = 0.0001$.

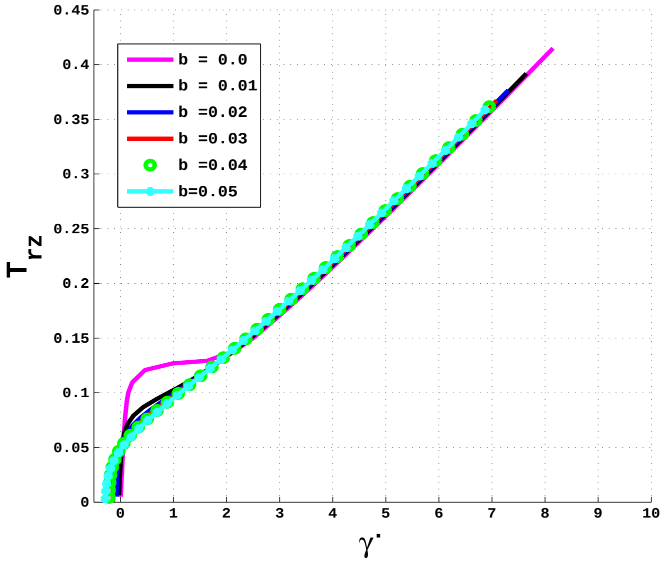

Figure 3.16: Effect of fluid injection on the shear stress - rate of shear curve, under non-isothermal conditions and wall slip, with polymer diffusion of $\varepsilon = 0.0001$. at $\chi = 1.5$

3.4 Conclusion

Using the stress diffusion type DJS model, we have numerically investigated the effect of temperature, stress diffusion, wall slip, injection and annular gap size on the related shear rate path selection phenomena which has been observed for polymeric fluids both theoretically and experimentally. Under conditions of shear banding, our results capture the unique shear stress path selection phenomena, in agreement with reported observations in the literature. This uniquely selected shear stress path is shown to be affected by fluid viscoelasticity, wall slip and heat transfer processes which arises in the flow as a result of say, wall heating, chemical reactions, inter-particle frictional heating within the fluid molecules or friction against the walls. The onset of shear banding is shown to be influenced by non-isothermal condition, so that as the temperature of the system increase, the selected stress value also increases, which leads to an increase in the critical stress value at which shear banding will normally occur. Investigations on the effect of the layer thickness, show that the flow temperature, bulk velocity as well as the value of the selected stress decreases as this band layer gets thicker.

As reported in literature, we observed that this stress selection phenomena is also affected by confinement. At narrower annular gaps, the flow regime becomes more restricted, showing a plugged flow in the bulk which consistently moves inwards towards the center of the gap, such that under very constricted condition (in the presence of polymer diffusion), the velocity profile becomes parabolic, while the shear stress - shear rate curve becomes almost linear. In the presence of transverse injection/suction flow, we observe that the shear banding phenomena is also affected. We, in particular observe reduced flow rates in the bulk flow. This injection is also shown to affect the shear stress - shear rate curves by making these monotonic.

Chapter 4

Complex Dynamics of Polyurethane Foam in Reaction Injection Molding*

Abstract

This chapter presents computational analysis of the complex dynamics observed in chemically blown Polyurethane (PU) foams during reaction injection molding process. The mathematical formulation introduces an experimentally motivated non-divergence free setup for the continuity equations which reflects the self expansion process observed in the physical system. The foam growth phenomena which is normally initiated by adequate pre-mixing of necessary reactant polymers, leading to an exothermic polymerization reaction, bubble nucleation and gas formation, is captured numerically. We assume the dependence of material viscosity on the cure/polymerization rate, gas volume fraction and non-isothermal temperatures as

---

*The contents of this chapter is from Ireka et. al. [58]

well as non-dependence of mixture density on pressure. The set of unsteady nonlinear coupled partial differential equations describing the dynamics of the system are solved numerically for state variables using finite volume techniques such that the front of the flow is tracked with high resolution interface capturing schemes. Graphical representation of the foam volume fraction, evolution of foam heights as well as temperature distributions are presented. Results from our simulations are validated with experimental data. These results show good quantitative agreement with observations from experiments.

4.1 Introduction

The chemistry of chemically blown Polyurethane (PU) foams has a well documented history, see [3, 34, 69, 107]; however, obtaining a proper mathematical description of the complex dynamics, which occurs in reaction injection molding (RIM), still remains an issue of current research. PU foams, rigid or flexible, possess certain physical attributes which makes them quite attractive for various industrial and domestic applications. For instance, rigid PU foams exhibit good thermal resistance properties, high energy absorption capacity, and their thermosetting nature makes them very useful in shock applications, acoustics and thermal insulations; with extensive application in aircraft, refrigerators, building, packaging and automotive industries as well as in structural materials under certain conditions. The properties of these foams depend strongly on the type of Isocyanate/Polyol group present in the reaction mixture and/or whether additional composite materials are introduced to the polymer blend [107].

In RIM, shear thinned reacting polymer mixture of adequate Isocyanate and Polyol group is injected into a mold where after a few seconds the material evolves from a low molecular weight emulsion (through polymerization with the evolution of heat and CO_2 gas) to a complex polymer network via chain-linking and polymer entanglement, known as chemical gelation or simply gelling [69, 101]. The gelling process occurs simultaneously with volume expansion, attributed to the diffusion of the resulting CO_2 gas into nucleated bubbles formed within the mixture. This process continues until a critical gel point (ζ_c), where transition from soluble liquid material to an insoluble solid matrix occurs [116]. Curing continues for several hours even after ζ_c is reached [69]. For theoretical and computational purposes, various cure models for thermosetting resins have been proposed and adopted (under certain conditions) in literature, see for example [18, 46, 64, 118]. For a detailed overview on chemorheology and cure kinetics modelling for thermosets, the reader is referred to the work of Halley and Mackay [46] and the references therein. Furthermore, a thorough review on factors affecting cure reactions, including formulation and process variables, can be found in [118]. The heat evolution during this exothermic reaction contributes to the overall curing process. This can be attributed to the fact that most of the reactants' material variables depend on temperature. In fact, a recent experimental study on temperature effects on the cure behavior for Polyurethane (solid and foams) reveal some interdependence between the degree of cure and non-isothermal temperatures [102]. Cure effects on the mixture viscosity are two fold, the viscosity is initially seen to decrease at the onset of the exothermic reaction process due to thermal effects and then subsequently increases as a result of the cross linking/gelation process [46]. To capture this phenomena, various viscosity models which assume the resin viscosity dependence on some combination of cure rate, shear rate, temperature, pressure, time, gas volume fraction and filler properties i.e. in the case of filled polymers, have been proposed [18, 31, 46, 98, 105].

The quest for optimally controlled molding processes has led to the formulation of various mathematical models capable of describing mass and heat transfer in reacting

PU setups; either from a mesoscale view [9, 10] or macroscale view [7, 15, 31, 70, 104, 105]. For instance, a two dimensional mathematical model for the flow of a chemically reactive polymeric system under different time and geometric conditions was presented in [70], the resulting numerical solutions predicted the evolution of the macroscopic velocity, temperature, stresses and species concentration fields in the flow. Furthermore, by proposing empirical density and viscosity models for the bubble suspension in the homogeneous phase of the resin mixture, a theoretical three dimensional (3D) model (an extension of the work of Baser [7]) was derived and solved numerically to predict the flow field, distribution of foam density, thermal conductivity and the progression of the flow front in mold filling processes of PU foam [104]. In a related study [98], mathematical models suitable for predicting the self-expansion process of foams in a physically blown reactive polymer setup, contained in a closed complex geometry, was presented. Here, an empirical based time and temperature dependent density model was assumed to drive the flow in the setup. Validations of numerical results with experimental data revealed a good qualitative agreement, even though some physical intricacies were lost to the modelling. On the other hand, a mesoscale modelling approach proposed by Bikard et al [9, 10] models the foam growth phenomena by the expansion of gas bubbles within the polymer matrix with evolutionary rheological behavior. In [9], the initial polymer mixture was assumed to be a diphasic compressible fluid (i.e. quasi-homogeneous liquid/gas mixture), so that the foam expansion process occurs as a result of evolution of gas rate in the mixture. This gas evolution was reported to result from a pressure difference between the liquid and gas, as well as CO_2 creation within the mixture.

We present a novel experimentally motivated mathematical model capable of predicting the complex dynamics exhibited by the reacting isocyanate - polyol mixture in the production process of PU foams. The experimental setup consists of a premixed mixture of reactants in a homogeneous phase, injected into a calibrated tube of known volume. The material is then allowed to expand and rise in the tube, while the expansion volumes are recorded as a function of time. We assume a non-isothermal viscosity model which depends on temperature, cure rate and gas volume fraction as well as the dependence of thermal conductivity and heat capacity (of the mixture) on the gas volume fraction. Furthermore, we adopt a Kamal type reaction model [64], for the foam curing process. The emerging set of coupled partial differential equations governing the dynamics of the system are solved via finite volume techniques, while the front of the expanding liquid foam is tracked with the aid of high resolution interface capturing schemes. Although there exists quite a number of mathematical models capable of predicting the expansion process in PU foams, our aim in this study is to propose a more tractable modelling approach which is capable of predicting the flow front, temperature distribution within the expanding system, as well as the observed front height both at the middle and at the wall of the tube, throughout the reaction process. Our proposed model is therefore ideally suited for possible use in various applications involving free rise of foams in either open or closed systems, including the case when the constituent reactants (i.e. Isocyanate, Polyol) are not known a-priori. Results from our simulations are validated with the experimental data[*]. Details of the experiment setup are presented in the next section.

4.2 Description of Experimental Setup

The characterisation of the PU foam propagation was carried out in laboratory experiments. To this end, a commercial rigid PU foam composition from Bayer Material Science (Leverkusen, Germany) was used. The processing of the two-component system to a PU reaction mixture was performed with a two-component

---

[*] Experimental details in this chapter are included with permission from our collaborators in TU Chemnitz, Germany, who provided us with the experiment data used to validate our model.

mixing and metering low pressure unit of Unipre GmbH (Werl, Germany). The basic components were preheated in the material containers to 30 ^oC, conveyed via a hose package to the mixing head, and metered there, at a ratio of 100:67 mass parts (isocyanate to polyol) in a static mixer, with an inner tube diameter of 8 mm. Transparent polycarbonate (PC) tubes were used for the foam propagation and consolidation and these tubes were aligned vertically in a clamping device. The tube inner diameter was 112 mm, the wall thickness 4 mm and the height 200 mm.The maximum propagation volume was thus designed to be approximately two liters. To determine the time-volume curves, scales were applied onto the tubes in a division of 0,025 l.

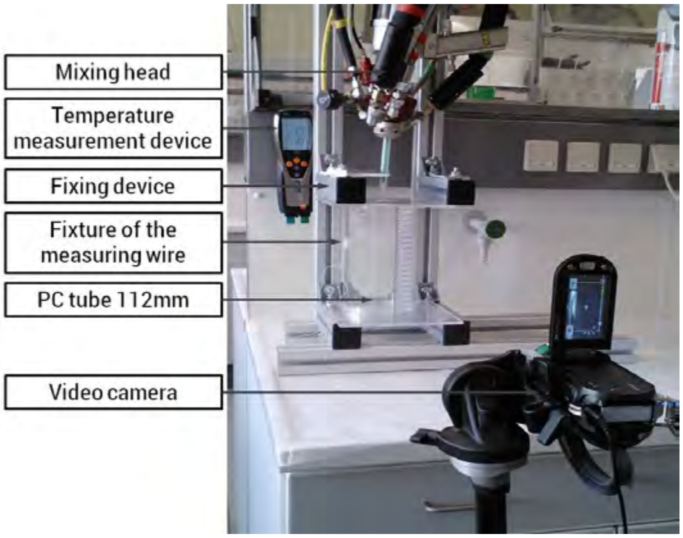

Figure 4.1: Experimental setup for determining the time dependent PU foam expansion

For discharging the reaction mixture into the PC tubes, the mixing head was suspended vertically above the tube opening so that the PU-mixture stream could flow onto the tube sheet without touching the tube walls (Fig. 4.1). For a plant and process engineering reproducible discharge, an output capacity of 150 g/min was used and various reaction masses were considered. For this study however, we focus on the 77 g reactant mass. All the experiments were carried out at room temperature. With a digital video camera, the PU expansion processes were observed and recorded; this aided the creation of the time-volume curves. The first impact of the mixture onto the tube sheet was defined as the temporal point of origin for the analysis. As soon as the expansion in volume sets in, each time of growth/expansion of the PU foam was recorded on a scale division. In the described manner, based on the parabolic flow front of the foam propagation, the curve progressions on the inner tube wall and the tube center were determined. To determine the reaction temperatures during the foam propagation, a measuring device Testo 735-2 of Testo AG (Lenzkirch, Germany) was used. The thermo-cables were inserted via lateral bores into the PC tubes and secured with cable ties, which impeded the foam propagation only slightly due to their small cross-section but still featured a sufficient bending stiffness to prevent displacement. Time-temperature curves were recorded for the examined reaction quantities at tube height of 1.25 l in the tube center. The measurement frequency was 1/s and the start of the measurement was again at the impact of the resin mixture onto the tube sheet.

4.3 Mathematical Modelling

To formulate a consistent mathematical model which describes the above mentioned setup, we consider a startup flow of self expansion of a reactive liquid polymer mixture contained in a 3D vertically oriented cylindrical tube of radius r and height H along the z axis. We assume the initial premixed reacting mixture to be incompressible and homogeneous, with nucleated bubbles distributed uniformly in the the emerging expanding foam. With these assumptions, we formulate a macro-scale mathematical model for the flow set up governed by the conservation equations of mass, momentum and energy, Eqs. (1.1 - 1.3), but this time, we include two additional equations describing the liquid volume fraction and the rate of polymerization within the reacting mixture. The continuity equation in this chapter is necessarily modified to accommodate the foam self-expansion process which essentially drives the flow.

Conservation of mass

Starting from the mass conservation equation,

$$\frac{\partial \rho}{\partial t} + \nabla \cdot (\rho \ \mathbf{v}) = 0, \tag{4.1}$$

we rearrange this to obtain,

$$\nabla \cdot \boldsymbol{v} = -\frac{1}{\rho}(\frac{\partial \rho}{\partial t} + \boldsymbol{v} \cdot \nabla \rho). \tag{4.2}$$

Recall that for incompressible fluids the RHS of Eq. (4.2) is zero. From the continuity equation, Eq. (4.2), unlike the modelling approach of [104] where an empirical model was developed for the foam density (ρ) and [98] where the density model was assumed to depend on temperature (thereby, making the right hand side of Eq. (4.2) non zero), we instead introduce a foam expansion term S_p, so that

$$\nabla \cdot \boldsymbol{v} = S_p. \tag{4.3}$$

We assume S_p to depend on volume changes in the expanding foam over time. This source term accounts for the foam rise, ensuring that the experimentally obtained height is adequately described by the results from simulations. Hence, S_p serves as an input to our simulations. We define S_p by

$$S_p = \frac{1}{V(t)} \frac{dV(t)}{dt}, \tag{4.4}$$

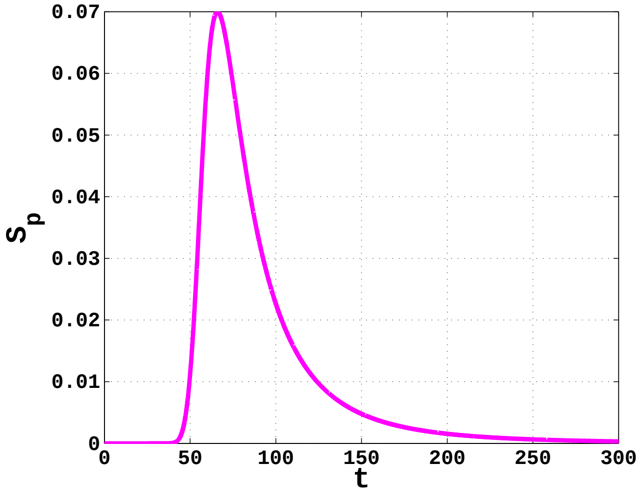

Figure 4.2: General behavior of expansion term S_p with time

here, $V(t)$ is a fit function corresponding to the measurements of the foam volume obtained over the duration of the expansion experiment, see section 4.4.2 for details.

The rate of change of $V(t)$ with time is reflected in the general behavior of S_p, see Fig. 4.2. We particularly observe that $S_p = 0$ at the initial time, which agrees with the incompressibility assumption we made for the initial homogeneous mixture. Furthermore, as the expansion progresses, S_p gradually increases until a maximum is reached and then decreases so that $S_p \to 0$ as $t \to \infty$ and the material becomes incompressible again (i.e. solidifies). This observation as shown by the decay in Fig. 4.2, guarantees that the expansion will stop at the end of our simulation.

Although our current investigation assumes a uniformly distributed source term S_p within the domain, this might not be optimum since the nucleated bubbles in the foam matrix may not necessarily expand in the same way, as the expansion of the bubbles is related to the difference between the bubble inner pressure and the liquid ambient pressure [16]. Therefore, in a physical system, each bubble inner pressure can vary, one from another. In future work, we intend to explore various means of capturing this obvious physical phenomena of non-uniform expansion across the reacting material.

Conservation of Momentum

The equation governing the motion of the system in conservative form is given by

$$\frac{\partial \rho \boldsymbol{v}}{\partial t} + \nabla \cdot (\rho \boldsymbol{v}\boldsymbol{v}) = \nabla \cdot \boldsymbol{\tau} - \nabla P + \rho \mathbf{g}. \tag{4.5}$$

Here, $\boldsymbol{v}$ is the velocity field describing the motion of the front under the influence of gravity, $\mathbf{g}$. P is the pressure within the system, $\boldsymbol{\tau}$ is the stress tensor and ρ is the density of the homogeneous mixture assumed to depend linearly on gas volume fraction φ_g.

$$\rho = \rho_l(1 - \varphi_g) + \rho_g \varphi_g, \tag{4.6}$$

where ρ_l and ρ_g are the liquid mixture and gas density respectively. $\varphi_g = 1 - \varphi$ and φ is the liquid volume fraction defined by

$$\frac{\partial \varphi}{\partial t} + \nabla \cdot (\varphi \boldsymbol{v}) = 0, \tag{4.7}$$

Expanding Eq. (4.7) and substituting Eq. (4.3), we have that φ is related to S_p by

$$\frac{\partial \varphi}{\partial t} + \boldsymbol{v} \cdot \nabla \varphi = -\varphi S_p, \tag{4.8}$$

Eq. (4.8) is necessary for tracking the front of the expanding foam.

Although, it would be appropriate to incorporate a viscoelastic tensor in the stress relations, since the expanding foam exhibits some traits of viscoelasticity at some stage, we will assume the stress tensor $\boldsymbol{\tau}$ to obey

$$\boldsymbol{\tau} = \eta_m \boldsymbol{D}, \tag{4.9}$$

where $\boldsymbol{D}$ is as defined in Eq. (1.12) and and η_m is the foam mixture viscosity. Observe in Eq. (4.9) that we have neglected the inclusion of bulk viscosity; this has been shown to generally decrease with foam expansion (see [98]), and since the expansion in the current study occurs rapidly, we therefore assume no contribution of the bulk viscosity to the stress equation.

We define the mixture viscosity by

$$\eta_m = \begin{cases} \eta_F, & \text{for} \quad \varphi \geq \varphi_s, \\ \\ \eta_F \frac{\varphi}{\varphi_s} + \eta_g \left(1 - \frac{\varphi}{\varphi_s}\right), & \text{for} \quad 0 \leq \varphi < \varphi_s. \end{cases} \tag{4.10}$$

here, φ_s is a constant switch fluid volume fraction (such that φ_s=0.01 signifies 99% volume fraction occupied by gas), which is introduced to define the interface between foam and the surrounding (air), η_g is the gas (air) viscosity. Following [9], the foam viscosity model is given by

$$\eta_F = \eta_{oo} \exp\left(\frac{E_\eta}{RT}\right) \cdot \left(\frac{\zeta_c}{\zeta_c - \zeta}\right)^{h(\zeta)} f(\varphi_g), \tag{4.11}$$

where η_{oo} is the mixture viscosity at initial temperature T_o and E_η is the activation energy for the polymer mixture. ζ_c represents the gelling point for the polymerization reaction, while ζ (defined by Eq. (4.18)) indicates the amount of uncured polymer in the mixture and $f(\varphi_g)$ is defined by (see [9]),

$$f(\varphi_g) = a_1 + a_2\varphi_g + a_3\varphi_g^2 \ \text{ and } \ h(\zeta) = b_1 + b_2\zeta, \tag{4.12}$$

where

$$a_1 = 0.8,\ a_2 = -1.2,\ a_3 = 0.5,\ b_1 = 1.5 \text{ and } b_2 = 1.$$

Conservation of Energy

Due to the high amount of heat generated as a result of exothermic reactions within the mixture, the equation governing the distribution of heat, Eq. (1.3), is modified so that the heat source as a result of the exothermic reactions dominate over other heat generating terms in the energy equation. To obtain the temperature distribution within the system, we therefore adopt the model of [98], so that the heat transfer processes are governed by,

$$\rho C_p \left(\frac{\partial T}{\partial t} + \boldsymbol{v} \cdot \nabla T \right) = \nabla \cdot (\kappa \nabla T) + \rho H_R \frac{\partial \zeta}{\partial t}, \tag{4.13}$$

where T is the temperature of the system, H_R (in J/Kg) is the heat generated as a result of chemical reaction, κ and C_p are the thermal conductivity and heat capacity respectively. H_R is defined as

$$H_R = H_r \Gamma, \tag{4.14}$$

where H_r is a constant, see Table:4.1, and Γ is chosen such that its magnitude is equivalent to the magnitude of C_p. Similar to the approach of [70], we assume C_p and κ to depend linearly on the gas volume fraction by

$$C_p = C_{p_l}(1 - \varphi_g) + C_{p_g}\varphi_g, \tag{4.15}$$

and

$$\kappa = \kappa_l(1-\varphi_g) + \kappa_g\varphi_g + \kappa_r. \tag{4.16}$$

The terms C_{p_l} and C_{p_g} correspond to the heat capacities of the continuous liquid phase and gas phase respectively, and similarly, κ_g and κ_l respectively represent the thermal conductivity of the gas and liquid phase. We further assume κ_g to depend linearly on temperature, so that

$$\kappa_g = 0.0271 + \tau^*(T - T_o), \qquad \tau^* = \frac{\kappa_g(T_{max}) - \kappa_g(T_o)}{T_{max} - T_o}. \tag{4.17}$$

Since the heat generation resulting from chemical reaction in the setup is high, with a maximum temperature (T_{max}) of about 160^oC, under a fast reacting system; we thus neglect contributions from the radiative thermal conductivity κ_r in Eq. (4.16). Adopting the Kamal cure model [64], Eq. (4.18) thus governs the amount of uncured polymer in the mixture.

$$\frac{\partial\zeta}{\partial t} + \boldsymbol{v}\cdot\nabla\zeta = (k_1 + k_2\zeta^m)(1-\zeta)^n, \tag{4.18}$$

where, m and n are constants and $k_j,\ j \in \{1,2\}$ are the rates of the primary polyol - isocyanate reaction and the secondary water-isocyanate reaction defined as

$$k_j = A_j \exp(-E_j/RT). \tag{4.19}$$

A_j and $E_j, j \in \{1,2\}$ are the Arrhenius pre-factor and activation energy respectively. Under isothermal conditions, Eq. (4.18) has shown good agreement for cure data of a variety of thermosetting systems [65]. However, the difficulty arises when the time change of temperature is considered (i.e under non-isothermal conditions); this dynamics of the temperature has been shown to have a strong affect on the cure rate [102]. Due to the challenges involved with incorporating non-isothermal effects (resulting from rapid heating) into the cure equations, we have chosen to obtain the values of the k_j's from numerical experimentation. We present details of this approach in section 4.4.3.

4.4 Numerical Method and estimation of input parameters

In this section, we present a description of the discretization technique utilized in this chapter as well as the approach used for the choice of some input parameters adopted in the equations governing the expansion and polymerization processes. Due to the high level of computation involved, all the 3D simulations carried out in this study are implemented in CoRheoS; a complex rheology simulation platform developed at the Fraunhofer ITWM, Kaiserslautern Germany.

4.4.1 Numerical Method for the State Equations

Each of the model equations described in section 4.3 is discretized with finite volume method on collocated grids, see [111]. Furthermore, we employ the Chorin algorithm discussed in [26], see appendix A.17 (and with successful implementation in [68, 85, 86] for non-Newtonian fluids), to resolve the conservation of mass and momentum equations Eqs. (4.3) and (4.5) respectively. This algorithm particularly aids us in decoupling pressure from the Navier-Stokes equations, thereby, splitting the continuity and momentum equations into individual equations for the velocities and pressure.

The viscosity functions in [68, 85, 86] are space dependent, hence, can differ within the spatial domain by some orders of magnitude in one computation time. The same applies to our current study wherein the fluid viscosity is seen to increase with decrease in temperature and increase in polymerization values as the gelling point is approached. Stable numerical simulations are thus satisfied by a full implicit discretization of the viscous term in Eq. (4.5) without necessarily decreasing the time steps, whilst the fluid viscosity increases. For details on the discretization approach used in this work, the reader is referred to [115] and the references therein. Furthermore, the corresponding convective terms in both Eqs. (4.5) and (4.13) are discretized with the upwind discretization approach. Although the upwind scheme is known to smear out solutions but with our choice of time step ($\Delta t = 2.5 \times 10^{-4}$) and mesh sizes of $O(10^{-3})$ in each direction, this smearing is minimized with a reasonable level of accuracy.

To solve the unsteady, coupled system of partial differential equations Eqs. (4.3), (4.5), (4.8), (4.13) and (4.18), along with the constitutive relations for gas volume expansion Eq. (4.4), fluid (foam) viscosity Eq. (4.11), heat capacity Eq. (4.15) and thermal conductivity Eq. (4.16); we first linearize the convective term in Eq. (4.5) with the Picard linearization technique (see appendix A.16 for illustration), and then solve the emerging equations of conservation of mass and momentum. Fluid viscosity relation Eq. (4.11) is updated with the values of temperature, polymerization and gas volume fraction obtained in the previous time step. Furthermore, the discrete solution of temperature, polymerization and fluid volume fraction are respectively obtained. Special care needs to be taken when obtaining the discrete form of the convective terms in Eqs. (4.8) and (4.18), since the flow front ought to be as sharp as possible. To satisfy this constraint, we adopt the high resolution interface capturing scheme (HRIC) of [84], which has been successfully implemented in the simulations of two phase flow of incompressible immiscible fluids, see [52, 84, 112] for example.

In our simulations, we assume no-slip velocity conditions at the walls and base of the tube, and then initialize the flow velocity to zero, so that the advancement of the front starts from rest. The volume fractions as well as the polymerization are also initialized to zero. Temperature values are set initially (T_o) to 25^oC, this corresponds to the room temperature under which the experiments were carried out. Special care is given to the temperature at the wall, as it is observed that the wall temperature also increases as the expansion progresses, hence, we prescribe a flux boundary condition defined by

$$\kappa \frac{dT}{dx_{int}} \cdot \mathbf{n} = \lambda_2 \frac{dT}{dx_{wall}} \cdot \mathbf{n} \tag{4.20}$$

on the walls of the tube. Here, κ represents the thermal conductivity of the reacting mixture contained in the tube and λ_2 is that of the tube (polycarbonate in this case) dx_{int} corresponds to an interior distance from the wall, while dx_{wall} is the tube thickness, and $\mathbf{n}$ is the normal vector. In section 4.5, we discuss with graphical illustrations the results obtained in our simulations and then validate them with experimental data.

4.4.2 Estimating fit function for Volume expansion over time

The expanded foam in Fig. 4.3(b), is estimated to compose of a cylindrical base with radius $r = 56 \times 10^{-3}m$ and height $H_w(t)$, and half of an ellipsoid with planar minor and major axis $a = r$, $b = r$ respectively, and height $h = H_m(t) - H_w(t)$, on the top of the cylinder, see Fig. 4.3(a). $H_m(t)$ and $H_w(t)$ are the time dependent heights at the middle and wall respectively. We therefore obtain an approximate equation for

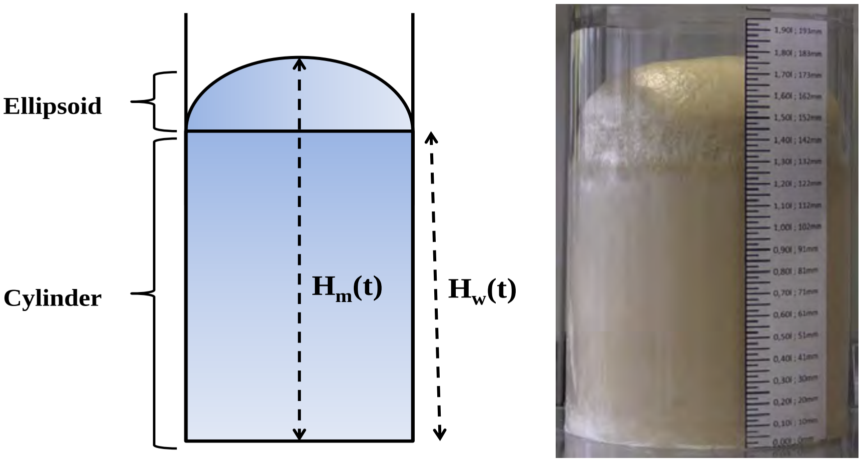

(a) (b)

Figure 4.3: (a) Estimate of the geometry of expanded foam, projected on a 2-D plane (b)Image of the expanded foam at the end of the foam expansion experiment

the volume expansion as a function of time in the form

$$V(t) = \pi r^2 H_w(t) + \frac{2}{3}\pi r^2 (H_m(t) - H_w(t)) \tag{4.21}$$

The height $H_w(t)$ and $H_m(t)$ are obtained by fitting function curves to the data obtained for the corresponding heights from experiment as shown in Fig. 4.4(a). Haven obtained the function curves $H_w(t)$ and $H_m(t)$ which approximates the data from experiment, we then compute the volume expansion $V(t)$ over time, see Fig. 4.4(b). The fit function $V(t)$ is in turn used to obtain the relevant expansion source term S_p in the continuity equation.

4.4.3 Estimating Polymerization parameters

To avert the difficulty introduced by non-isothermal conditions on the polymerization equation (as described earlier), we obtain numerical estimates for the values of the $k_j's$ in Eq. (4.19) and H_R in Eq. (4.13). Thus, from several 1D simulations of the coupled

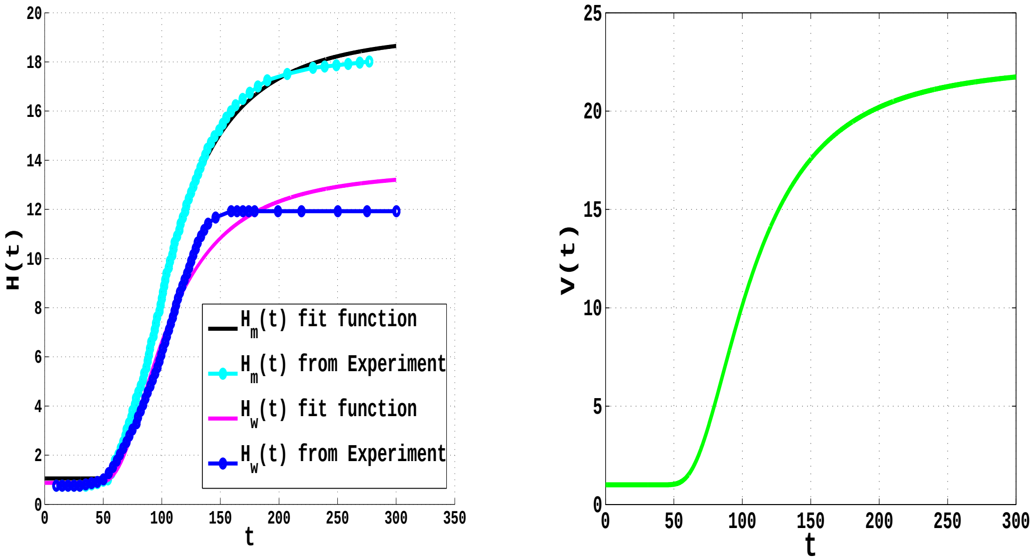

(a) (b)

Figure 4.4: Curves showing (a) foam height on the wall and at the center, (b) estimated function for the volume as a function of time

temperature and cure equations, we adopt optimal values of k_1, k_2, m, n and H_R for which the resulting temperature curves have good agreement with the given experimental data, see Fig.4.5. These estimates therefore serve as first approximations for the input parameters required in the 3D simulations of the flow setup. This idea seemed reasonable, particularly because it takes longer time to complete one run of numerical experimentation in 3D geometry, therefore, in order to have some idea of what happens in the higher dimensions, we explored the general behavior in 1D.

Furthermore, we also opted for this approach, since not much information concerning the constituent elements of the reacting materials (polyol-isocyanate groups) used in the experiment was available to us. Secondly, the experiments were not conducted under adiabatic conditions; which would have naturally aided us in computing the necessary rate parameters involved in the Arrhenius model of the k_j's. In future works, provided adequate information becomes available, we hope to be able to back

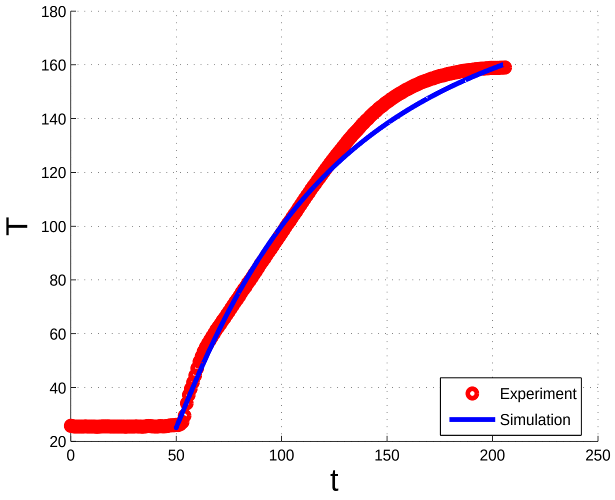

Figure 4.5: Comparison of temperature distribution over time from experiment and simulation, for the chosen values of k_1, k_2, m and n

couple the cure equation with temperature, by assuming an Arrhenius dependence of the k_j's on temperature.

4.5 Results and Discussion

P	Value	Source	P	Value	Source
C_{p_l}	2000J/KgK	[90]	κ_l	0.19 W/mK	[90]
C_{p_g}	1012J/KgK		η_{00}	1.08×10^{-7}Pa s	
ζ_c	0.65	[104]	E_η/R	4970 K^{-1}	[104]
n	1.5	Simulation	m	0.5	Simulation
k_1	$1.0553\times10^{-2}s^{-1}$	Simulation	k_2	$5.15164\times10^{-3}s^{-1}$	Simulation
H_r	135	Simulation	ρ_l	1100Kg/m^3	
ρ_g	1Kg/m^3		$\kappa_g(25^oC)$	0.0271W/mK	
λ_1	0.2 W/mK		$\kappa_g(160^oC)$	0.0358W/mK	

Table 4.1: Parameter values adopted for our simulations

In this section, we present 3D results from our numerical simulations with validations from experiments. The parameter values used throughout this study are presented in

Table: 4.1. The flow fronts are compared with those obtained from experiments, for the 77 g resin mixture in the tube. The initial height, from experiment, was adopted as input for our numerical simulation.

4.5.1 Spatio-temporal variations of Temperature

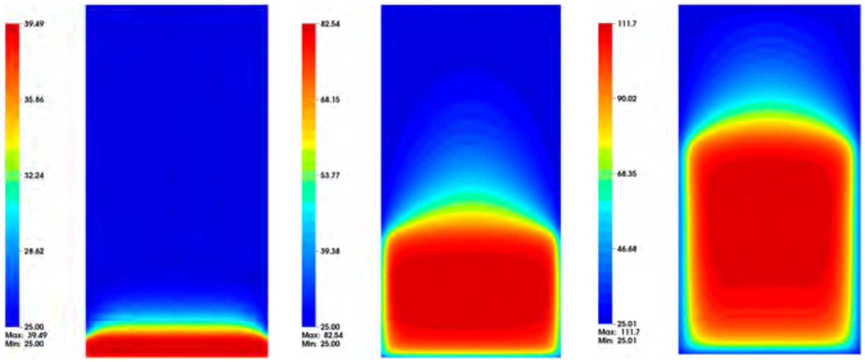

(a) t=60secs (b) t=110secs (c) t = 150secs

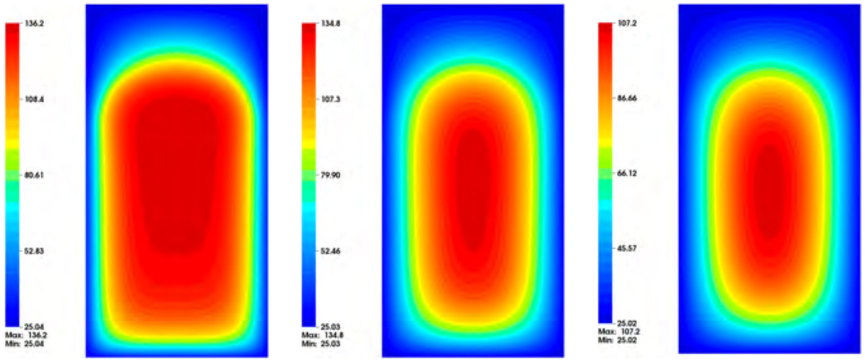

(d) t=250secs (e) t=580secs (f) t=900secs

Figure 4.6: 2D snap shots of the evolution of temperature and it's spatial distribution in the tube (slices along centerline)

Snapshots of 2D axial slices of our 3D simulations for the temperature distribution in the domain Figs. 4.6, reflects the spatial change of temperature over time. The rapid heat generated as a result of exothermic reactions within the polymer mix is convected along with the mixture, in the direction of flow.

Hence, the distribution of temperature is such that maximum heat is generated at the core of the setup i.e the deep - red regions in Figs. 4.6, with minimum temperatures observed at the walls of the tube. Furthermore, we observe that heat generation occurs mainly in the first 400 seconds of our simulations, Figs. 4.6(a-e), after which the reaction stops and the systems starts to cool down in an inward manner, Figs. 4.6(e-f). This heat loss is attributed to heat transfer by diffusion via the walls of the tube to the environment. With this form of temperature distribution in the domain, since the foam viscosity depends on temperature in a decreasing manner whilst growing infinitely as the gelling point is reached, the flow is thus expected to be maximum in regions with higher temperature corresponding to lower viscosity). This spatial variation of the fluid viscosity therefore initiates a fountain flow at the center of the tube, leading to the formation of the front curvature discussed in section 4.5.2.

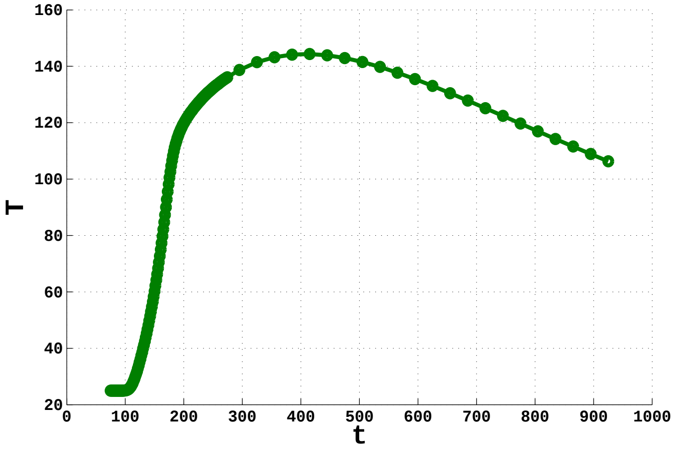

Figure 4.7: Time change of temperature at a point in the center of the tube, 1.25l from the base: result from simulations

The temporal temperature measurements, at a fixed point in the domain, from our simulations, Fig. 4.7, further buttress our observations in Figs. 4.6(a - f), we particularly observe a rapid increase in temperature followed by a gradual decay

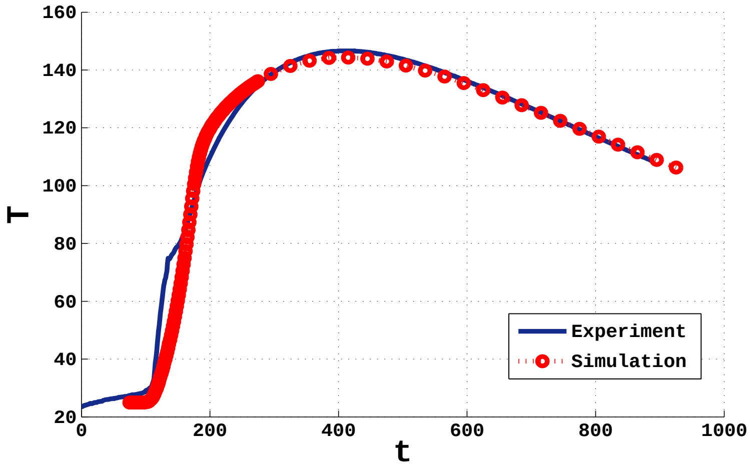

Figure 4.8: Temperature change over time at the height of 1.25l in the center of the tube: Comparison of results from experiment and simulation

after a maximum value had been reached. Since it will be very difficult to slice through the physical material while the experiment is in progress, time measurements of temperature at the same fixed point in the domain, as in the simulations, were obtained from experiments. The resulting measurements were compared with results from our simulation, see Fig. 4.8, our results compare favorably with that from experiment.

4.5.2 Volume expansion, Flow front curvature and Foam height (at the wall and middle)

To investigate the progression of the foam front as well as the curvature, we run our simulations over the duration of the foam expansion as observed in the experiment. This normally takes about 250 seconds, after which the height remains constant. We note that the actual expansion process starts at about 50 seconds after the reacting mixture is injected into the tube.

(a) t=150secs (b) t=200secs (c) t=250secs

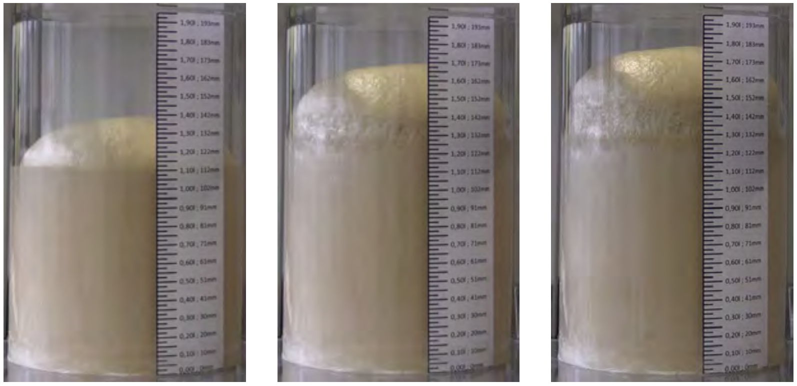

(d) t=150secs (e) t=200secs (f) t=250secs

Figure 4.9: Advancement of flow front of the foaming material mixture in the tube; above, results from simulations and below, those from experiments

In Figs. 4.9(a-c), 2D axial slices of results from our 3D simulations for the evolution of the expanding foam fractions (for 77 g of material) are presented. The emergence of the flow front curvature depends mostly on the fluid viscosity, which increases with decrease in temperature and increases infinitely with the advancement of the polymerization rate. As the gelling point is approached, and since the temperature at the walls is lower than those at the core, see Figs.4.6(a-d), the viscosity becomes very high at the walls, leading to a retarded fluid motion around the wall, so that as time evolves, the flow rates at the wall becomes very low and much higher at the middle. Therefore, when the mixture viscosity at the wall is not high enough, the

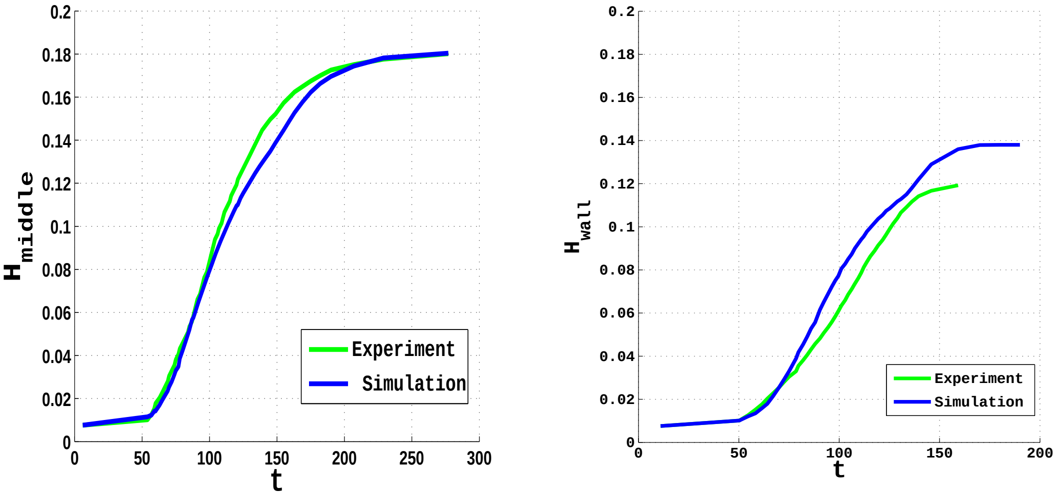

(a) (b)

Figure 4.10: Foam height from experiment with 77grams material compared with results from our simulation (a) at the middle of the tube H_m, (b) and at the wall of the tube H_w

flow front remains almost flat, Fig. 4.9(a), but as soon as the polymerization reaches the gelling point, the viscosity grows infinitely, thus, the curvature at the flow front emerges, Figs. 4.9(b - c). When compared with experiments, the curvature of the flow front from our simulations compare favorably well with those obtained in the experiment, see Figs.4.9 (a - f).

We note that, as the emergence of the curvature at the flow front is attributed to the spatial and temporal changes in viscosity, the foam expansion process is driven by the source term S_p. Hence, in Figs. 4.10, the propagation of the foam height at the middle and at the wall from our simulation is compared with those obtained in experiments; whilst the heights at the middle, in both cases, agree quite well (Fig.4.10(a)), on the wall, our result seem to overestimate the experimental values, see Fig.4.10(b). This observation may be attributed to the choice of S_p, since we had assumed uniform expansion in our model. As earlier mentioned, in our future works, we explore the possibility of non-uniform expansion.

4.6 Conclusion

In this work, we proposed and validated an alternative model approach, capable of predicting the complicated flow behavior observed in self expanding PU foams. This experimentally motivated idea suggests an incorporation of a source term S_p to the mass conservation equation; which enabled us to capture the complex physics seen in these expanding foams. The foaming polymer mixture is assumed to be a homogeneous incompressible liquid, subject to no slip conditions on the walls and non-isothermal conditions in the domain. Finite volume techniques on collocated grids are used as numerical tools to solve the coupled system of time dependent partial differential equations emerging from the mathematical model.

Whilst the source term is responsible for driving the flow and ensuring that the flow ceases at the end of the expansion, after reaching the expected heights, we further observe that an appropriate choice of non-isothermal viscosity model enables an adequate prediction of the curvature in the flow front. The obvious behavior of expanding foams is that of transition from a reacting viscous liquid to an elastic solid, with high generation of heat resulting from exothermic reactions, and the highest heat generated at the core of the setup. Hence, due to this temperature variations within the domain, the coupling of temperature and viscosity ensures that the mixture viscosity at the walls becomes higher than those at the center, thereby leading to a fountain flow in the front through the center.

Although the positive comparison of results obtained from our simulations with those from experiments proves the validity of this modelling approach, we hereby remark that uniform expansion of all foam bubbles within the foam matrix was assumed. This may not be optimal in general as has been reported in the literature, [16]. We therefore intend to factor in non-uniform expansions in future investigations.

The ideas discussed in this study can be useful in industrial applications of expanding foams, especially in cases where there is need to make an a-priori estimate of the quantity of material required to adequately fill the mold cavity, thereby minimizing material loss or waste which may result from excess expansion in reaction injection molding.

Chapter 5

Concluding Remarks

This thesis focuses on the computational and experimental investigations of the flow of non-Newtonian fluids under different physical and geometric conditions. In particular three non-Newtonian flow problems motivated by relevant industrial applications are considered.

The onset of instabilities, which manifest as shear bands, has been experimentally observed in the flow of some complex fluids whose stress behavior can be described by viscoelastic constitutive models. Our first investigation (chapter 2) limits attention to pipe flow of fluids described by one such viscoelastic constitutive model, the Joshnson-Segalman model. We conduct numerical investigations on the combined effects of wall slip and non-isothermal conditions on the resulting pressure driven pipe flow of fluids of the Johnson-Segalman type. Strong relationship are revealed between wall slip, non-isothermal conditions and shear banding. The fluid temperature is shown to increase with wall slip, under shear banding conditions, thereby resulting in, say, enhanced susceptibility to thermal runaway phenomena. Under relevant wall slip and shear banding conditions, the investigation further illustrates the relationships between fluid viscoelasticity and corresponding thermal loading properties. In particular, higher fluid viscoelasticity was shown to lead to lower critical Frank-Kamenetskii parameter values, thereby resulting in increased susceptibility to thermal runaway phenomena. Efficient finite difference techniques are employed for the numerical solution processes.

In a related study (chapter 3), phenomena associated with shear banded flows of viscoelastic fluids, governed by the diffusive Johnson-Segalman constitutive model, in both pipe and coaxial annular flow geometries was investigated numerically. We demonstrate that under conditions of shear banding, the uniquely selected stress paths and critical shear stress values are affected by temperature, fluid injection, viscoelasticity and geometric constrictions. These observations are particularly in agreement with those reported in the literatures. The computational solution processes are also conducted via efficient finite difference methodologies.

In the third and final study (chapter 4), an experimentally motivated modelling approach is used to formulate mathematical models capable of predicting the self expansion phenomena observed in reaction injection molding process of polyurethane foams. For an accurate description of the temperature distribution within the bulk flow as well as the progression of the expanding foam front, the finite volume method is used as numerical tool. This method was chosen because of its conservative nature. The computational solutions from the finite volume solvers were compared with available experimental results. Qualitative agreement is observed between the computational and experimental results showing that our computational techniques offer good predictions of the complex dynamics seen in expanding polymeric foams. We also offer suggestions of improvement in the mathematical models to enhance quantitative agreement with experiments.

The investigations in this thesis were not meant to be exhaustive in terms of the behavior of all relevant and available viscoelastic stress constitutive models. The numerical results obtained in the first two studies offer excellent insights into the relevant contributions of wall slip and non-isothermal conditions on the shear banding phenomena in non-isothermal flow of viscoelastic fluids. The computational and experimental results obtained in the final study similarly offers excellent insights into the self expansion processes observed in reacting polyurethane foams.

Appendix

Appendix A

Summary of Equations

A.1 Gradient of the velocity vector in cylindrical coordinates

Given the velocity vector $\boldsymbol{v}$ with components (u, v, w), then the velocity gradient in cylindrical coordinates is,

$$\nabla \boldsymbol{v} = \begin{pmatrix} \frac{\partial u}{\partial r} & \frac{1}{r}\left(\frac{\partial u}{\partial \theta} - v\right) & \frac{\partial u}{\partial z} \\ \frac{\partial v}{\partial r} & \frac{1}{r}\left(\frac{\partial v}{\partial \theta} + u\right) & \frac{\partial v}{\partial z} \\ \frac{\partial w}{\partial r} & \frac{1}{r}\frac{\partial w}{\partial \theta} & \frac{\partial w}{\partial z} \end{pmatrix}. \tag{A.1}$$

A.2 Divergence of the velocity vector in cylindrical coordinates

$$\nabla \cdot \boldsymbol{v} = trace(\nabla \boldsymbol{v}) = \frac{\partial u}{\partial r} + \frac{1}{r}\left(\frac{\partial v}{\partial \theta} + u\right) + \frac{\partial w}{\partial z}. \tag{A.2}$$

A.3 Laplace of the velocity vector in cylindrical coordinates

$$\boldsymbol{\Delta v} = \nabla^2 \boldsymbol{v} = \nabla \cdot \nabla \boldsymbol{v} = \frac{\partial^2 u}{\partial r^2} + \frac{1}{r}\frac{\partial u}{\partial r} + \frac{1}{r^2}\frac{\partial v}{\partial \theta^2} + \frac{\partial^2 w}{\partial z^2}. \tag{A.3}$$

A.4 Gradient of the stress tensor in cylindrical coordinates

Given a stress Tensor $\boldsymbol{T}$, then the stress gradient in cylindrical coordinates is,

$$\begin{aligned}
\nabla \boldsymbol{T} = {} & \frac{\partial T_{rr}}{\partial r} e_r \otimes e_r \otimes e_r + \frac{1}{r}\left[\frac{\partial T_{rr}}{\partial \theta} - (T_{\theta r} + T_{r\theta})\right] e_r \otimes e_r \otimes e_\theta + \frac{\partial T_{rr}}{\partial z} e_r \otimes e_r \otimes e_z \\
& + \frac{\partial T_{r\theta}}{\partial r} e_r \otimes e_\theta \otimes e_r + \frac{1}{r}\left[\frac{\partial T_{r\theta}}{\partial \theta} + (T_{rr} - T_{\theta\theta})\right] e_r \otimes e_\theta \otimes e_\theta + \frac{\partial T_{r\theta}}{\partial z} e_r \otimes e_\theta \otimes e_z \\
& + \frac{\partial T_{rz}}{\partial r} e_r \otimes e_z \otimes e_r + \frac{1}{r}\left[\frac{\partial T_{rz}}{\partial \theta} - T_{\theta z}\right] e_r \otimes e_z \otimes e_\theta + \frac{\partial T_{rz}}{\partial z} e_r \otimes e_z \otimes e_z \\
& + \frac{\partial T_{\theta r}}{\partial r} e_\theta \otimes e_r \otimes e_r + \frac{1}{r}\left[\frac{\partial T_{\theta r}}{\partial \theta} + (T_{rr} - T_{\theta\theta})\right] e_\theta \otimes e_r \otimes e_\theta + \frac{\partial T_{\theta r}}{\partial z} e_\theta \otimes e_r \otimes e_z \\
& + \frac{\partial T_{\theta\theta}}{\partial r} e_\theta \otimes e_\theta \otimes e_r + \frac{1}{r}\left[\frac{\partial T_{\theta\theta}}{\partial \theta} + (T_{\theta r} + T_{r\theta})\right] e_\theta \otimes e_\theta \otimes e_\theta + \frac{\partial T_{\theta\theta}}{\partial z} e_\theta \otimes e_\theta \otimes e_z \\
& + \frac{\partial T_{\theta z}}{\partial r} e_\theta \otimes e_z \otimes e_r + \frac{1}{r}\left[\frac{\partial T_{\theta z}}{\partial \theta} + T_{rz}\right] e_\theta \otimes e_z \otimes e_\theta + \frac{\partial T_{\theta z}}{\partial z} e_\theta \otimes e_z \otimes e_z \\
& + \frac{\partial T_{zr}}{\partial r} e_z \otimes e_r \otimes e_r + \frac{1}{r}\left[\frac{\partial T_{zr}}{\partial \theta} - T_{z\theta}\right] e_z \otimes e_r \otimes e_\theta + \frac{\partial T_{zr}}{\partial z} e_z \otimes e_r \otimes e_z \\
& + \frac{\partial T_{z\theta}}{\partial r} e_z \otimes e_\theta \otimes e_r + \frac{1}{r}\left[\frac{\partial T_{z\theta}}{\partial \theta} + T_{zr}\right] e_z \otimes e_\theta \otimes e_\theta + \frac{\partial T_{z\theta}}{\partial z} e_z \otimes e_\theta \otimes e_z \\
& + \frac{\partial T_{zz}}{\partial r} e_z \otimes e_z \otimes e_r + \frac{1}{r}\frac{\partial T_{zz}}{\partial \theta} e_z \otimes e_z \otimes e_\theta + \frac{\partial T_{zz}}{\partial z} e_z \otimes e_z \otimes e_z.
\end{aligned} \tag{A.4}$$

A.5 Divergence of the stress tensor in cylindrical coordinates

$$\begin{aligned}
\nabla \cdot \boldsymbol{T} = & \left[\frac{1}{r}\frac{\partial}{\partial r}(rT_{rr}) + \frac{1}{r}\frac{\partial}{\partial \theta}T_{\theta r} + \frac{\partial}{\partial z}T_{zr} - \frac{T_{\theta\theta}}{r}\right] e_r \\
& + \left[\frac{1}{r^2}\frac{\partial}{\partial r}(r^2 T_{r\theta}) + \frac{1}{r}\frac{\partial}{\partial \theta}T_{\theta\theta} + \frac{\partial}{\partial z}T_{z\theta} + \frac{T_{\theta r} - T_{r\theta}}{r}\right] e_\theta \\
& + \left[\frac{1}{r}\frac{\partial}{\partial r}(rT_{rz}) + \frac{1}{r}\frac{\partial}{\partial \theta}T_{\theta z} + \frac{\partial}{\partial z}T_{zz}\right] e_z.
\end{aligned} \tag{A.5}$$

A.6 Laplace of the symmetric stress tensor in cylindrical coordinates

The non-identical terms are,

$$\begin{aligned}
\nabla^2 \boldsymbol{T} = \nabla \cdot \nabla \boldsymbol{T} = & \left[\boldsymbol{\Delta}(T_{rr}) - \frac{2}{r^2}(T_{rr} - T_{\theta\theta}) - \frac{4}{r^2}\frac{\partial T_{r\theta}}{\partial \theta}\right] e_r \otimes e_r + \\
& \left[\boldsymbol{\Delta}(T_{\theta\theta}) + \frac{2}{r^2}(T_{rr} - T_{\theta\theta}) + \frac{4}{r^2}\frac{\partial T_{r\theta}}{\partial \theta}\right] e_\theta \otimes e_\theta + \\
& \left[\boldsymbol{\Delta}(T_{r\theta}) - \frac{4}{r^2}T_{r\theta} + \frac{2}{r^2}\frac{\partial}{\partial \theta}(T_{rr} + T_{\theta\theta})\right] e_r \otimes e_r + \\
& \left[\boldsymbol{\Delta}(T_{rz}) - \frac{1}{r^2}T_{rz} - \frac{2}{r^2}\frac{\partial T_{\theta z}}{\partial \theta}\right] e_r \otimes e_z + \\
& \left[\boldsymbol{\Delta}(T_{\theta z}) - \frac{1}{r^2}T_{\theta z} - \frac{2}{r^2}\frac{\partial T_{rz}}{\partial \theta}\right] e_\theta \otimes e_z + \\
& [\boldsymbol{\Delta}(T_{zz})] e_z \otimes e_z,
\end{aligned} \tag{A.6}$$

where the operation of $\boldsymbol{\Delta}$ on a scaler f is defined by

$$\boldsymbol{\Delta} f = \frac{\partial^2 f}{\partial r^2} + \frac{1}{r}\frac{\partial f}{\partial r} + \frac{1}{r}\frac{\partial^2 f}{\partial \theta^2} + \frac{\partial^2 f}{\partial z^2}. \tag{A.7}$$

Due to symmetry considerations, we have

$$(\boldsymbol{\Delta T})_{rz} = (\boldsymbol{\Delta T})_{zr}, \tag{A.8}$$

$$(\boldsymbol{\Delta T})_{\theta z} = (\boldsymbol{\Delta T})_{z\theta}, \tag{A.9}$$

$$(\boldsymbol{\Delta T})_{r\theta} = (\boldsymbol{\Delta T})_{\theta r}. \tag{A.10}$$

A.7 Material Derivative of the stress Tensor in cylindrical coordinates

$$\begin{aligned}
\frac{\partial}{\partial t}\boldsymbol{T} + \boldsymbol{v}\cdot\nabla\boldsymbol{T} = {} & \left[\left(\frac{\partial}{\partial t} + \boldsymbol{v}\cdot\nabla\right) T_{rr} - \frac{v}{r}(T_{r\theta} + T_{\theta r})\right] e_r \otimes e_r \\
& + \left[\left(\frac{\partial}{\partial t} + \boldsymbol{v}\cdot\nabla\right) T_{r\theta} + \frac{v}{r}(T_{rr} - T_{\theta\theta})\right] e_r \otimes e_\theta \\
& + \left[\left(\frac{\partial}{\partial t} + \boldsymbol{v}\cdot\nabla\right) T_{rz} - \frac{v}{r} T_{\theta z}\right] e_r \otimes e_z \\
& + \left[\left(\frac{\partial}{\partial t} + \boldsymbol{v}\cdot\nabla\right) T_{\theta r} + \frac{v}{r}(T_{rr} - T_{\theta\theta})\right] e_\theta \otimes e_r \\
& + \left[\left(\frac{\partial}{\partial t} + \boldsymbol{v}\cdot\nabla\right) T_{\theta\theta} + \frac{v}{r}(T_{r\theta} + T_{\theta r})\right] e_\theta \otimes e_\theta \\
& + \left[\left(\frac{\partial}{\partial t} + \boldsymbol{v}\cdot\nabla\right) T_{\theta z} + \frac{v}{r} T_{rz}\right] e_r \otimes e_z \\
& + \left[\left(\frac{\partial}{\partial t} + \boldsymbol{v}\cdot\nabla\right) T_{z\theta} + \frac{v}{r} T_{zr}\right] e_z \otimes e_\theta \\
& + \left[\left(\frac{\partial}{\partial t} + \boldsymbol{v}\cdot\nabla\right) T_{zr} - \frac{v}{r} T_{zr}\right] e_z \otimes e_r \\
& + \left[\left(\frac{\partial}{\partial t} + \boldsymbol{v}\cdot\nabla\right) T_{zz}\right] e_z \otimes e_z,
\end{aligned} \tag{A.11}$$

where

$$(\boldsymbol{v}\cdot\nabla) = u\frac{\partial}{\partial r} + \frac{v}{r}\frac{\partial}{\partial\theta} + w\frac{\partial}{\partial z}. \tag{A.12}$$

A.8 Equations of Motion in Cylindrical Coordinates

The incompressible continuity equation in coordinate free notation reads,

$$\nabla \cdot \boldsymbol{v} = 0. \tag{A.13}$$

The velocity field for axi-symmetric flow with porous walls can be written, $\boldsymbol{v} = u(r,t)\hat{e}_r + w(r,t)\hat{e}_z$. In this case, Eqs. (A.2) and (A.13) lead to,

$$\frac{\partial u}{\partial r} + \frac{u}{r} = 0, \tag{A.14}$$

so that,

$$\frac{\partial u}{\partial r} = -\frac{u}{r}, \tag{A.15}$$

where $u = b/r$, and b is a constant. The Momentum Equations in coordinate free notation read,

$$\rho \frac{D\boldsymbol{v}}{Dt} = -\nabla P + \nabla' \cdot \boldsymbol{T}, \tag{A.16}$$

where

$$\boldsymbol{T} = \eta_s \boldsymbol{D} + \boldsymbol{\sigma}. \tag{A.17}$$

In cylindrical coordinates, the deformation rate tensor becomes,

$$\boldsymbol{D} = [\nabla \boldsymbol{v} + (\nabla \boldsymbol{v})^T] = \begin{pmatrix} 2\frac{\partial u}{\partial r} & 0 & \frac{\partial w}{\partial r} \\ 0 & \frac{2u}{r} & 0 \\ \frac{\partial w}{\partial r} & 0 & 0 \end{pmatrix}. \tag{A.18}$$

The momentum equations (A.16) in cylindrical coordinates can therefore be written as,

$$\begin{bmatrix} 0 \\ 0 \\ \frac{\partial w}{\partial t} \end{bmatrix} + \begin{bmatrix} u\frac{\partial u}{\partial r} \\ 0 \\ u\frac{\partial w}{\partial r} \end{bmatrix} = \begin{bmatrix} -\frac{\partial P}{\partial r} \\ 0 \\ -\frac{\partial P}{\partial z} \end{bmatrix} + \nabla \cdot \begin{pmatrix} 2\eta_s\frac{\partial u}{\partial r} & 0 & \eta_s\frac{\partial w}{\partial r} \\ 0 & 2\eta_s\frac{u}{r} & 0 \\ \eta_s\frac{\partial w}{\partial r} & 0 & 0 \end{pmatrix}$$
$$+\nabla \cdot \begin{pmatrix} \sigma_{rr} & \sigma_{r\theta} & \sigma_{rz} \\ \sigma_{\theta r} & \sigma_{\theta\theta} & \sigma_{\theta z} \\ \sigma_{zr} & \sigma_{z\theta} & \sigma_{rz} \end{pmatrix} \quad . \quad (A.19)$$

Since $\boldsymbol{\sigma} = \boldsymbol{\sigma}(r,t)$ and $\sigma_{r\theta} = \sigma_{\theta z} = 0$, then Eq. (A.15) implies that the momentum equations reduce to,

$$\begin{bmatrix} 0 \\ 0 \\ \frac{\partial w}{\partial t} \end{bmatrix} + \begin{bmatrix} u\frac{\partial u}{\partial r} \\ 0 \\ u\frac{\partial w}{\partial r} \end{bmatrix} = \begin{bmatrix} -\frac{\partial P}{\partial r} \\ 0 \\ -\frac{\partial P}{\partial z} \end{bmatrix} + \begin{bmatrix} -\frac{2u}{r}\frac{\partial}{\partial r}\eta_s \\ 0 \\ \frac{\partial}{\partial r}\left(\eta_s\frac{\partial}{\partial r}w\right) + \frac{\eta_s}{r}\frac{\partial}{\partial r}w \end{bmatrix}$$
$$+\begin{bmatrix} \frac{\partial}{\partial r}\sigma_{rr} + \frac{1}{r}\left(\sigma_{rr} - \sigma_{\theta\theta}\right) \\ 0 \\ \frac{1}{r}\frac{\partial}{\partial r}\left(r\sigma_{rz}\right) \end{bmatrix} \quad . \quad (A.20)$$

Dimensionless momentum equations in cylindrical coordinates

Using the non-dimensional variables and parameters below

$$r' = \frac{r}{\zeta},\ z' = \frac{z}{\zeta},\ w' = \frac{w}{U},\ u' = \frac{u}{U},\ t' = \frac{U}{\zeta}t,\ \boldsymbol{\sigma}' = \frac{\zeta}{\eta_r U}\boldsymbol{\sigma},\ P' = \frac{R_o}{U\eta_r}P,$$

$$Re = \frac{\rho U R_o}{\eta_r}, \zeta = \frac{R_o}{\chi}, \eta_s = (1-\beta)\eta_r\mu(\theta).$$

We derive the non-dimensional equations governing the conservation of momentum in the flow set-up. Hence the Eq.(A.22) becomes

$$\frac{U^2}{\zeta}\begin{pmatrix} u'\frac{\partial u'}{\partial r'} \\ 0 \\ \frac{\partial w'}{\partial t'} + u'\frac{\partial w'}{\partial r'} \end{pmatrix} = \frac{U\eta_r}{R_o\zeta}\begin{pmatrix} -\frac{\partial P}{\partial r'} \\ 0 \\ -\frac{\partial P}{\partial z'} \end{pmatrix} + \frac{\eta_r U}{\zeta^2}\begin{pmatrix} -(1-\beta)\frac{2u'}{r'}\frac{\partial}{\partial r'}\mu(\theta) + \frac{\partial}{\partial r'}{\sigma'}_{rr} + \frac{1}{r'}\left({\sigma'}_{rr} - {\sigma'}_{\theta\theta}\right) \\ 0 \\ \frac{\partial}{\partial r'}\left((1-\beta)\mu(\theta)\frac{\partial}{\partial r'}w'\right) + \frac{(1-\beta)\mu(\theta)}{r'}\frac{\partial}{\partial r'}w' + \frac{1}{r'}\frac{\partial}{\partial r'}\left(r'{\sigma'}_{rz}\right) \end{pmatrix}. \tag{A.21}$$

Removing the primes and rearranging we obtain the momentum equations in non-dimensional form as

$$\frac{Re}{\chi}\begin{pmatrix} u\frac{\partial u}{\partial r} \\ 0 \\ \frac{\partial w}{\partial t} + u\frac{\partial w}{\partial r} \end{pmatrix} = \frac{1}{\chi}\begin{pmatrix} -\frac{\partial P}{\partial r} \\ 0 \\ -\frac{\partial P}{\partial z} \end{pmatrix} + \begin{pmatrix} -(1-\beta)\frac{2u}{r}\frac{\partial}{\partial r}\mu(\theta) + \frac{\partial}{\partial r}\sigma_{rr} + \frac{1}{r}\left(\sigma_{rr} - \sigma_{\theta\theta}\right) \\ 0 \\ (1-\beta)\frac{\partial}{\partial r}\left(\mu(\theta)\frac{\partial}{\partial r}w\right) + (1-\beta)\frac{\mu(\theta)}{r}\frac{\partial}{\partial r}w + \frac{1}{r}\frac{\partial}{\partial r}\left(r\sigma_{rz}\right) \end{pmatrix}. \tag{A.22}$$

A.9 Temperature equation in cylindrical coordinates

$$\rho c_p\left(\frac{\partial T'}{\partial t'} + u'\frac{\partial T'}{\partial r'}\right) = \frac{1}{r'}\frac{\partial}{\partial r'}\left(\kappa r'\frac{\partial T'}{\partial r'}\right) + \bar{Q}'_D + QAC\exp\left(\frac{-E}{RT'}\right). \tag{A.23}$$

Non-dimensional Temperature equations

Using the following non-dimensional variables and parameters,

$$r = \frac{r'}{\zeta}, u = \frac{u'}{U}, t = \frac{U}{\zeta}t', \theta = \frac{T' - T_0}{\alpha T_0}, Q_D = \frac{\zeta^2}{\eta_r U^2}Q'_D,$$

$$Re = \frac{\rho U R_o}{\eta_r}, Pr = \frac{c_p \eta_r}{\kappa}, Br = \frac{\eta_r U^2}{\alpha \kappa T_0}, \alpha = \frac{RT_o}{E}, \delta = \frac{R_o^2 QACE}{RT_0^2 \kappa} \exp(-\frac{1}{\alpha}),$$

Eq. (A.23) becomes,

$$\begin{aligned} \frac{\rho c_p \alpha T_0 U}{\kappa \zeta}\left(\frac{\partial \theta}{\partial t} + u\frac{\partial \theta}{\partial r}\right) &= \frac{\alpha T_0}{\zeta^2}\frac{1}{r}\frac{\partial}{\partial r}\left(r\frac{\partial \theta}{\partial r}\right) + \frac{\eta_r U^2}{\zeta^2 \kappa}Q_D \\ &+ \frac{QAC}{\kappa}\exp\left(\frac{-E}{RT_o(1+\alpha\theta)}\right). \end{aligned} \tag{A.24}$$

Multiplying through by $\frac{\zeta^2}{\alpha T_0}$ leads to,

$$\begin{aligned} \frac{\rho c_p \zeta U}{\kappa}\left(\frac{\partial \theta}{\partial t} + u\frac{\partial \theta}{\partial r}\right) &= \frac{1}{r}\frac{\partial}{\partial r}\left(r\frac{\partial \theta}{\partial r}\right) + \frac{\eta_r U^2}{\alpha T_0 \kappa}Q_D \\ &+ \frac{\zeta^2 QAC}{\kappa \alpha T_0}\exp\left(\frac{-1}{\alpha}\left(\frac{1}{1+\alpha\theta}\right)\right). \end{aligned} \tag{A.25}$$

Since $\zeta = \frac{R_o}{\chi}$, Eq. A.23 becomes,

$$\begin{aligned} \frac{\rho c_p R_o U}{\kappa \chi}\left(\frac{\partial \theta}{\partial t} + u\frac{\partial \theta}{\partial r}\right) = \frac{1}{r}\frac{\partial}{\partial r}\left(r\frac{\partial \theta}{\partial r}\right) + \frac{\eta_r U^2}{\alpha T_0 \kappa}Q_D \\ + \frac{R_o^2 QAC}{\chi^2 \kappa \alpha T_0}\exp\left(\frac{-1}{\alpha}\left(\frac{1}{1+\alpha\theta} + 1 - 1\right)\right), \end{aligned} \tag{A.26}$$

which can be written as,

$$\begin{aligned}\frac{\rho c_p R_o U \eta_r}{\kappa \eta_r \chi}\left(\frac{\partial\theta}{\partial t}+u\frac{\partial\theta}{\partial r}\right) &= \frac{1}{r}\frac{\partial}{\partial r}\left(r\frac{\partial\theta}{\partial r}\right)+\frac{\eta_r U^2}{\alpha T_0 \kappa}Q_D \\ &\quad +\frac{R_o^2 QAC}{\chi^2\kappa\alpha T_0}\exp\left(\frac{-1}{\alpha}\left(\frac{-\alpha\theta}{1+\alpha\theta}\right)+\left(\frac{-1}{\alpha}\right)\right).\end{aligned} \tag{A.27}$$

Using the dimensionless parameters, we have that

$$\begin{aligned}\frac{RePr}{\chi}\left(\frac{\partial\theta}{\partial t}+u\frac{\partial\theta}{\partial r}\right) &= \frac{1}{r}\frac{\partial}{\partial r}\left(r\frac{\partial\theta}{\partial r}\right)+BrQ_D \\ &\quad +\frac{R_o^2 QACE}{\chi^2\kappa R T_o^2}\exp\left(\frac{-1}{\alpha}\right)\exp\left(\frac{\theta}{1+\alpha\theta}\right),\end{aligned} \tag{A.28}$$

leading to,

$$RePr\left(\frac{\partial\theta}{\partial t}+u\frac{\partial\theta}{\partial r}\right)=\chi\frac{1}{r}\frac{\partial}{\partial r}\left(r\frac{\partial\theta}{\partial r}\right)+\chi BrQ_D+\frac{\delta}{\chi}\exp\left(\frac{\theta}{1+\alpha\theta}\right). \tag{A.29}$$

A.10 Stress constitutive equations in cylindrical coordinates

$$\boldsymbol{\sigma}'+\lambda'\left(\overset{\square}{\boldsymbol{\sigma}'}-\boldsymbol{\sigma}'\frac{D}{Dt'}\ln\left(\frac{T'}{T_0}\right)\right)=\eta_p\boldsymbol{D}'+\psi\lambda'\nabla^2\boldsymbol{\sigma}'. \tag{A.30}$$

The stress equations in dimensionless form:

Using the following dimensionless variables and parameters

$$r=\frac{r'}{\zeta},\nabla=\zeta\nabla',\ u=\frac{u'}{U},\ t=\frac{U}{\zeta}t',\ \boldsymbol{\sigma}=\frac{\zeta}{\eta_r U}\boldsymbol{\sigma}',\theta=\frac{T'-T_0}{\alpha T_0},$$

$$\overset{\square}{\boldsymbol{\sigma}}=\frac{\zeta^2}{\eta_r U^2}\overset{\square}{\boldsymbol{\sigma}'},\eta_p=\eta_r\mu(\theta),\lambda'=\lambda_r\lambda(\theta),\ Wi=\frac{\lambda_r U}{R_o},\ \varepsilon=\frac{\psi\lambda_r}{R_o^2}=\frac{\epsilon}{R_o^2},$$

the stress constitutive equations in dimensionless form become,

$$\begin{aligned}\frac{\eta_r U}{\zeta}\boldsymbol{\sigma} + \lambda_r\lambda(\theta)\frac{\eta_r U^2}{\zeta^2}\left[\overset{\square}{\boldsymbol{\sigma}} - \boldsymbol{\sigma}\frac{\alpha}{(1+\alpha\theta)}\left(\frac{\partial\theta}{\partial t}+u\frac{\partial\theta}{\partial r}\right)\right] &= \frac{\eta_r U}{\zeta}\beta\mu(\theta)\boldsymbol{D} \\ &+\lambda(\theta)\frac{\eta_r U\lambda_r\psi}{\zeta^3}\nabla^2\boldsymbol{\sigma}.\end{aligned} \tag{A.31}$$

Multiplying through by $\frac{\zeta}{\eta_r U}$, Eq. (A.31) simplifies to

$$\boldsymbol{\sigma} + \lambda(\theta)\frac{\lambda_r U}{\zeta}\left[\overset{\square}{\boldsymbol{\sigma}} - \boldsymbol{\sigma}\frac{\alpha}{(1+\alpha\theta)}\left(\frac{\partial\theta}{\partial t}+u\frac{\partial\theta}{\partial r}\right)\right] = \beta\mu(\theta)\boldsymbol{D} + \lambda(\theta)\frac{\lambda_r\psi}{\zeta^2}\nabla^2\boldsymbol{\sigma}. \tag{A.32}$$

Since $\zeta = R_o/\chi$, then Eq. (A.30) in dimensionless form reads,

$$\boldsymbol{\sigma} + \lambda(\theta)\chi Wi\left[\overset{\square}{\boldsymbol{\sigma}} - \boldsymbol{\sigma}\frac{\alpha}{(1+\alpha\theta)}\left(\frac{\partial\theta}{\partial t}+u\frac{\partial\theta}{\partial r}\right)\right] = \beta\mu(\theta)\boldsymbol{D} + \chi^2\lambda(\theta)\varepsilon\nabla^2\boldsymbol{\sigma}. \tag{A.33}$$

Stress Equations in cylindrical coordinates

Recall that

$$\begin{aligned}\overset{\square}{\boldsymbol{\sigma}} = (1-\frac{\xi}{2})&\left(\frac{D}{Dt}\boldsymbol{\sigma} - \boldsymbol{\sigma}\cdot\nabla\boldsymbol{v} - (\nabla\boldsymbol{v})^T\cdot\boldsymbol{\sigma}\right) \\ &+\frac{\xi}{2}\left(\frac{D}{Dt}\boldsymbol{\sigma} + \nabla\boldsymbol{v}\cdot\boldsymbol{\sigma} + \boldsymbol{\sigma}\cdot(\nabla\boldsymbol{v})^T\right).\end{aligned} \tag{A.34}$$

Following Eq. (A.11) and the fact that $\boldsymbol{\sigma} = \boldsymbol{\sigma}(t,r)$ we have that

$$-\left[\boldsymbol{\sigma}\cdot\nabla\boldsymbol{v} + (\nabla\boldsymbol{v})^T\cdot\boldsymbol{\sigma}\right] = \begin{bmatrix} 2\frac{u}{r}\sigma_{rr} - 2\sigma_{rz}\frac{\partial}{\partial r}w & 0 & \frac{u}{r}\sigma_{rz} - \sigma_{zz}\frac{\partial}{\partial r}w \\ 0 & -2\frac{u}{r}\sigma_{\theta\theta} & 0 \\ \frac{u}{r}\sigma_{rz} - \sigma_{zz}\frac{\partial}{\partial r}w & 0 & 0 \end{bmatrix}, \tag{A.35}$$

$$[\nabla \boldsymbol{v} \cdot \boldsymbol{\sigma} + \boldsymbol{\sigma} \cdot (\nabla \boldsymbol{v})^T] = \begin{bmatrix} -2\frac{u}{r}\sigma_{rr} & 0 & -\frac{u}{r}\sigma_{rz} + \sigma_{rr}\frac{\partial}{\partial r}w \\ 0 & 2\frac{u}{r}\sigma_{\theta\theta} & 0 \\ -\frac{u}{r}\sigma_{rz} + \sigma_{rr}\frac{\partial}{\partial r}w & 0 & 0 \end{bmatrix}, \tag{A.36}$$

and

$$\frac{D}{Dt}\boldsymbol{\sigma} = \begin{bmatrix} \left(\frac{\partial}{\partial t} + u\frac{\partial}{\partial r}\right)\sigma_{rr} & 0 & \left(\frac{\partial}{\partial t} + u\frac{\partial}{\partial r}\right)\sigma_{rz} \\ 0 & \left(\frac{\partial}{\partial t} + u\frac{\partial}{\partial r}\right)\sigma_{\theta\theta} & 0 \\ \left(\frac{\partial}{\partial t} + u\frac{\partial}{\partial r}\right)\sigma_{zr} & 0 & \left(\frac{\partial}{\partial t} + u\frac{\partial}{\partial r}\right)\sigma_{zz} \end{bmatrix}. \tag{A.37}$$

Combining Eqs. (A.35)-(A.37) leads to,

$$\overset{\square}{\sigma}_{rr} = \left(\frac{\partial}{\partial t} + u\frac{\partial}{\partial r}\right)\sigma_{rr} + 2(1-\xi)\frac{u}{r}\sigma_{rr} + (\xi - 2)\sigma_{rz}\frac{\partial}{\partial r}w, \tag{A.38}$$

$$\overset{\square}{\sigma}_{rz} = \left(\frac{\partial}{\partial t} + u\frac{\partial}{\partial r}\right)\sigma_{rz} + (1-\xi)\frac{u}{r}\sigma_{rz} + \left[\left(\frac{\xi}{2} - 1\right)\sigma_{zz} + \frac{\xi}{2}\sigma_{rr}\right]\frac{\partial}{\partial r}w, \tag{A.39}$$

$$\overset{\square}{\sigma}_{\theta\theta} = \left(\frac{\partial}{\partial t} + u\frac{\partial}{\partial r}\right)\sigma_{\theta\theta} + 2(\xi - 1)\frac{u}{r}\sigma_{\theta\theta}, \tag{A.40}$$

$$\overset{\square}{\sigma}_{zz} = \left(\frac{\partial}{\partial t} + u\frac{\partial}{\partial r}\right)\sigma_{zz} + \xi\sigma_{rz}\frac{\partial}{\partial r}w. \tag{A.41}$$

Similarly,

$$\boldsymbol{\sigma}\frac{\alpha}{(1+\alpha\theta)}\left(\frac{\partial\theta}{\partial t} + u\frac{\partial\theta}{\partial r}\right) = \begin{bmatrix} \sigma_{rr} & 0 & \sigma_{rz} \\ 0 & \sigma_{rr} & 0 \\ \sigma_{zr} & 0 & \sigma_{zz} \end{bmatrix} \frac{\alpha}{(1+\alpha\theta)}\left(\frac{\partial\theta}{\partial t} + u\frac{\partial\theta}{\partial r}\right). \tag{A.42}$$

Substituting the convective derivatives Eqs.(A.38 - A.41) and Eq. (A.42) into (A.33) as well as using the Laplace of the stress tensor as described in appendix A.7 and rearranging, we obtain the stress equations in cylindrical coordinates as *rr Component of the stress tensor*

$$
\begin{aligned}
\Phi\left(\frac{\partial\sigma_{rr}}{\partial t}+u\frac{\partial\sigma_{rr}}{\partial r}\right) &= \varepsilon\lambda(\theta)\frac{\partial^2\sigma_{rr}}{\partial r^2}+\frac{\varepsilon\lambda(\theta)}{r}\frac{\partial\sigma_{rr}}{\partial r} \\
&\quad+\left(\Phi\boldsymbol{D}_{(\theta)}-\frac{1}{\chi^2}-(1-\xi)\Phi\frac{2u}{r}-\frac{2\varepsilon\lambda(\theta)}{r^2}\right)\sigma_{rr} \\
&\quad+\left(\frac{2\varepsilon\lambda(\theta)}{r^2}\sigma_{\theta\theta}-(\xi-2)\Phi\sigma_{rz}\frac{\partial w}{\partial r}-\frac{\beta\mu(\theta)u}{r\chi^2}\right). \qquad (A.43)
\end{aligned}
$$

rz Component of the stress tensor

$$
\begin{aligned}
\Phi\left(\frac{\partial\sigma_{rz}}{\partial t}+u\frac{\partial\sigma_{rz}}{\partial r}\right) &= \varepsilon\lambda(\theta)\frac{\partial^2\sigma_{rz}}{\partial r^2}+\frac{\varepsilon\lambda(\theta)}{r}\frac{\partial\sigma_{rz}}{\partial r} \\
&\quad+\left(\Phi\boldsymbol{D}_{(\theta)}-\frac{1}{\chi^2}-(1-\xi)\Phi\frac{u}{r}-\frac{\varepsilon\lambda(\theta)}{r^2}\right)\sigma_{rz} \\
&\quad+\left(\frac{\beta\mu(\theta)}{\chi^2}-\Phi\left[(\frac{\xi}{2}-1)\sigma_{zz}+\frac{\xi}{2}\sigma_{rr}\right]\right)\frac{\partial w}{\partial r}. \qquad (A.44)
\end{aligned}
$$

θθ Component of the stress tensor

$$
\begin{aligned}
\Phi\left(\frac{\partial\sigma_{\theta\theta}}{\partial t}+u\frac{\partial\sigma_{\theta\theta}}{\partial r}\right) &= \varepsilon\lambda(\theta)\frac{\partial^2\sigma_{\theta\theta}}{\partial r^2}+\frac{\varepsilon\lambda(\theta)}{r}\frac{\partial\sigma_{\theta\theta}}{\partial r} \\
&\quad+\left(\Phi\boldsymbol{D}_{(\theta)}-\frac{1}{\chi^2}-(\xi-1)\Phi\frac{2u}{r}-\frac{2\varepsilon\lambda(\theta)}{r^2}\right)\sigma_{\theta\theta} \\
&\quad+\left(\frac{2\varepsilon\lambda(\theta)}{r^2}\sigma_{rr}+\frac{\beta\mu(\theta)u}{r\chi^2}\right). \qquad (A.45)
\end{aligned}
$$

zz Component of the stress tensor

$$
\begin{aligned}
\Phi\left(\frac{\partial\sigma_{zz}}{\partial t}+u\frac{\partial\sigma_{zz}}{\partial r}\right) &= \varepsilon\lambda(\theta)\frac{\partial^2\sigma_{zz}}{\partial r^2}+\frac{\varepsilon\lambda(\theta)}{r}\frac{\partial\sigma_{rz}}{\partial r} \\
&\quad+\left(\Phi\boldsymbol{D}_{(\theta)}-\frac{1}{\chi^2}\right)\sigma_{zz}-\xi\Phi\sigma_{rz}\frac{\partial w}{\partial r}. \qquad (A.46)
\end{aligned}
$$

where

$$\boldsymbol{D}_{(\theta)} = \frac{\alpha}{(1+\alpha\theta)}\left(\frac{\partial\theta}{\partial t} + u\frac{\partial\theta}{\partial r}\right), \quad \Phi = \frac{Wi\lambda(\theta)}{\chi}. \tag{A.47}$$

A.11 Mechanical dissipation

The mechanical dissipation function reads,

$$Q'_D = \eta_s \boldsymbol{D'} : \nabla\boldsymbol{v'} + \gamma\boldsymbol{\sigma'} : \boldsymbol{D'} + (1-\gamma)\frac{\hat{G}}{2(1-\xi)^2\lambda'}(I'_1 + tr(\boldsymbol{b'}^{-1}) - 6), \tag{A.48}$$

where

$$\boldsymbol{b'} = \frac{(1-\xi)}{\hat{G}}\boldsymbol{\sigma'} + \boldsymbol{I}. \tag{A.49}$$

Using the dimensionless variables and parameters

$$Q_D = \frac{\zeta^2}{\eta_r U^2}Q'_D, \ \boldsymbol{\sigma} = \frac{\zeta}{\eta_r U}\boldsymbol{\sigma'}, \boldsymbol{D} = \frac{\zeta}{U}\boldsymbol{D'}, Wi = \frac{\lambda_r U}{R_o}, \ \eta_s = \eta_r(1-\beta)\mu(\theta)$$

$$(I_1 \ + \ tr(\boldsymbol{b}^{-1}) \ - \ 6) = \frac{\zeta}{\eta_r U}(I'_1 \ + \ tr(\boldsymbol{b'}^{-1}) \ - \ 6),$$

where $\zeta = R_o/\chi$, then the heat dissipation function in dimensionless form becomes

$$\begin{aligned} Q_D \ &= \ \mu(\theta)(1-\beta)\boldsymbol{D} : \nabla\boldsymbol{v} + \gamma\boldsymbol{\sigma} : \boldsymbol{D} \\ &\quad +(1-\gamma)\frac{\hat{G}}{2\chi(1-\xi)^2 Wi\lambda(\theta)}(I_1 \ + \ tr(\boldsymbol{b}^{-1}) \ - \ 6). \end{aligned} \tag{A.50}$$

Since $\boldsymbol{A} : \boldsymbol{B} = A_{ij}B_{ij}$, we have that

$$\mu(\theta)(1-\beta)\boldsymbol{D} : \nabla\boldsymbol{v} = \mu(\theta)(1-\beta)\left(2\frac{u^2}{r^2} + \left(\frac{\partial w}{\partial r}\right)^2\right), \tag{A.51}$$

$$\gamma\boldsymbol{\sigma} : \boldsymbol{D} = -\gamma\frac{u}{r}(\sigma_{rr} - \sigma_{\theta\theta}) + 2\gamma\sigma_{rz}\frac{\partial}{\partial r}w, \tag{A.52}$$

where,

$$\boldsymbol{b} = \begin{bmatrix} \sigma_{rr}\frac{(1-\xi)}{\hat{G}}+1 & 0 & \sigma_{rz}\frac{(1-\xi)}{\hat{G}} \\ 0 & \sigma_{\theta\theta}\frac{(1-\xi)}{\hat{G}}+1 & 0 \\ \sigma_{rz}\frac{(1-\xi)}{\hat{G}} & 0 & \sigma_{zz}\frac{(1-\xi)}{\hat{G}}+1 \end{bmatrix}. \tag{A.53}$$

This leads to,

$$I_1 = tr(\boldsymbol{b}) = (\sigma_{rr}+\sigma_{\theta\theta}+\sigma_{zz})\frac{(1-\xi)}{\hat{G}}+3, \tag{A.54}$$

and

$$\begin{aligned} \boldsymbol{b}^{-1} = & \left[\frac{\sigma_{zz}\frac{(1-\xi)}{\hat{G}}+1}{\left(\sigma_{rr}\frac{(1-\xi)}{\hat{G}}+1\right)\left(\sigma_{zz}\frac{(1-\xi)}{\hat{G}}+1\right)-\left(\sigma_{rz}^2\left(\frac{(1-\xi)}{\hat{G}}\right)^2\right)}\right] e_r \otimes e_r \\ & + \left[\frac{-\sigma_{rz}\frac{(1-\xi)}{\hat{G}}}{\left(\sigma_{rr}\frac{(1-\xi)}{\hat{G}}+1\right)\left(\sigma_{zz}\frac{(1-\xi)}{\hat{G}}+1\right)-\left(\sigma_{rz}^2\left(\frac{(1-\xi)}{\hat{G}}\right)^2\right)}\right] e_r \otimes e_z \\ & + \left[\frac{1}{\sigma_{\theta\theta}\frac{(1-\xi)}{\hat{G}}+1}\right] e_\theta \otimes e_\theta \\ & + \left[\frac{-\sigma_{rz}\frac{(1-\xi)}{\hat{G}}}{\left(\sigma_{rr}\frac{(1-\xi)}{\hat{G}}+1\right)\left(\sigma_{zz}\frac{(1-\xi)}{\hat{G}}+1\right)-\left(\sigma_{rz}^2\left(\frac{(1-\xi)}{\hat{G}}\right)^2\right)}\right] e_z \otimes e_r \\ & + \left[\frac{\sigma_{rr}\frac{(1-\xi)}{\hat{G}}+1}{\left(\sigma_{rr}\frac{(1-\xi)}{\hat{G}}+1\right)\left(\sigma_{zz}\frac{(1-\xi)}{\hat{G}}+1\right)-\left(\sigma_{rz}^2\left(\frac{(1-\xi)}{\hat{G}}\right)^2\right)}\right] e_r \otimes e_r. \end{aligned} \tag{A.55}$$

We therefore have,

$$tr(\boldsymbol{b}^{-1}) = \frac{(\sigma_{zz}+\sigma_{rr})\frac{(1-\xi)}{\hat{G}}+2}{\left(\sigma_{rr}\frac{(1-\xi)}{\hat{G}}+1\right)\left(\sigma_{zz}\frac{(1-\xi)}{\hat{G}}+1\right)-\sigma_{rz}^2\left(\frac{(1-\xi)}{\hat{G}}\right)^2} + \left(\frac{1}{\sigma_{\theta\theta}\frac{(1-\xi)}{\hat{G}}+1}\right), \tag{A.56}$$

which simplifies to

$$
tr(\boldsymbol{b}^{-1}) = \frac{(\sigma_{zz}+\sigma_{rr})\frac{2\hat{G}}{(1-\xi)}}{\left(\sigma_{rr}\sigma_{zz}\frac{(1-\xi)}{\hat{G}}+\sigma_{rr}+\sigma_{zz}+\frac{(1-\xi)}{\hat{G}}\right)-\sigma_{rz}^{2}\left(\frac{(1-\xi)}{\hat{G}}\right)} + \left(\frac{1}{\sigma_{\theta\theta}\frac{(1-\xi)}{\hat{G}}+1}\right). \tag{A.57}
$$

Substituting Eqs. (A.51), (A.52), (A.54) and (A.57) into Eq. (A.50) leads to,

$$
\begin{aligned}
Q_D = \mu(\theta)(1-\beta)\left(2\frac{u^2}{r^2}+\left(\frac{\partial w}{\partial r}\right)^2\right) - \gamma\frac{u}{r}(\sigma_{rr}-\sigma_{\theta\theta}) \\
+2\gamma\sigma_{rz}\frac{\partial w}{\partial r} + (1-\gamma)\frac{\hat{G}}{2\chi(1-\xi)^2 Wi\lambda(\theta)}\Psi,
\end{aligned} \tag{A.58}
$$

where

$$
\begin{aligned}
\Psi = (\sigma_{rr}+\sigma_{\theta\theta}+\sigma_{zz})\frac{(1-\xi)}{\hat{G}} + \left(\frac{1}{\sigma_{\theta\theta}\frac{(1-\xi)}{\hat{G}}+1}\right) \\
+\frac{(\sigma_{zz}+\sigma_{rr})\frac{2\hat{G}}{(1-\xi)}}{\left(\sigma_{rr}\sigma_{zz}\frac{(1-\xi)}{\hat{G}}+\sigma_{rr}+\sigma_{zz}+\frac{(1-\xi)}{\hat{G}}\right)-\sigma_{rz}^{2}\left(\frac{(1-\xi)}{\hat{G}}\right)} - 3.
\end{aligned} \tag{A.59}
$$

A.12 Dimensionless wall slip conditions

The slip model in [48] reads,

$$
w'_s + \lambda_s\frac{dw'_s}{dt'} = a\sigma'^{m}_{w}, \tag{A.60}
$$

where a is the slip coefficient, w'_s is the slip velocity λ'_s is the slip relaxation time, σ'^{m}_{w} is the wall shear stress and $m \in \{2,4,6\}$ is the power law exponent. Using the dimensionless variables defined in chapter 3 and setting $a = \alpha'_2\eta_p$, where η_p is the polymer viscosity and ${\alpha'}_2$ is similar to the dimensionless slip parameter of [80] and related to the coefficient of dynamics friction (k^*) by ${\alpha'}_2 = \frac{1}{k^*}$, we obtain

$$Uw_s + \chi\alpha_1\lambda(\theta)U\frac{\lambda_r U}{R_o}\frac{dw_s}{dt} = {\alpha'}_2\frac{U^m\eta_r^m\chi^m}{R_o^m}\eta_r\beta\mu(\theta)\sigma_w^m, \tag{A.61}$$

which reduces to,

$$w_s + \chi\alpha_1 Wi\lambda(\theta)\frac{dw_s}{dt} = \chi^m{\alpha'}_2\frac{U^{m-1}\eta_r^{m+1}\chi^m}{R_o}\beta\mu(\theta){\sigma_w}^m. \tag{A.62}$$

On setting,

$${\alpha'}_2 = \frac{R_o^m}{U^{m-1}\eta_r^{m+1}}\alpha_2, \tag{A.63}$$

we obtain

$$w_s + \chi\alpha_1 Wi\lambda(\theta)\frac{dw_s}{dt} = \chi^m\alpha_2\beta\mu(\theta){\sigma_w}^m. \tag{A.64}$$

Rearranging Eq. (A.64), we obtain

$$\frac{dw_s}{dt} + \frac{1}{\chi\alpha_1 Wi\lambda(\theta)}w_s = \frac{\chi^{m-1}\alpha_2\beta\mu(\theta)}{\alpha_1 Wi\lambda(\theta)}{\sigma_w}^m. \tag{A.65}$$

It follows from Eq. (A.65) that,

$$w_s = \left(1 - \exp\left(\frac{-t}{\chi\alpha_1 Wi\lambda(\theta)}\right)\right)\chi^m\alpha_2\beta\mu(\theta)\sigma_w^m. \tag{A.66}$$

A.13 Numerical Algorithm: Semi Implicit Finite Difference Techniques

The governing equations in cylindrical coordinates are discretized with semi-implicit finite difference schemes similar to the well know finite difference θ schemes. As an example, consider a smooth function W satisfying a one dimensional autonomous Partial Differential Equation (PDE) of the form

$$\frac{\partial W}{\partial t} = a(x)\frac{\partial^2 W}{\partial x^2} + b(W,x)\frac{\partial W}{\partial x} + c(W,x)W + \mathrm{F}, \tag{A.67}$$

subject to the conditions

$$W(0,x) = W_0, \tag{A.68}$$

$$\frac{\partial W}{\partial x}(x_0,t) = \alpha_0 \quad \text{and} \quad W(x_m,t) = \alpha_m. \tag{A.69}$$

In solving the parabolic PDE given by Eq. (A.67), we decompose the given domain based on a linear Cartesian mesh and uniform grid of size h, on which finite-differences are taken. We construct finite difference approximations for Eq.(A.67) in the form

$$\frac{W_i^{n+1} - W_i^n}{k} = a\left(\frac{\partial^2 W}{\partial x^2}\right)^{n+\zeta^*} + \left[b(W,x)\frac{\partial W}{\partial x}\right]^n + [c(W,x)W]^n + \mathrm{F}^n, \tag{A.70}$$

where k is the time change (Δt), and n represents the current time step. Here, the temporal derivative is approximated via the discrete Euler forward difference scheme, while spatial derivatives are discretized with second order central differences. We make allowance for a Crank-Nicolson type scheme such that implicit terms are taken at intermediate time level (n + ζ^*), $0 \leq \zeta^* \leq 1$. Observe that in the case where $\zeta^* = 0$, all terms in the RHS of Eq. (A.70) are explicitly discretized. In this study, we use $\zeta^* = 1$ so that we can use larger time steps and still converge to steady state solutions. Furthermore, the term $\#^{n+\zeta^*}$ in Eq.(A.70) is written as a convex combination of $\#$ so that,

$$\#^{n+\zeta^*} = \zeta^* \# + (1-\zeta^*)\#. \tag{A.71}$$

Eq. (A.70) therefore becomes,

$$\begin{aligned} W_i^{n+1} - W_i^n \;=\; & \frac{ak\zeta^*}{h^2}\left(W_{i+1}^{n+1} - 2W_i^{n+1} + W_{i-1}^{n+1}\right) \\ & + \frac{ak(1-\zeta^*)}{h^2}\left(W_{i+1}^{n} - 2W_i^{n} + W_{i-1}^{n}\right) \\ & + \frac{kb(W,x)_i^n}{2h}\left(W_{i+1}^{n} - W_{i-1}^{n}\right) \\ & + kc(W,x)_i^n W_i^n + k\mathrm{F}_i^n, \end{aligned} \tag{A.72}$$

which simplifies to

$$\begin{aligned} -\Gamma_1 W_{i+1}^{n+1} + (1+2\Gamma_1)W_i^{n+1} - \Gamma_1 W_{i-1}^{n+1} = & \left(\Gamma_2 + \frac{b(W,x)_i^n}{2h}\right) W_{i+1}^n \\ & + \left(1 - 2\Gamma_2 + c(W,x)_i^n\right) W_i^n \\ & + \left(\Gamma_2 - \frac{b(W,x)_i^n}{2h}\right) W_{i-1}^n + \mathrm{F}_i^n, \end{aligned} \tag{A.73}$$

where $\Gamma_1 = \frac{ak\zeta^*}{h^2}$ and $\Gamma_2 = \frac{ak(1-\zeta^*)}{h^2}$. The emerging systems of algebraic equations (Eq.(A.73)) can be rearranged to obtain,

$$\boldsymbol{A}\boldsymbol{W}^{n+1} = \boldsymbol{B}\boldsymbol{W}^n + k\boldsymbol{F}^n, \tag{A.74}$$

with sparse matrices $\boldsymbol{A}$ and $\boldsymbol{B}$. The matrix $\boldsymbol{A}$ in fact is tridiagonal and corresponds to the coefficients of the unknowns at the future ($(n+1)^{th}$) time step, $\boldsymbol{B}$ is the matrix coefficients of the known values of $\boldsymbol{W}$ at the present time n and $\boldsymbol{F}$ is the source term at n.

The equations corresponding to the boundary nodes are necessarily modified to reflect the contributions of the boundary conditions, thus, the matrices $\boldsymbol{A}$ and $\boldsymbol{B}$ are adjusted to include these contributions. In other to avoid the use of ghost nodes at the Neumann boundaries, we construct one sided higher order difference schemes for the derivatives at the boundary. Now suppose W is continuously differentiable and defined on the given domain, then by [78], it is possible to construct alternative finite difference stencils for the first derivative approximations involving either three interior nodes,

$$W'(x)^{+} \approx \frac{1}{6h}\left[2W(x+3h) - 9W(x+2h) + 18W(x+h) - 11W(x)\right], \tag{A.75}$$

and

$$W'(x)^{-} \approx \frac{1}{6h}\left[11W(x) - 18W(x-h) + 9W(x-2h) - 2W(x-3h)\right], \tag{A.76}$$

or two interior nodes,

$$W'(x)^{+} \approx \frac{1}{2h}\left[-3W(x) + 4W(x+h) - W(x+2h)\right], \tag{A.77}$$

$$W'(x)^{-} \approx \frac{1}{2h}\left[3W(x) - 4W(x-h) + W(x-2h)\right], \tag{A.78}$$

where $()^{+}$ and $()^{-}$ indicate forward and backward difference respectively, (see appendix A.14 for details). This idea has been successfully implemented in [57] for example.

The values of $\boldsymbol{W}$ are therefore estimated at every time step $(t + nk)$, via Gauss elimination,

$$\boldsymbol{W}^{n+1} = \boldsymbol{A}^{-1}\boldsymbol{B}\boldsymbol{W}^{n} + k\boldsymbol{A}^{-1}\boldsymbol{F}^{n}. \tag{A.79}$$

This technique has been successfully utilized to investigate various fluid flow problems in literature [25, 20, 21, 22, 23, 24]. For computational efficiency in practice, we do not actually compute the inverse matrices but rather use, LU decompositions, Gauss elimination etc. We follow this approach and discretize the coupled system of equations governing the flow under consideration. These equations are solved systematically at every time step until, say, steady state solutions are reached.

A.14 Neumann Boundaries

In order to avoid the use of ghost nodes, we explore alternative finite difference discretization (with controllable accuracy). Let f be a continuously differentiable function defined on a given interval $x_0 < x < x_1, \{x_0, x_1 \in \mathbb{R}\}$, then by Taylor series approximations, $f(x \pm sh)$ $\{s \in \mathbb{R}^+\}$, in series form is

$$f(x \pm sh) = f(x) + \sum_{m=1}^{n} (\pm 1)^m \frac{(sh)^m}{m!} f^{(m)}(x) + O(h^{n+1}). \tag{A.80}$$

We have,

$$f(x + h) = f(x) + \sum_{m=1}^{3} \frac{(h)^m}{m!} f^{(m)}(x) + O(h^4), \tag{A.81}$$

$$f(x - h) = f(x) + \sum_{m=1}^{3} (-1)^m \frac{(h)^m}{m!} f^{(m)}(x) + O(h^4), \tag{A.82}$$

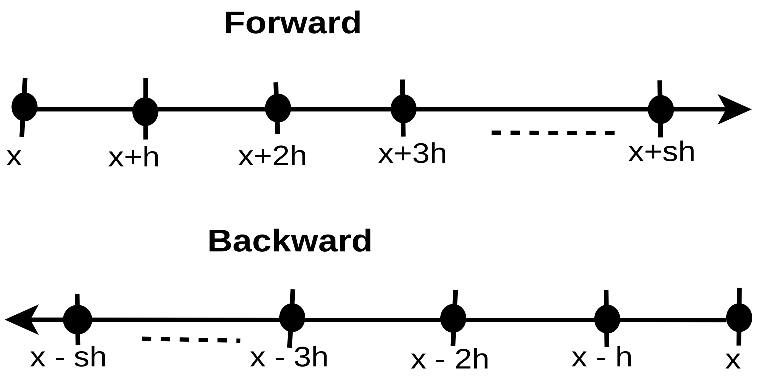

Figure A.1: Forward and backward difference mesh for a linear domain

$$f(x+2h) = f(x) + \sum_{m=1}^{3} \frac{(2h)^m}{m!} f^{(m)}(x) + O(h^4), \tag{A.83}$$

$$f(x-2h) = f(x) + \sum_{m=1}^{3} (-1)^m \frac{(2h)^m}{m!} f^{(m)}(x) + O(h^4), \tag{A.84}$$

$$f(x+3h) = f(x) + \sum_{m=1}^{3} \frac{(3h)^m}{m!} f^{(m)}(x) + O(h^4), \tag{A.85}$$

and

$$f(x-3h) = f(x) + \sum_{m=1}^{3} (-1)^m \frac{(3h)^m}{m!} f^{(m)}(x) + O(h^4). \tag{A.86}$$

Multiplying equations (A.81), (A.83), (A.86) by α_1, α_2 and α_3 respectively, leads to

$$\alpha_1 f(x+h) - \alpha_1 f(x) = \alpha_1 \sum_{m=1}^{3} \frac{(h)^m}{m!} f^{(m)}(x) + O(h^4), \tag{A.87}$$

$$\alpha_2 f(x+2h) - \alpha_2 f(x) = \alpha_2 \sum_{m=1}^{3} \frac{(2h)^m}{m!} f^{(m)}(x) + O(h^4), \tag{A.88}$$

and

$$\alpha_3 f(x+3h) - \alpha_3 f(x) = \alpha_2 \sum_{m=1}^{3} \frac{(3h)^m}{m!} f^{(m)}(x) + O(h^4). \tag{A.89}$$

Adding equations (A.87), (A.88) and (A.89), gives

$$\sum_{s=1}^{3} \alpha_s f(x+sh) - f(x) \sum_{s=1}^{3} \alpha_s = \sum_{m=1}^{3} \sum_{s=1}^{3} \alpha_s s^m \frac{(h)^m}{m!} f^{(m)}(x) + O(h^4). \tag{A.90}$$

Setting,

$$m!\beta_m = \sum_{s=1}^{3} \alpha_s s^m, \tag{A.91}$$

then Eq. (A.90) becomes,

$$\sum_{s=1}^{3} \alpha_s f(x+sh) - f(x) \sum_{s=1}^{3} \alpha_s = \sum_{m=1}^{3} \beta_m h^m f^{(m)}(x) + O(h^4). \tag{A.92}$$

To obtain the approximation for the first derivative, set $\beta_1 = 1, \beta_2 = \beta_3 = 0$. This yields a system of algebraic equations

$$\begin{aligned} &\alpha_1 + 2\alpha_2 + 3\alpha_3 = 1, \\ &\alpha_1 + 4\alpha_2 + 9\alpha_3 = 0, \\ &\alpha_1 + 8\alpha_2 + 27\alpha_3 = 0. \end{aligned} \tag{A.93}$$

The resulting values are therefore

$$\alpha_1 = 3, \quad \alpha_2 = -\frac{3}{2}, \ \alpha_3 = \frac{1}{3}.$$

It then follows that an alternative stencil for the forward difference approximation (involving three interior nodes) of the first derivative is,

$$f'(x) \approx \frac{1}{6h}\left[2f(x+3h) - 9f(x+2h) + 18f(x+h) - 11f(x)\right]. \tag{A.94}$$

Following a similar argument, the backward difference approximation is,

$$f'(x) \approx \frac{1}{6h}\left[11f(x) - 18f(x-h) + 9f(x-2h) - 2f(x-3h)\right]. \tag{A.95}$$

Suppose it is required that only two interior nodes are involved in the approximation, then following the same arguments, the forward and backward difference approximations are

$$f'(x) \approx \frac{1}{2h}\left[-3f(x) + 4f(x+h) - f(x+2h)\right], \tag{A.96}$$

and

$$f'(x) \approx \frac{1}{2h}\left[3f(x) - 4f(x-h) + f(x-2h)\right], \tag{A.97}$$

respectively.

A.15 Boundaries in terms of χ: Annular flow problem

The two concentric pipes are such that the inner radius is R_i and outer radius is R_o, $\zeta = R_o - R_i$ and $k = \frac{R_o}{R_i} > 1$. Recall that $\zeta = R_o/\chi$, and the scaling of the radius r' is such that

$$r = \frac{r'}{\zeta}. \tag{A.98}$$

At $r' = R_i$ we have,

$$r = \frac{R_i}{\zeta}; \quad \text{but} \quad \zeta = R_o/\chi \quad \text{and} \quad \chi = \frac{k}{k-1}, \tag{A.99}$$

hence at $r' = R_i$

$$r = \frac{R_i \chi}{R_o} = \frac{\chi}{k}. \tag{A.100}$$

Since

$$k = \frac{\chi - 1}{\chi}, \tag{A.101}$$

then

$$r = \chi - 1 \quad \text{at} \quad r' = R_i. \tag{A.102}$$

Similarly, at $r' = R_o$, we have

$$r = \frac{R_o}{\zeta} = \chi. \tag{A.103}$$

A.16 Picard linearization Technique

Given the nonlinear PDE Eq.(A.104) subject to the conditions (A.105) and(A.106), it is possible to linearize the equation iteratively via the Picard linearization technique. This means that at every time step n we solve the time discrete equation (A.107) iteratively to obtain the approximate numerical solution to the PDE,

$$\frac{\partial u}{\partial t} + \nabla \cdot (uu) = \nabla \cdot (\alpha(u) \nabla u) + f(u), \quad \boldsymbol{x} \in \Gamma, \quad t \in (0, T] \tag{A.104}$$

$$-\alpha(u) \frac{\partial u}{\partial n} = g, \quad \boldsymbol{x} \in \partial\Gamma_N, \quad t \in (0, T], \tag{A.105}$$

$$u = u_0, \quad \boldsymbol{x} \in \partial\Gamma_D, \; t \in (0, T]\,. \tag{A.106}$$

If we employ the backward Euler method to the time derivative term on the LHS of Eq. A.104, we obtain

$$\frac{u^n - u^{n-1}}{\Delta t} = -\nabla \cdot (u^n u^n) + \nabla \cdot (\alpha(u^n)\nabla u^n) + f(u^n), \tag{A.107}$$

which generates a non linear system of algebraic equations in u^n. By using the Picard Linearization technique with i iteration counter, the terms $\nabla \cdot (u^n u^n)$ and $\nabla \cdot \alpha(u^n)\nabla u^n$ are linearized in terms of the i^{th} and $(i+1)^{th}$ iteration. So that the previously computed $u^{n,i}$ approximates the diffusion term $\alpha(\boldsymbol{u}^{n,i})$ as well as one of the $\boldsymbol{u}$'s in the convective. The nonlinear source term is also treated in a similar manner i.e. $f(u^{n,i})$. Hence in discrete form, the nonlinear PDE becomes in linear form

$$\frac{u^{n,k+1} - u^{n-1}}{\Delta t} = -\nabla \cdot (u^{n,i} u^{n+i}) + \nabla \cdot (\alpha(u^{n,i})\nabla u^{n,i+1}) + f(u^{n,i})\,. \tag{A.108}$$

The initial guess for the iteration at the current time level is therefore the solution at the previous time step, i.e. $u^{n,0} = u^{n-1}$. The iterative process is set to stop as the values of u converges; $||u^{n,i+1} - u^{n,i}|| \to 0$ as $i \to \infty$.

A.17 Summary of the Chorin algorithm

Consider the equations for conservation of momentum and mass,

$$\frac{\partial \rho \boldsymbol{v}}{\partial t} + \nabla \cdot (\rho \boldsymbol{v}\boldsymbol{v}) = \nabla \ \cdot \ \boldsymbol{\tau} - \nabla P + \rho \boldsymbol{g}, \tag{A.109}$$

$$\nabla \cdot \boldsymbol{v} = S_p. \tag{A.110}$$

To implement the Chorin Algorithm, we first solve the momentum equation (for an auxiliary velocity $\boldsymbol{v}^*$) using the values of pressure from previous time step n, so that the time discretization takes the form

$$\frac{(\rho \boldsymbol{v})^* - (\rho \boldsymbol{v})^n}{dt} = -\nabla p^n + F. \tag{A.111}$$

Here $F = -\nabla \cdot (\boldsymbol{v} \rho \boldsymbol{v}) + \nabla \cdot \boldsymbol{\sigma} + \rho \boldsymbol{g}$, Eq. A.111 can be solved explicitly for $\boldsymbol{v}^*$. However, $\boldsymbol{v}^*$ does not necessarily have to satisfy the continuity equation Eq.A.110. Similarly, we can write the solutions at the $(n+1)^{th}$ term as

$$\frac{(\rho \boldsymbol{v})^{n+1} - (\rho \boldsymbol{v})^n}{dt} = -\nabla p^{n+1} + F, \tag{A.112}$$

so that combining Eqs. (A.111) and (A.112), we obtain

$$\frac{(\rho \boldsymbol{v})^{n+1} - (\rho \boldsymbol{v})^*}{dt} = -\nabla (p^{n+1} - p^n) = -\nabla (p'). \tag{A.113}$$

Taking the divergence of Eq. (A.113) yields,

$$\nabla \cdot (\rho \boldsymbol{v})^{n+1} - \nabla \cdot (\rho \boldsymbol{v})^* = -dt \Delta p', \tag{A.114}$$

where $\Delta = \nabla \cdot \nabla$ and $\boldsymbol{v}^{n+1}$ satisfies the continuity equation (A.110), i.e.

$$\nabla \cdot \boldsymbol{v}^{n+1} = S_p. \tag{A.115}$$

Since S_p is known at every time step, then Eq. (A.114) is solved for p' and the value is used to correct the velocity at the $(n+1)^{th}$ time step,

$$\boldsymbol{v}^{n+1} = \boldsymbol{v}^* - dt \nabla p'. \tag{A.116}$$

The pressure is then corrected by

$$p^{n+1} = p^n + p'. \tag{A.117}$$

Bibliography

Bibliography

[1] J. Adler. Thermal explosion theory for reactive flow between parallel heated walls. *Combustion and Flame 24:151-158.*, 1975.

[2] G. F. Arnold and R. B. Bird. Non- newtonian flow in annuli. *Industrial and Engineering Chemistry. 50(3):347-352.*, 1958.

[3] K. Ashida. *Polyurethane and Related Foams: Chemistry and Technology.* CRC Press Taylor & Francis Group, 6000 Broken Sound Parkway NW, Suite 300 Boca Raton, FL 334872742, 2007.

[4] H. Azzouzi, J.P. Decruppe, S. Lerouge, and O. Greffier. Temporal oscillations of shear stress and scattered light in a shear-banding-shear-thickening micellar solution. *Eur. Phys. J E17,507-514.*, E17:507–514, 2005.

[5] S. Bair and F. Qureshi. The generalized newtonian fluid model and elastohydrodynamic film thickness. *Transactions of the ASME*, 125:70–75, 2003.

[6] H. A. Barnes, J. F. Hutton., and K. Walters. *An Introduction to Rheology.* Elsevier Science Publishers B.V. Sara Burgerhartstraat 25, P.O. Box 21 1,1000 AE Amsterdam, The Netherlands, 1989.

[7] S. A. BASER and D. V. Khakhar. Modelling of the dynamics of water and r-11 blown polyurethane foam formation. *Polymer Engineering and Science, 34 (8):643 - 649.*, 1994.

[8] L. Becu, P. Grondin, A. Colin, and S. Manneville. How does a concentrated emulsion flow? yielding, local rheology, and wall slip. *Colloid Surf A-Physicochem Eng Asp 263:146-152.*, 2005.

[9] J. Bikard, J. Bruchon, T. Coupez, and L. Silva. Numerical simulation of 3d polyurethane expansion during manufacturing process. *Colloids and Surfaces A: Physiochem Eng. Aspect, 309:49-63.*, 2007.

[10] J. Bikard, J. Bruchon, T. Coupez, and B. Vergnes. Numerical prediction of the foam structure of polymeric materials by 3d simulation of their expansion by chemical reaction based on multidomain method. *Mechanical Behaviour of Cellular Solids: Journal of Materials Science, 40: 5875 - 5881.*, 2005.

[11] R. B. Bird, R.C. Armstrong, and O. Hassager. *Dynamics of polymeric liquids: Fluid Mechanics, Vol. 1.* Wiley, New York., 1977.

[12] T. Boddington, C.G. Feng, and P. Gray. Thermal explosion and the theory of its initiation by intense light. 1983.

[13] P. E. Boukany, P. Tapadia, and S.Q. Wang. Interfacial stick-slip transition in simple shear of entangled melts. *J Rheol 50: 641 - 654.*, 2006.

[14] P. E. Boukany and S.Q. Wang. Exploring the transition from wall slip to bulk shearing banding in well-entangled dna solutions. *Soft Matter 5:780 - 789.*, 2009.

[15] E. Broyer, C. W. Macosko, F. E. Critchfield, and L. F. Lawler. Curing and heat transfer in polyurethane reaction molding. *Polymer Engineering and Science, 18 (5):382 - 387.*, 1978.

[16] J. Bruchon and T. Coupez. A numerical strategy for the direct 3d simulation of the expansion of bubbles into a molten polymer during a foaming process. *Int. Journal for Numerical Methods in Fluids, 57:977-1003.*, 2008.

[17] B. R. Byron., A. C. Robert, and . H. Ole. *Dynamics of Polymeric Liquids*, volume Vol 1. John Wiley & Sons, Inc., second edition, 1987.

[18] J. M. Castro and C. W. Macosko. Studies of mold filling and curing in the reaction injection molding process. *AIChE Journal, 28(2):250-260.*, 1982.

[19] T. Chinyoka. Poisueille flow of a reactive phan-thien-tanner liquids in one dimension. *ASME Journal of Heat Transfer 132(11):1-7.*

[20] T. Chinyoka. Computational dynamics of a thermally decomposed viscoelastic lubricant under shear. *ASME Journal of Fluids Engineering. 130(12):1-7.*, 2008.

[21] T. Chinyoka. Modeling of cross-flow heat exchangers with viscoelastic fluids. *Nonlinear Analysis; Real world Applications 10:3353-3359.*, 2009.

[22] T. Chinyoka. Viscoelastic effects in double-pipe single-pass counterflow heat exchangers. *International Journal of Numerical Meth. Fluids 59:677-690.*, 2009.

[23] T. Chinyoka. Suction and injection control of shear banding in non-isothermal and exothermic channel flow of johnson-segalman liquids. *ASME Journal of Fluids Engineering 133:1-12.*, 2011.

[24] T. Chinyoka. Two-dimensional flow flow of chemically reactive viscoelastic fluids with or without the influence of thermal convection. *Communications in nonlinear Science and Numerical Simulation 16:1387-1395.*, 2011.

[25] T. Chinyoka and O.D. Makinde. On transient flow of a reactive variable viscosity third-grade fluid through a cylindrical pipe with convective cooling. *Meccanica*, 47:667–685, 2012.

[26] A. J. Chorin. Numerical solution of the navier-stokes equations. *Math. Comp. 22: 745762.*, 1968.

[27] M. Cromer, L. P. Cook, and G. H. McKinley. Interfacial instability of pressure-driven channel flow for a two-species model of entangled wormlike micellar solutions. *Journal of Non-Newtonian Fluid Mechanics, 166: 566-577.*, 2011.

[28] M. Cromer, L. P. Cook, and G. H. McKinley. Pressure-driven flow of wormlike micellar solutions in rectilinear microchannels. *J. non-Newtonian Fluid Mechanics,166:180-193.*, 2011.

[29] M. Cromer, M. C. Villet, G. H. Fredrickson, and L. G. Leal. Shear banding in polymer solutions. *Phys. Fluids, 25: 051703.*, 2013.

[30] M. M. Denn. Extrusion instabilities and wall slip, annu. rev. *Fluid Mech. 33:26587.*, 2001.

[31] J. D. Domine and C. G. Gogos. Simulations of reactive injection molding. *Polymer Engineering and Science, 20 (13):847 - 858.*, 1980.

[32] P. A. Drda and S.Q. Wang. Stickslip transition at polymer melt/solid interfaces. *Physical Review Letters; 75:26982701.*, 1995.

[33] M. Dressler, B.J. Edwards, and H.C. Öttinger. Macroscopic thermodynamics of flowing polymeric liquids. *Rheol. Acta, 38:117-136.*, 38:117–136, 1999.

[34] D. Eaves. *Handbook of Polymer Foams.* Rapra Technology Limited Shawbury, Shrewsbury, Shropshire, SY4 4NR, UK, 2004.

[35] P. Espanol, X.F. Yuan, and R.C. Ball. Shear banding flow in the johnson-segalman fluid. *Journal of Non-Newtonian Fluid Mech. 65:93-109.*, 1996.

[36] M. A. Fardin, T. J. Ober, V. Grenard, T. Divoux, S. Manneville, G. H. McKinley, and S. Lerouge. Interplay between elastic instabilities and shear-banding: three categories of taylorcouette flows and beyond. *Soft Matter, 8:10072.*, 2012.

[37] T. P. Fernando and P. J. Oliviera. Axial annular flow of non-linear viscoelastic fluid - an analytical solution. *J. Non-Newtonian fluid Mechanics. 93:325 - 337.*, 2000.

[38] M. S. Fielding and J.H. Wilson. Shear banding and interfacial instability in planar poiseuille flow. *Journal of Non-Newtonian Fluid Mech, 165:192-201*, 2010.

[39] S. M. Fielding. Complex dynamics of shear banded flows. *Soft Matter 3:1262-1279.*, 2007.

[40] S. M. Fielding and P.D. Olmsted. Kinetics of the shear banding instability in startup flows. *Phys Rev E*, 68::036313, 2003.

[41] P. Fischer, E. K. Wheeler, and G.G. Fuller. Shear-banding structure orientated in the vorticity direction observed for equimolar micellar solution. *Rheol Acta 41:35 - 44.*, 2002.

[42] D. A. Frank-Kamanetskii. *Diffussion and heat transfer in Chemical Kinetics.* Plenum Press, New York, 1969.

[43] M. M. Fyrillas, G.C. Georgiou, and D. Vlassopoulos. Time-dependent plane poiseuille flow of a johnson-segalman fluid. *Journal of Non-Newtonian Fluid Mech. 82:105-123.*, 1999.

[44] C. G. Georgiou. On the stability of the shear flow of viscoelastic fluid with slip along the fixed wall. *Rheol Acta 47:33-39.*, 1996.

[45] H. Giesekus. A simple constitutive equation for polymer fluids based on the concept of deformation-dependent tensorial mobility. *Journal 0f Non-Newtonian Fluid Mechanics, 11: 69- 109.*, 1982.

[46] P. J. Halley and M. E. Mackay. Chemorheology of thermosets-an overview. *Polymer Engineering and Science, 36 (5): 593-609.*, 1996.

[47] S. G. Hatzikiriakos. Appropriate boundary condition in the flow of molten polymers. *International Polymer Processing,25:5562.*, 2010.

[48] S. G. Hatzikiriakos. Wall slip of molten polymers. *Progress in Polymer Science,37:624 643.*, 2012.

[49] S. G. Hatzikiriakos and J.M. Dealy. Wall slip of molten high density polyethylene. ii. capillary rheometer studies. *J Rheo, 36:70341.*, 1992.

[50] S. G. Hatzikiriakos, C. Stewart, and J.M. Dealy. Effect of surface coatings on wall slip of lldpe. *Intern Polymer Processing, 8:305.*, 1993.

[51] S.G. Hatzikiriakos and K.B. Migler, editors. *Polymer Processing Instabilities Control and Understanding.* Marcel Dekker, New York., 2005.

[52] C. Heese, W.Breit, F.Schuler, D. Niedziela, and A. Latz. Simulation of the flow and form filling behavior of uhpc with fibers. pages 535–538, 2012.

[53] M. E. Helgeson, M. D. Reichert, Y. Thomas Hu, and N. J. Wagner. Relating shear banding, structure, and phase behavior in wormlike micellar solutions. *Soft Matter, 5: 38583869.*, 2009.

[54] M. Hütter, Luap C., and Öttinger H.C. Energy elastic effects and the concept of temperature in flowing polymeric liquids. *Rheol Acta 48:301 - 316.*, 2009.

[55] I. E. Ireka and T. Chinyoka. Non - isothermal flow of a johnson - segalman liquid in a lubricated pipe with wall slip. *J. Non-Netonian Fluid Mechanics*, 192:20–28, 2013.

[56] I. E. Ireka and T. Chinyoka. Analysis of shear banding phenomena in non-isothermal flow of fluids governed by the diffusive johnson-segalman model. *Applied Mathematics Modelling*, Currently under review, 2014.

[57] I. E. Ireka, Wakeni M.F., and Alireza Baghai-Wadji. A novel ab-initio finite difference-based method for convenient implementation of the mass-loading effect in microacoustic devices. volume 10.1109/ULTSYM.2014.0368, pages 1488–1491. IEEE International Ultrasonics Symposium, 2014.

[58] I. E. Ireka, D. Niedziela, K. Schäfer, J. Tröltzsch, K. Steiner, F. Helbig, T. Chinyoka, and L. Kroll. Computational modelling of the complex dynamics of chemically blown polyurethane foam. *Macromolecular Theory and Simulations*, Currently under review, 2015.

[59] M. Johnson and D. Segalman. A model for viscoelastic fluid behavior which allows non-affine deformation. *J Non-Newton Fluid Mech 2:255-270.*, 1977.

[60] D. D. Joseph and Y. Renardy. *Fundamentals of Two-Fluid Dynamics. Part 2: Lubricated Transport, Drops and Miscible Liquids.* Springer Verlag New York., 1993.

[61] Y. M. Joshi, K.L. Ashish, and R.A. Mashelkar. A unified wall slip model. *Journal of Non-Newtonian Fluid Mech. 94:135-149.*, 2000.

[62] Y. M. Joshi, P.S. Tapadia, A.K. Lele, and R.A. Mashelkar. Temperature dependence of critical stress for wall slip by debonding. *Journal of Non-Newtonian Fluid Mech. 94:151157.*, 2000.

[63] D. S. Kalika and M.M. Denn. Wall slip and extrudate distortion in linear low-density polyethylene. *Journal of Rheology 31:815.*, 1087.

[64] M. R. Kamal. Thermoset characterization for modality analysis. *Polymer Engineering and Science, 14 (3): 231-239.*, 1974.

[65] M. R. Kamal and M. E. Ryan. Reactive polymer processing: Techniques and trends. *Advances in Polymer Technology, 4(3-4):323348.*

[66] R. W. Kolkka, D.S. Malkus, M.G. Hansen, G.R. Ierley, and R.A. Worthing. Spurt phenomena of the johnson-segalman fluid and related models. *Journal of Non-Newtonian Mech. 29:303-335.*, 1988.

[67] R. G. Larson. Instabilities in viscoelastic flows. *Rheologica Acta, 31(3):213-263.*, 1992.

[68] A. Latz, U. Strautins, and D. Niedziela. Comparative numerical study of two concentrated fiber suspension modles. *Journal of Non-Newtonian Fluid Mechanics, Vol. 165,Issues 13-14, pp. 764-781.*, 2010.

[69] S.T. Lee and N.S. Ramesh. *POLYMERIC FOAMS Mechanisms and Materials.* CRC Press LLC, 2000 N.W. Corporate Blvd., Boca Raton, Florida 33431, 2004.

[70] L. Lefebvre and R. Keunings. Finite element modelling of the flow of chemically reactive polymeric liquids. *Int. Journal for Numerical Methods in Fluids, 20:319-334.*, 1995.

[71] A. E. Likhtman and R. S. Graham. Simple constitutive equation for linear polymer melts derived from molecular theory: Roliepoly equation. *J. Non-Newtonian Fluid Mech., 114: 112.*, 2003.

[72] C.Y.U. Lu, P.D. Olmsted, and R.C Ball. Effects of non-local stress on the determination of of shear banding flow. *Phy. Rev. Lett. 84:642-645.*, 2000.

[73] S. Manneville, A. Colin, G. Waton, and F. Schosseler. Wall slip, shear banding, and instability in the flow of a triblock copolymer micellar solution. *Phys Rev E 75:061502.*, 2007.

[74] M. F. Marios, C.G. Georgiou, and V. Dimitris. Time-dependent plane poiseuille flow of a johnson-segalman fluid. *Journal of Non-Newtonian Fluid Mech. :*, 82:105–123, 1999.

[75] C. Masselon, A. Colin, and P.D. Olmsted. Influence of boundary conditions and confinement on nonlocal effects in flows of wormlike micellar systems. *Physics review letters E 81:021502-15.*, 2010.

[76] T.C.B. McLeish and R.C. Ball. A molecular approach to the spurt effect in polymer melt flow. *Journal of Polymer Science B24:1735-1745.*, 1986.

[77] V. Mhetar and L. A. Archer. Slip in entangled polymer melts. 1. general features. *Macromolecules , 31: 8607-8616.*, 1998.

[78] A. R. Mitchell and D. F. Griffiths. *The finite difference method in partial differential equations.* Chichester Eng. : New York Wiley, 1980.

[79] E. Mitsoulis. Flows of viscoplastic materials: Models and computations. *Rheology Reviews (British Society of Rheology)*, pages 135 – 178, 2007.

[80] E. Mitsoulis and S. G. Hatzikiriakos. Tubing extrusion of a flouropolymer melt. *International journal of Polymer Processing*, 2:259–269, 2012.

[81] M. M. Mohseni and F. Rashidi. Short communication: Viscoelastic fluid behavior in annulus using giesekus model. *J. Non-Newtonian Fluid Mech, 165:15501553.*, 2010.

[82] R. L. Moorcroft and S.M.Fielding. Criteria for shear banding in time-dependent flows of complex fluids. *arXiv:1201.6259v1 [cond-mat.soft] 30 Jan 2012.*, 2012.

[83] M. Mostafaiyan, K. Khodabandehlou, and F. Sharif. Analysis of a viscoelastic fluid in an annulus using giesekus model. *J. Non-Newtonian Fluid Mech. 118:4955.*, 2004.

[84] S. Muzaferija and M.Peric. *Computation of free surface flows using interface-tracking and interface-capturing methods. In Nonlinear Water Wave Interaction.*, chapter 2, pages 59–100. IT Press Southampton., 1999.

[85] D. Niedziela, J.Tröltzsch, A.Latz, and L.Krol. On numerical simulation of injection moulding process with integrated textile fibre reinforcement. *Journal of Thermoplastic Composite Materials, 26 (1): 74-90.*, 2013.

[86] D. Niedziela, U. Strautins, V. Hosdez, A. Kech, and A. Latz. Improved multiscale fiber orientation modeling in injection molding of short fiber reinforced thermoplastics: Simulation and experiment. *The International Journal of Multiphysics.*, 2011.

[87] S. S. Okoya. On the transition for a generalized couette flow of a reactive third-grade fluid with viscous dissipation. *International Communications in Heat and Mass Transfer, 35:188-196.*, 2008.

[88] P. D. Olmsted. Perspectives on shear banding in complex fluids. *Rheo. Acta 47:283-300.*, 2008.

[89] R. G. Owens and T. N. Philips. *Computational Rheology.* Imperial College Press, 2002.

[90] D. S. W. Pau, C.M Fleischmann, M.J. Spearpoint, and K.Y. Li. Thermophysical properties of polyurethane foams and their melts. *Fire and Materials, DOI:10.1002/fam.2188.*, 2013.

[91] J. R. A. Pearson. Flow curves with a maximum. *Journal of Rheology 38:309331.*, 1994.

[92] G.W.M. Peters and F.P.T. Baaijens. Modelling of non-isothermal viscoelastic flows. *J. Non-Newton Fluid Mech. 68:205 - 224.*, 1997.

[93] A. V. Ramamurthy. Wall slip in viscous fluids and influence of materials of construction. *J. Rheology 30:337.*, 1986.

[94] I. J. Rao. Flow of a johnson - segalman fluid between rotating co-axial cylinders with and without suction. *Journal of Non-Linear Mechanics. 34:63-70.*, 1999.

[95] I. J. Rao and K.R. Rajagopal. Some simple flows of a johnson-segalman fluid. *Acta Mechanica Springer-Verlag 132:209-219.*, 1997.

[96] I. J. Rao and K.R. Rajagopal. The effect of the slip boundary condition on the flow of fluids in a channel. *Acta Mechanica Springer-Verlag 135:113-126.*, 1999.

[97] M. A. Rao. *Rheology of Fluid, Semisolid, and Solid Foods*, chapter 2, pages 27–36. Springer, Food Engineering Series, 2014.

[98] R. R. Rao, L. A. Mondy, D. R. Noble, H. K. Moffat, D. B. Adolf, and P. K. Notz. A level set method study of foam processing: a validation study. *International journal for Numerical Methods in Fluids, 68:1362-1392.*, 2011.

[99] M. T. Ravanchi, M. Mirzazadeh, and F. Rashidi. Flow of giesekus viscoelastic fluid in a concentric annulus with inner cylinder rotation. *International Journal of Heat and Fluid Flow, 28(4): 838-845.*, 2007.

[100] M. Renardy. *Mathematical analysis of Viscoelastic flows.* Society for Industrial and Applied Mathematics, Philadelphia, 2000.

[101] L. Z. Rogovina, V. G. Vasilev, and E. E. Braudo. Definition of the concept of polymer gel. *Polymer Science Series C, 50(1): 85 - 92.*, 2008.

[102] M. C. Saha, B. Barua, and S. Mohan. Study on the cure kinetic behavior of thermosetting polyurethane solids and foams: Effect of temperature, density, and carbon nanofiber. *Journal of Engineering Materials and Technology, 133: 0110153 -6.*, 2011.

[103] C. J. Seeton. Viscosity-temperature correlation for liquids. *Tribology Letters*, 22:67 – 78, 2006.

[104] D. Seo and J. R Youn. Numerical analysis on reaction injection molding of polyurethane foam by using finite volume method. *Polymer, 46:6482 - 6493.*, 2005.

[105] D. Seo, J. R. Youn, and C. L. Tucker III. Numerical simulation of mold filling in foam reaction injection molding. *International Journal of Numerical Methods in Fluids, 42:1105 -1134.*, 2003.

[106] J. C. Shang, K J. De Witt, and J. G. Fikioris. Annular couette flow of a sudden pressurized viscoelastic fluid. *Ind Eng. Chem Fundam., 12(1):31-33.*, 1973.

[107] A. V. Shenoy. *Rheology of Filled Polymer Systems.* Kluwer Academic Publishers, P.O. Box 17, 3300 AA Dordrecht, The Netherlands, 1999.

[108] N. A. Spenley, X.F. Yuan, and M.E. Cates. Nonmonotonic constitutive laws and the formation of shear banded flows. *J Phys II 6:551-571.*, 1996.

[109] R. I. Tanner and K. Walters. *Rheology: An Historic Perspective.* Elsevier Science Publishers, 1999.

[110] P. A. Vasquez, G. H. McKinley, and L. P. Cook. A network scission model for wormlike micellar solutions: I. model formulation and viscometric flow predictions. *Journal of Non-Newtonian Fluid Mechanics, 144: 122-139.*, 2007.

[111] H. K. Versteeg and W.Malalasekera. *An introduction to Computational Fluid Dynamics. The Finite Volume Method.* Longman Group Ltd., 1995.

[112] T. Waclawczyk and T.Koronowicz. Comparison of cicsam and hric high resolution schemes for interface capturing. *Journal of theoretical and applied mechanics, 46(2) :325-345.*, 2008.

[113] S. Q. Wang. Molecular transitions and dynamics at polymer/wall interfaces: Origins of flow instabilities and wall slip, in polymers in confined environments. *Adv. Poly. Sci. 138:227 - 275.*, 1999.

[114] P. Wapperom and M.A. Hulsen. Thermodynamics of viscoelastic fluids: the temperature equation. *J Rheol 42:999 - 1019.*, 1998.

[115] P. Wesseling. *Principles of Computational Fluid Dynamics.* Springler-Verlag Berlin Heidelberg New York., 2001.

[116] H. H. Winter. Can the gel point of a cross-linking polymer be detected by g' - g'' crossover? *Polymer Engineering and Science, 27(22):1698-1702*, 1987.

[117] T. Yamamoto, T. Hashimoto, and A. Yamashita. Flow analysis for wormlike micellar solutions in an axisymmetric capillary channel. *Rheol Acta, 47:963974.*, 2008.

[118] A. Yousefi and P. G. Lafleu. Kinetic studies of thermoset cure reactions: A review. *Polymer Composites, 18(2):157-168.*, 1997.

[119] X. F. Yuan. Dynamics of a mechanical interface in shear banded flow. *Europhys Lett 46:542 - 548.*, 1999.